Photocopy and Use Authorization

In presenting this thesis in partial fulfillment of the requirements for an advanced degree at Idaho State University, I agree that the Library shall make it freely available for inspection. I further state that permission for extensive copying of my thesis for scholarly purposes may be granted by the Dean of the Graduate School, Dean of my academic division, or by the University Librarian. It is understood that any copying or publication of this thesis for financial gain shall not be allowed without my written permission.

Signature: _____

Date: _____

Developing Low Noise, Rad-hard Detectors for Parity Violating Experiments

by

Carlos Bula Villarreal

A dissertation submitted in the partial fulfillment

of the requirement for the degree of

Doctor of Philosophy

in the Department of Physics

Idaho State University

Fall 2019

Committee Approval

To the Graduate Faculty:

The members of the committee appointed to examine the thesis of CARLOS BULA VILLARREAL find it satisfactory and recommend that it be accepted.

Dr. Dustin McNulty

Major Advisor

Dr. Tony Forest,

Committee Member

Dr. George Imel,

Committee Member

Dr. Steven Shropshire

Committee Member

Dr. Russell Wahl

Graduate Faculty Representative

Acknowledgments

Science requires the collaboration of people of different backgrounds. Each of us contribute with our different strengths to reach the common goal. Through collaboration, we all benefit in the search of our personal objectives. Without the contributions of my colleagues and the direction of my advisor, my work would have been impossible.

To them, thanks.

Table of Contents

List of Figures

List of Tables

Developing Low Noise, Rad-hard Detectors for Parity Violating Experiments.

Dissertation Abstract–Idaho State University (2019)

As parity-violating electron scattering (PVeS) experiments continue to push the frontiers of precision electro-weak asymmetry measurements, the demands on the experimental techniques and apparatus are also pushed. In particular, the need for higher resolution and radiation-hardness of the main integrating detectors has increased over the successive generations of PVeS experiments. The demand for precise measurement of GHz event rates has pushed the field toward the use of thin quartz Cerenkov light based detectors. We have been designing and testing such thin quartz detectors specifically for the upcoming experiments at Jefferson Lab, PREX-II and CREX, but this work also greatly influences the detector development for several future experiments including MOLLER at Jefferson Lab. These are all PVeS experiments that will use the new thin quartz Cerenkov detector design concept for their main asymmetry measurements (as well as for beam monitoring). The new design concept gives not only significant performance improvements compared to its predecessor from PREX-I, but also we have now thoroughly characterized its operational design and performance using a combination of test-beam data and detailed particle and optical Monte Carlo Geant4 simulations. These activities have culminated in the development and implementation of a "bench-marked" Monte Carlo package, QSIM, which constitutes a powerful design tool for present and future PVeS quartz detectors. The benchmarked simulation can replicate real photoelectron distributions (RMS and Mean) from testbeam data with $\sim$5% precision–limited mainly by the systematic uncertainty of the PMT gain measurements.

Key Words: Cerenkov Detector, thin quartz detector, QSIM.

1 Introduction

By comparing the cross section for left and right handed polarized electrons, scattered from various unpolarized nuclear targets, the small parity-violating asymmetry, A_{PV}, can be measured. These types of experiments are known as parity-violating electron scattering experiments (PVeS) and the quantity measured is:

$$A_{PV} = \frac{\sigma_R - \sigma_L}{\sigma_R + \sigma_L} \tag{1}$$

where $\sigma_R(\sigma_L)$ is the cross section for the scattering of longitudinally spin-polarized electrons, with right(left) helicity, from an unpolarized target. Because electromagnetism conserves parity, any nonzero value of A_{PV} must be due to weak interactions through the exchange of the neutral Z-boson (Z^0) according to the standard model.

PVeS has a definitive advantage for the study of nuclei: The quarks have different coupling strengths to the Z^0 and, as a result, the weak charge of the neutron is much larger than that of the proton. This makes PVeS much more sensitive to the distribution of neutrons inside nuclei, in contrast to purely electromagnetic (EM) scattering, which is essentially only sensitive to the EM charge or proton distribution.

PREX-II and CREX are 3rd generation PVeS experiments at Jefferson Lab. The present work focuses on the characterization of the thin quartz detectors being used in these experiments. We will cover topics including: The physical principles upon which the detector operation is based, optical properties of the active materials used and how they may be altered by radiation exposure, and the beam-testing and benchmarking of an optical Monte Carlo simulation of the detector. These endeavors have required the contribution of multiple researchers towards the same goal, the successful commissioning of the PREX-II/CREX detectors at JLab. These contributions range from technical engineering design, light reflectivity and transmission measurements,

PMT gain and linearity measurements and testing with electron beams. The optical simulation, QSIM, which is the main topic in this dissertation constitutes a powerful tool that can be applied beyond the PREX-II/CREX experiment: The simulation can be applied in the design of detector to be used in future experiments, such as MOLLER, which will measure the parity-violating asymmetry in electron-electron (Moller) scattering.

1.1 Historical Background of PVeS Experiments

1.1.1 Parity Symmetry

Symmetry principles are very important for physicists in their quest to understand forces in nature because they lead to conservation laws. Parity is the quantity conserved when there is mirror symmetry, and the laws of physics were all believed to conserve mirror symmetry with respect to left- and right-handed particle interactions [1]. In 1956 this belief was challenged by Lee and Yang [2]. They abandoned the principle of parity conservation in Weak force interactions in order to explain some puzzling observations on the decay of τ and θ mesons.

1.1.2 Wu Experiment

In 1958, Wu et. al.[3] determined experimentally that the charged Weak current associated with the nuclear decay of polarized [1] cobalt-60 violated parity symmetry [4]. The underlying process for this decay is represented in Figure 1 while the specific nuclear reaction is given by

$$^{60}_{27}Co \rightarrow ^{60}_{28} Ni + e^{-} + \overline{v}_e + 2\gamma \tag{2}$$

[1]The experiment study the decay of cobalt-60, cooled to near absolute zero and aligned in a uniform magnetic field. At that time, the experiment presented great technical challenges.

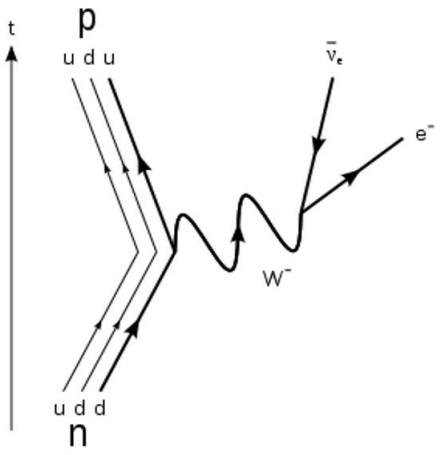

Figure 1: Feynman diagram for the fundamental Beta decay, Weak force interaction in which a *down* quark flavor changes to an *up* quark by emitting a negatively charged W-boson which quickly decays into an electron and anti-electron neutrino pair ($n \rightarrow p + \bar{\nu_e} + e^-$).

Where the $^{60}_{28}$Ni isotope is created in an excited state and decays electromagnetically by emitting two photons. Wu's experiment monitored the angular distributions of electrons and photons emitted during the decay and cleverly performed the experiment two different ways using a mirror-symmetric apparatus. The result was spectacular: while the electromagnetic photon decay part of the reaction conserved parity and provided the control variable, the Weak beta decay component violated parity nearly maximally. That is, in the mirrored apparatus, the electrons are emitted in the opposite direction than one would have expected given conservation of parity. Apparently, the distribution of electrons is preferentially opposite to the nuclear spin, and this introduces a violation of parity conservation since spin changes handedness when viewed through a mirror.

1.1.3 SLAC E122 Experiment

In 1978, the first observation of parity violation in inelastic electron-deuterium scattering was reported by Prescott et. al.[5]. Their experiment, E122, measured an

asymmetry of the order 10^{-4} or 100 ppm. Because the asymmetry was so small, the experiment required a number of innovations, nearly all of which are still important for PVeS today. A blueprint of the experiment design is given in Figure 2.

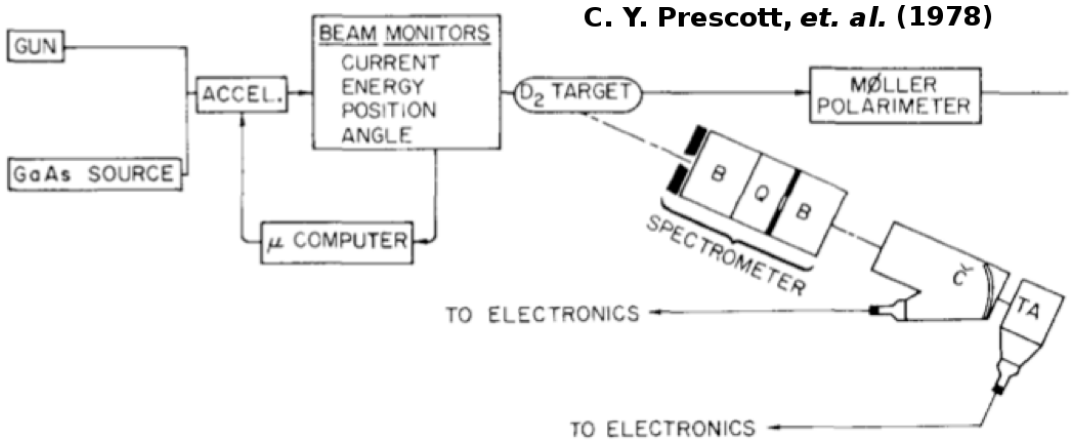

Figure 2: Sketch of experimental apparatus design for the pioneering SLAC E122, so-called Prescott experiment.

The most important innovation was the polarized electron beam source. The polarization of the electron beam was pseudo-randomly flipped, pulse by pulse, several times per second. This was accomplished by changing the voltage across a Pockels cell, a birefringent optical crystal that can change linearly polarized light to left or right circularly polarized. This highly polarized light is then incident on a specially designed photocathode capable of injecting highly polarized photoelectrons into the beamline with high current. The rapid helicity reversals minimized the effects of slow drifts during the experiment, such as drifts in beam parameters or detector efficiencies, and the pseudo-random nature of the flipping helped avoid false asymmetries from pick-up or cross-talk in the data acquisition electronics from adjacent beam pulses.

Another important innovation was the development of a new, nearly dead-timeless type of data acquisition system (DAQ). This was necessary to achieve the desired statistical precision in the measurement of the very small PV asymmetry. This aspect of PVeS experiments is discussed further in Section 4.2.3. Since the E122 experiment detected scattered electrons at very forward angles (4 deg) from a relatively thick 30

cm long liquid deuterium target and with high beam current, the detected rates were very high – of the order 10^5 Hz. To handle these large rates a new "integrating" DAQ was developed which sums or integrates the detector response of all electrons detected during a particular helicity pulse. This is in contrast to the more conventional event-based "counting" DAQ – which can have large dead-time corrections with potential for associated large systematic errors.

Scattered electrons which entered the spectrometer aperture and fell within a momentum acceptance were detected in two independent counters, a gas Cerenkov counter and a lead-glass calorimeter. Up to 1000 electrons per linac pulse (or helicity window) were detected in the spectrometer and there were over a hundred of these pulses per second. In order to capture and record all of the high counting rate, signals were integrated over the pulse and digitized for both the Cerenkov and the lead-glass counters. The data-acquisition computer stored the charge normalized, integrated signals for each pulse, sorted by the beam polarization.

Systematic errors were studied at considerable length. The most serious systematic error arose from beam parameters which changed with helicity reversals. Such effects could induce false asymmetries indistinguishable from the real ones. The experiment was set up to monitor six beam parameters, x and y at the target, θ_x and θ_y at the target, Q (charge per pulse) and the E_{beam}. Each parameter was read and logged for each pulse.

False asymmetries, or differences generated by the helicity reversals were an important part of the monitoring and analysis. The most important contribution to the systematic errors arose from ΔE_{beam} due to the helicity reversals. This effect arose due to the minor changes to Q generated at the source by the Pockel's cell modulation. The beam loading [2] in the linac connect changes in Q to changes in E_{beam} [6].

[2]The electromagnetic interaction of the bunched electron beam in a linear accelerator with the waveguide cavities of the linac can change the electron's energy.

Since the deep inelastic scattering cross section is strongly dependent on the energy of the beam, the effect of ΔE_{beam} was the most serious.

The experimenters also checked whether the apparatus produced spurious asymmetries. They measured the same scattering using an unpolarized beam, for which the asymmetry should be zero. They assigned polarization to the beam using the same random-number generator that determined the sign of the voltage on the Pockels cell. They obtained a value for $A_{exp}/P_e \sim (-2.5 \pm 2.2) \times 10^{-5}$, where A_{exp} is the experimental asymmetry and P_e is the beam polarization. This value demonstrates that the apparatus could measure asymmetries of the order of 10^{-5}[7]. A summary of all these innovations and how they relate to the blueprint of Figure 2 is shown in Figure 3.

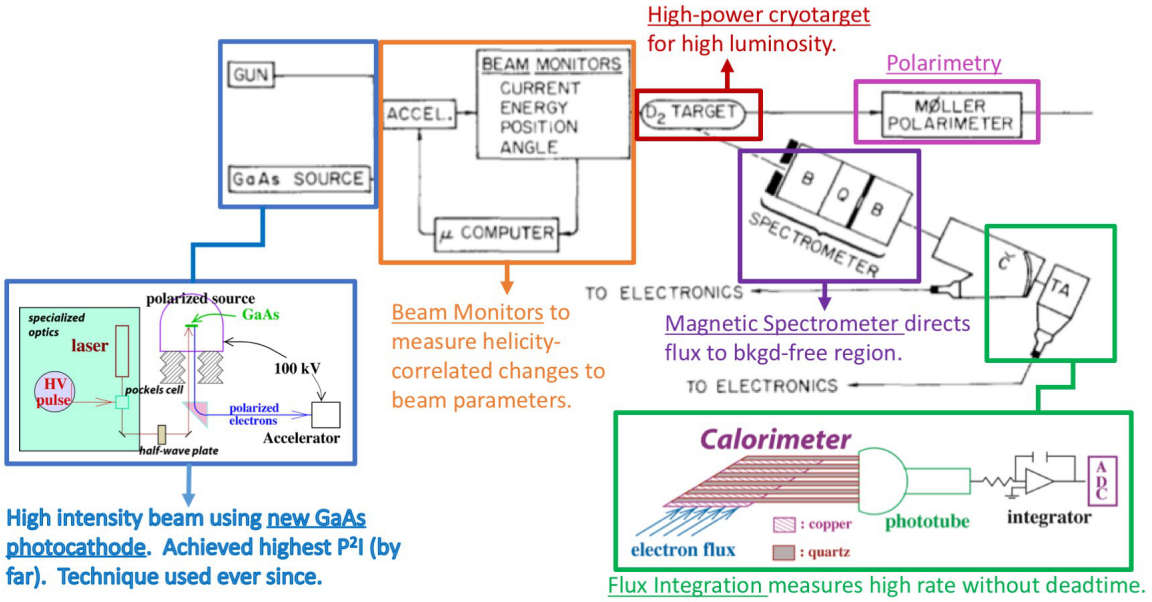

Figure 3: Highlighted innovations developed for E122.

In June 1978, E122 announced the evidence for parity violation in the inelastic electron-deuterium scattering. The statistical significance exceeded 10 sigma. Consistency checks and null tests were fully satisfied. In the Fall, E122 ran again and the combined data agreed with the Weinberg-Salam Model and gave a value for the

Weinberg mixing angle of $sin^2\theta_W = 0.224 \pm 0.020$. This was a clear indication of a neutral *weak* current interaction and essentially represented a new, powerful tool for probing nuclear structure as well as fundamental symmetries in nature with electron scattering[7].

1.2 Evolution of PVeS Experiments

As the field of PVeS has developed over the decades that followed the pioneering work of Prescott et. al., the size of the PV asymmetry (A_{PV}) has logarithmically decreased while the precision of its measurement, $\delta(A_{PV})$, has steadily improved. (See Figure 4, and corresponding Table 1) for a graphical representation of the experiments that make-up this evolution of the field.

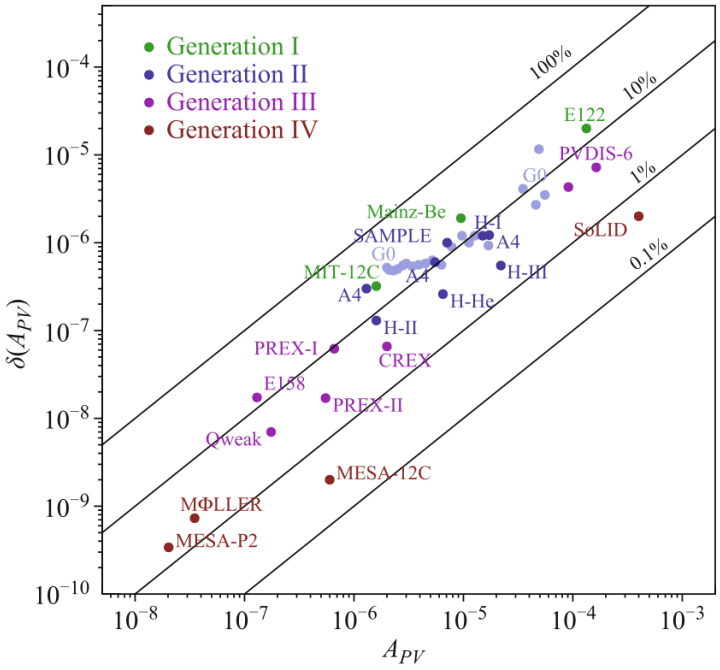

Figure 4: PVeS progress over the successive generations of experiments in terms of the asymmetries measured and their fractional errors. The diagonal lines indicate decades of relative error in the asymmetry. Measurements get more and more challenging as one moves down and to the left in the figure.[8]

Experiment	Year	Detector	A_{PV}	$\delta A(stat.)$	$\delta A(syst.)$	$\delta A/A(\%)$
SLAC-E122	1978	Pb glass	120	7	6	8
Mainz-Be	1989	Air C	9.4	1.8	0.5	20
MIT-12C	1990	Lucite C	1.62	0.37	0.11	24
SAMPLE	1990	Air C	5.61	0.67	0.88	20
HAPPEX-I	2001	Pb Lucite	15.05	0.98	0.56	7.5
GO	2005	Scintillator	2	0.15	0.2	13
SLAC-E158	2005	Cu-quartz	0.131	0.014	0.010	13
HAPPEX-He	2007	Cu-Quartz	6.4	0.23	0.12	4.1
Mainz-A4	2009	PbF_2	17.2	0.8	0.9	5
HAPPEX-III	2011	Pb-Lucite	23.8	0.78	0.36	4.6
PREX	2012	Quartz	0.656	0.060	0.014	9.4
Qweak	2013	Pb-Quartz	0.280	0.035	0.031	17
PREX-II	2019	Quartz	0.51	0.015	0.005	3
CREX	2019	Quartz	2	0.04	0.02	2.4
MOLLER	2024	Quartz	0.035	0.0007	0.0004	2.3
SoLID	2025	Package	800	2	4	0.6
Mainz-P2	202?	Quartz	0.020	0.00025	0.00019	1.7
Mainz-C	202?	Quartz	0.8	0.0025	0.00017	0.3

Table 1: Chronological list of PVeS experiments: past, present and future. Also given are the experiment results (or proposed results) with statistical asymmetries and errors are given in units of parts per million (ppm). [8, 9]

The statistical error in a PVeS experiment is given by:

$$\delta A_{PV} = \frac{1}{P_e\sqrt{N}} \tag{3}$$

Where N is the number of events detected and P_e is the beam polarization. The number of events, N, can be written as

$$N = IznT\frac{d\sigma}{d\Omega}\Delta\Omega \tag{4}$$

where I is the beam current, z target thickness, n is the target number density, $d\sigma/d\Omega$ is the differential cross section, $\Delta\Omega$ is the detector angular acceptance and T is the running time[8]. In a given experiment, it is very desirable to make the beam current, target thickness and detector acceptance as large as possible, in order to acquire enough number of events in a reasonable time to reduce the statistical error.

The typical beam current, I, for a parity experiment is around $\sim$50 μA, and sometimes over 100 μA in some experiments. At these high currents, radiation hard detectors and precautions against target melting or boiling are required. For solid targets, the target thickness, z, is usually on the order of few millimeters. The target thickness z is limited by the fact that electrons radiate when passing through material; the beam loses energy to radiation and the rate of useful (elastic) events no longer increases with z.

Then, the detector has to deal with high currents and its thickness is limited by the fact that the electrons will radiate when passing through material, losing part of their energy and creating secondary events. This circumstance impacts the statistics and the detector resolution.

1.3 Low-noise Thin Quartz Detectors

The purpose of the main detectors is to count the scattered electron flux with the highest resolution possible (low-noise). Since this flux is typically very large, these detectors must be made of radiation-hard materials. The detectors for PVeS experiments must have a response dominated by the scattered electrons and produce a signal proportional to the electron flux. The first experiments used total absorption calorimeters sensitive mostly to Cerenkov radiation, but these calorimeters had poor resolution for single electron signals.

A thin quartz Cerenkov detector consists of three essential components: a dielectric crystal (fused-silica quartz), a lightguide that collects/directs the photons to a photosensitive device, and the photo-sensitive device such as a photo-multiplier tube (PMT). Note that "thin" quartz is meant to classify a single dielectric crystal with a thickness in the range of $\sim$ 0.5 cm to $\sim$ 2 cm.

When a highly relativistic charged particle travels through the quartz, it produces

a number of Cerenkov photons, usually counted by the thousands. This is a statistical process in nature – in the sense that two separate events would not produce the same number or distribution of photons. The number of photons generated per incident electron follows a Poisson distribution, with the mean dominated by the thickness of quartz material traversed by the electron. The photons are emitted from electromagnetic disturbances inside the quartz (dielectric, i.e. electrically polarizable) when a charged particle traverses it at a greater speed than the speed of light inside the quartz. Therefore, the number of photos produced has an inherent fluctuation related to the electromagnetic disturbances inside the dielectric. Additionally, there are fluctuations in the number of photons from delta-rays. These are extra electrons resulting from secondary (hard) scattering processes inside the quartz which create extra (unwanted) light, collectively referred to as a Landau tail – this is further discussed in subsection 1.5.3.

After their creation, the photons can be internally reflected inside the quartz towards the PMT – an important point that is further discussed in subsection 1.5.4 – but due to small imperfections in the quartz surface polish, some of these photons escape; they could also be absorbed by the lightguide surface. All these processes are statistical in nature, and the number of photons that reach the PMT photocathode are typically counted by the hundreds. Finally, those remaining photons that impinge on the PMT are converted to photoelectrons (PEs) according to the photocathode's quantum efficiency (QE), and these PEs are typically counted by the tens.

The PEs produced, for each detected scattered electron, then pass through the amplification stages or dynodes of the PMT; these processes are also statistical in nature. All the fluctuations that occur during the "counting" of a single electron contribute to the detectors finite resolution which impacts the statistical error in the measured asymmetry. But the biggest contributor to that resolution is the average number of PEs produced per electron, $\langle n_{\mathrm{PE}} \rangle$. This is because it is the smallest

number in the chain of processes and thus dominates the quadratic sum of the relative statistical fluctuations ($1/\sqrt{\langle n_{\rm PE}\rangle}$).

To give an example of the importance of the main detector's resolution, if an asymmetry of 0.5 ppm is measured with 3% statistical precision, it means that the statistical error is 0.015 ppm, but this would be only for a perfect resolution detector. The reality of finite resolution reduces the overall statistical precision of the measurement. We refer to this effective increase in statistical error as excess noise which is defined as

$$\text{excess noise} = \delta_e - 1, \text{ where} \tag{5}$$

$$\delta_e = \sqrt{1 + (\text{resolution})^2}, \text{ where} \tag{6}$$

$$\text{resolution} \equiv \frac{rms}{mean} \tag{7}$$

The rms/mean represents the resolution of the main detectors and is extracted from the event-mode pulse-height distributions of the main detectors, that is, the collective distribution or histogram of the number of PE's produced by each passing electron. So now, in the above example, if the detector has an overall resolution of 30%, the excess noise is $\sim 4.4\%$ and so the *actual* statistical error is inflated to ~ 0.0157 ppm, and the experiment would need to collect an additional $\sim 10\%$ more data to "actually" achieve the 3% statistical precision. Which means, nominally, that the time duration of the experiment would need to be increased by 10%, and this is undesirable.

1.4 PREX-I Experiment at JLab

The PVeS technique has been used over the decades as a probe to help answer various questions about topics ranging from fundamental physics parameters to nuclear structure. The application of the technique always exploits the parity-violation signature of the interaction to access the desired physics. For the case of the Pb Radius

Experiment (PREX), the technique is exploited to measure the neutron radial distribution of a ^{208}Pb nucleus. The proposal for the experiment was accepted in year 2000 [10], the experiment ran in 2010, and published in 2012[11] (the idea for the experiment is remarkably simple and is credited to Swiss physicist Ingo Sick). The idea is this: neutrons have $\sim 14\times$ more weaker charge than protons and so PVeS will primarily probe the neutron distribution, in contrast to conventional EM scattering which probes the charge (or proton) distribution. Combining the neutron radius (R_n) measurement of PREX with precise knowledge of the proton radius (R_p) of ^{208}Pb from past experiments, a quantity referred to as the *neutron skin* ($n_{\text{skin}} = R_n - R_p$) can be determined.

In the Born approximation, the parity-violating asymmetry, A_{PV}, is proportional to the nuclear weak form factor $F_W(Q^2)$

$$A_{PV} = \frac{G_F(Q^2)}{4\pi\alpha\sqrt{2}} \frac{F_W(Q^2)}{F_{ch}(Q^2)} \tag{8}$$

where $F_{ch}(Q^2)$ is the Fourier transform of the known charge density, and in the same way, $F_W(Q^2)$ is related to the neutron density. So a measurement of A_{PV} is a measurement of the neutron distribution and thus R_n.

1.4.1 Motivations

A ^{208}Pb nucleus is made up of 82 protons and 126 neutrons. This means it has 44 more neutrons than protons; some of the extra neutrons are expected to be found in the surface, where they form a neutron rich skin. The value of the neutron radius of ^{208}Pb has important implications for a wide range of physics fields, from radioactive isotope beams to astrophysics. There is a strong correlation between R_n of ^{208}Pb and the density dependence (or slope) of the symmetry energy. The symmetry energy is the

energy "cost" per nucleon for having a nucleus with asymmetric numbers of protons and neutrons; that is, the overall nuclear binding energy per nucleon is reduced by this "repulsive" effect. For example, a larger n_{skin} measurement would indicate a steeper slope of the symmetry energy which is interpreted as a higher "pressure" for asymmetric matter—pushing the extra neutrons out to the surface. There is a strong connection between this measurement, done at ordinary nuclear saturation densities ($\rho_0 \approx 0.16$ fm^{-3}), and the slope of the symmetry energy for neutron star matter and densities. So the PREX A_{PV} measurement can tell us something about the size of neutron stars. It's important to note that prior to PREX-I, the slope of the symmetry energy was completely unconstrained by real data.

1.4.2 Experimental Apparatus

The PREX-I measurement was carried out in Hall A at the Thomas Jefferson National Accelerator Facility (Jefferson Lab or JLab) in Newport News, Virginia, USA (see Figure 5). PREX-I used a 1 GeV longitudinally polarized electron beam with a current of 50 to 70 μA scattered by a 0.55 mm thick (10% of the radiation length for lead, X_o) isotopically pure ^{208}Pb target foil. A 4×4 mm^2 beam raster was employed to prevent the target from melting. Two 150 μm diamond foils sandwiched the lead foil to improve thermal conductivity to a copper frame cooled to 20 K with cold helium gas.

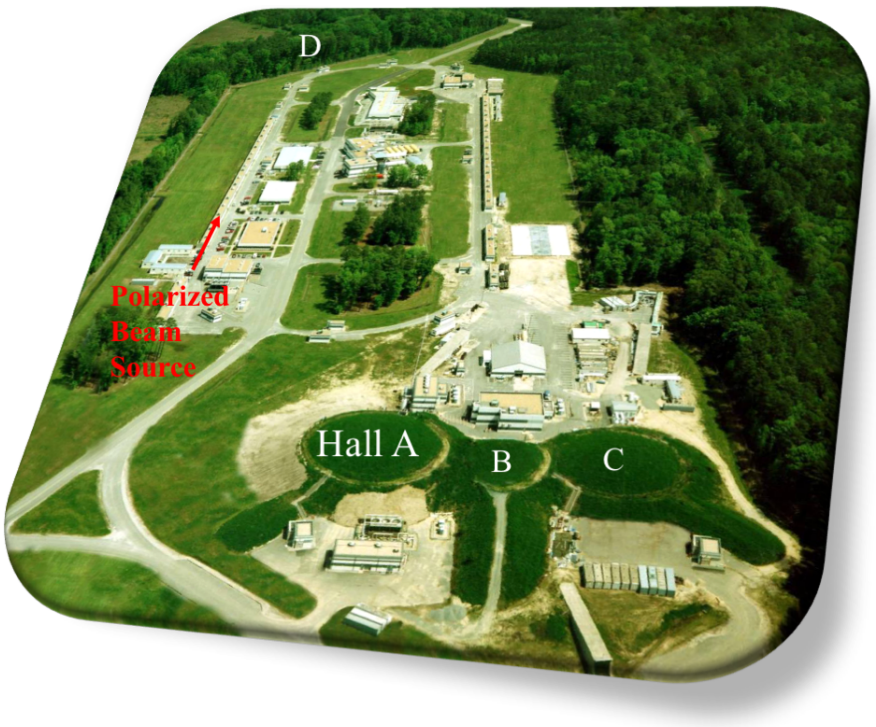

Figure 5: Aerial view of Jefferson Lab showing the accelerator and experimental halls A, B, C, and D. Polarized electrons are injected into the racetrack-shaped continuous electron beam accelerator facility (CEBAF), where they can acquire up to 11 GeV before being sent to Hall A.

Elastically scattered electrons emerging from the target were focused onto the main integrating flux detectors using Hall A's twin High Resolution Spectrometers (HRSs). A photo and schematic of the spectrometers are shown in Figure 6. The two HRSs are positioned symmetrically on either side of the beamline downstream of the target. They have a very small angular acceptance, on the order of 10^{-3} sr and were placed in their most forward position ($\pm 12.5^{\circ}$ with respect to the beamline). A septum magnet was used between the target and the HRS to pass electrons scattered from the target, at $\theta_{lab} = \pm 5^{\circ}$, to the HRSs.

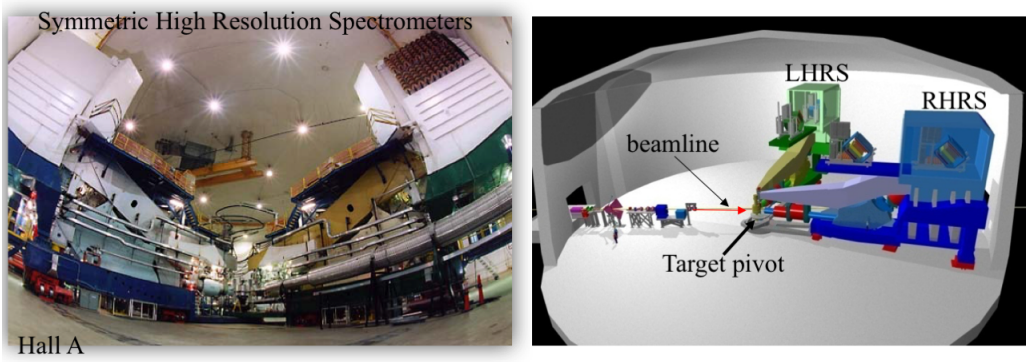

Figure 6: Photo (left) and schematic (right) of Hall A HRS. For parity violation experiments, the HRSs are positioned symmetrically about the beamline. Having two detectors double statistics and the symmetry allows for checks and reduction of systematic errors.

1.4.3 Main Detectors

The main integrating detectors for PREX-I were thin quartz arrays made of two optically polished, fused-silica (quartz) tiles, one 6 mm thick and the other 10 mm thick and each with a 45 deg "bevel" cut on one end. The fused silica bars or tiles were made out a trade-marked material called Spectrosil-2000 with optical polish on all six sides; they were 16 cm long by 3.5 cm wide. The thicker tile was placed downstream of the thinner tile, and both were oriented horizontally, making an angle of 45 deg with respect to the incoming scattered electrons (see Figure 7). Cerenkov light from the quartz bars was detected by 2" Hamamatsu photomultiplier tubes (PMT).

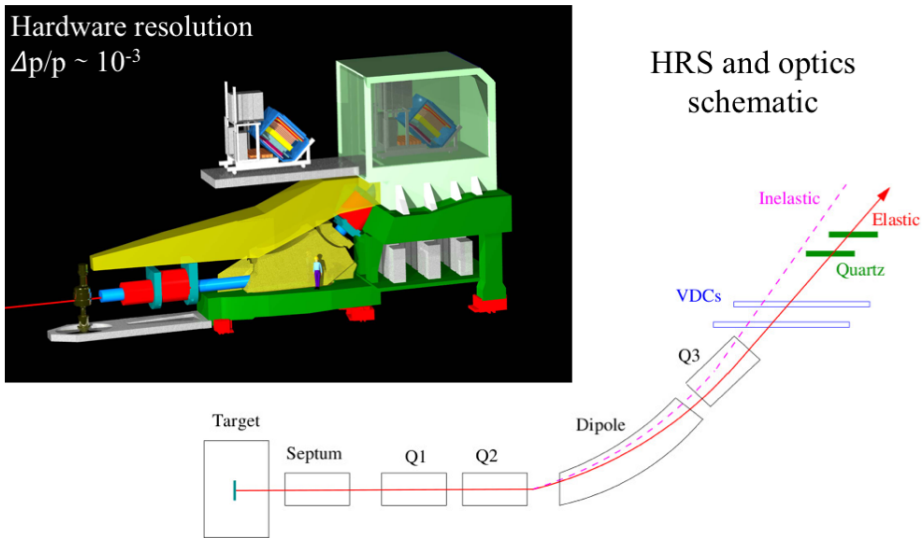

Figure 7: Schematic of focal plane quartz detector concept for PREX-I. Top figure shows the HRS detector hut with removable detector packages. Bottom schematic shows the optics of the spectrometer and orientation of quartz tiles in the HRS focal plane. Note that the length and position of the quartz tiles (within the focal plane) were engineered to only intercept the elastic-scattered part of the signal.

As an electron traverses the quartz with velocity $v \approx c$ (the velocity of light in vacuum), Cerenkov photons are continuously emitted at an angle $\theta_C = 46.58^{\circ}$ relative to the electron's direction of motion. From the index of refraction of the quartz tiles, Snell's Law states the total internal reflection (critical) angle is $\theta_c = 43.619^{\circ}$. This means there is a range of near-normal incident angles (and wavelengths) in which the photons created in the quartz will be trapped via total internal reflection (TIR). This range is $\pm 3.16^{\circ}$ $(\theta_C - \theta_c)$ from perfect normal incidence. A plot showing the range of wavelengths for achieving TIR is given in Figure 8.

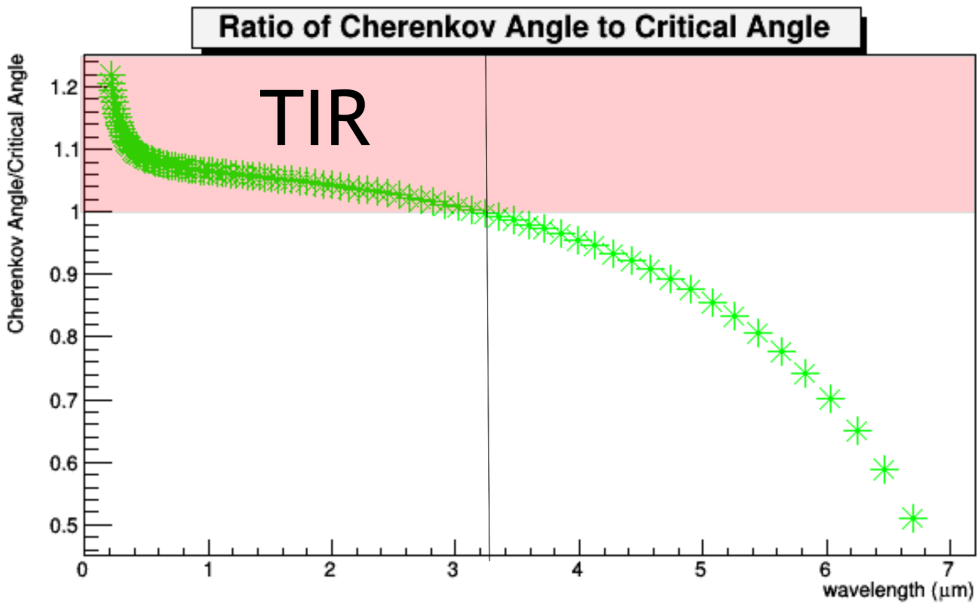

Figure 8: Ratio between Cerenkov angle and Total reflection critical angle. The plot of the ratio shows the Cerenkov angle is larger than the critical angle in the UV and visible ranges. (Plot from Joey McCullough)

For PREX-I, the incident angle was $\sim 45^{o}$ (refer to Figure 7). This means that half of the Cerenkov light cone went directly to the PMT while the other half escaped from the tile and was mostly lost. Configuring the quartz this way caused much lower light levels and worse resolution (due to relatively large Landau tails), but it had one advantage that the performance of the detector did not strongly depend on its precise orientation in the focal plane. The light yields and more importantly resolutions, while not optimized in this configuration, were the most stable given uncertainties in orientation of the quartz tile on the order of a few degrees. For PREX-II, with precision angle alignment between beam and quartz as well as the TIR feature, we have managed to increase light yields and enhance resolution by a factor of 2.

1.4.4 PREX-I Result and PREX-II/CREX Proposal

PREX-I measured an asymmetry:

$$A_{PV}^{^{208}Pb} = 656 \pm 60(\text{stat}) \pm 14(\text{syst}) \text{ ppm} \tag{9}$$

which corresponds to a difference between the radii of the neutron and proton of:

$$R_n - R_p = 0.33^{+0.16}_{-0.18} \text{ fm} \tag{10}$$

at $Q^2 = 0.008 \pm 0.00011$ GeV^2. This represents the first electroweak observation of a (non-zero) neutron skin at the 95% confidence level[11]. Note that PREX-I only collected 30% of its proposed statistics due to radiation-induced downtime. The combination of relatively low energy beam and a thick (10% $X_\circ$) target led to excessive EM and neutron radiation levels around the target and spectrometers (magnet power supplies and controls). The target chamber vacuum failed twice during the experiment due to excessive heat on a downstream o-ring, and each time this happened it took weeks to fix. There were also spurious spectrometer magnet trips which became untenable by the end of the experiment – causing much inefficiency in data collection. However, even though the experiment did not achieve its statistical error goals, it did achieve its systematic error goals (less than 2% total systematic error), showing that the proposed measurement precision could be achieved in a future extension to the experiment.

After addressing the radiation problems encountered during PREX-I, the collaboration submitted a proposal to run PREX-II – in order to achieve the PREX-I statistical error goal. This proposal was approved by the advisory committee at JLab and granted its full beam-time request. Along with this proposal, another experiment was put forward by the collaboration to perform a neutron radius measurement on

^{48}Ca. This experiment is named CREX and will run successively (back to back) with PREX-II. It uses all the same exact equipment as PREX-II in the same configuration; the only differences are the target material and the beam energy and current. The main integrating detectors in the HRS focal planes are the same for PREX-II and CREX.

1.5 New PREX-II/CREX Detector Design

The next generation of PREX, PREX-II, will have a new redesigned thin quartz detector in order to achieve higher light levels and better resolution and therefore reduce error inflation as compared with the previous experiment.

1.5.1 Evolution from PREX-I to PREX-II/CREX with QSIM

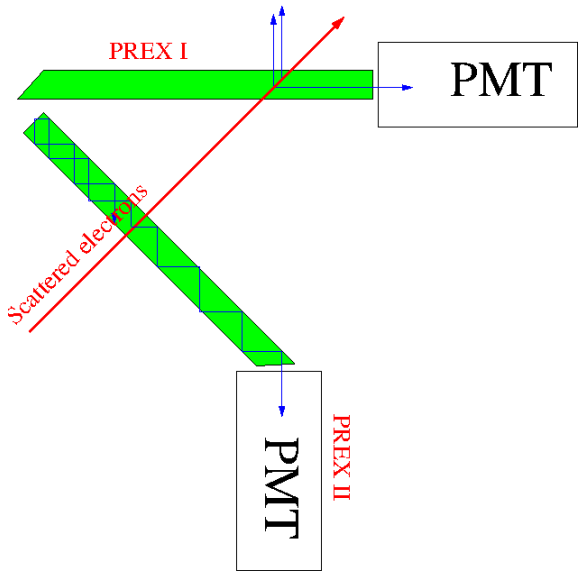

Figure 9: PREX-I (top detector) and PREX-II (bottom detector) design concepts. Note that the new PREX-II/CREX design takes advantage of the total internal reflection (TIR) of the Cerenkov light inside the quartz (shown as blue lines).

The PREX-I and PREX-II/CREX designs concepts are displayed on Figure 9. Their key features are:

- PREX-I
  - e^- has $\sim 45°$ angle of incidence.
  - PMT captures half of Cerenkov light cone. Most of the other half is refracted out of the quartz, and a reflective funnel was used with the intention of reflecting some of those lost photons towards the PMT.
  - It's light yields and resolution are relatively insensitive to incident angle.
  - The signal is independent of the beam energy.
- PREX-II/CREX:
  - e^- has $\sim 90°$ angle of incidence.
  - It uses total internal reflection (TIR) inside the quartz to capture all the photons.
  - For a given quartz thickness, it has a smaller Landau tail compared to PREX-I design (less material traversed)
  - The signal is independent of the beam energy.
  - Light yield and resolution are more sensitive to incident angle.

Overall, PREX-II design performs better than PREX-I design: PREX-II gives two times more light output and 40% better resolution. In the following sections I will remark on the importance of the new design; a basic sequence of the detector operation is given below.

The general idea behind the new PREX-II/CREX detector can be summarized in Figure 10: (1) electrons are scattered towards the quartz with a speed near the speed

of light; (2) the electron traverses the quartz with near-normal incidence and the "shock wave" generates a number of Cerenkov photons, N_γ; (3) the light is internally reflected in the quartz and will bounce repetitively (with some possible loses) until; (4) the reflections are interrupted by the bevel cut on one end of the quartz and the photons escape; (5) the photons flowing out of the quartz will fly towards the PMT window, where they will release a number of photoelectrons (PEs), N_e, governed by the photocathode quantum efficiency. Those PEs will each be amplified by the different PMT dynode stages to create a measurable charge pulse over a small, tens of nanosecond, time scale.

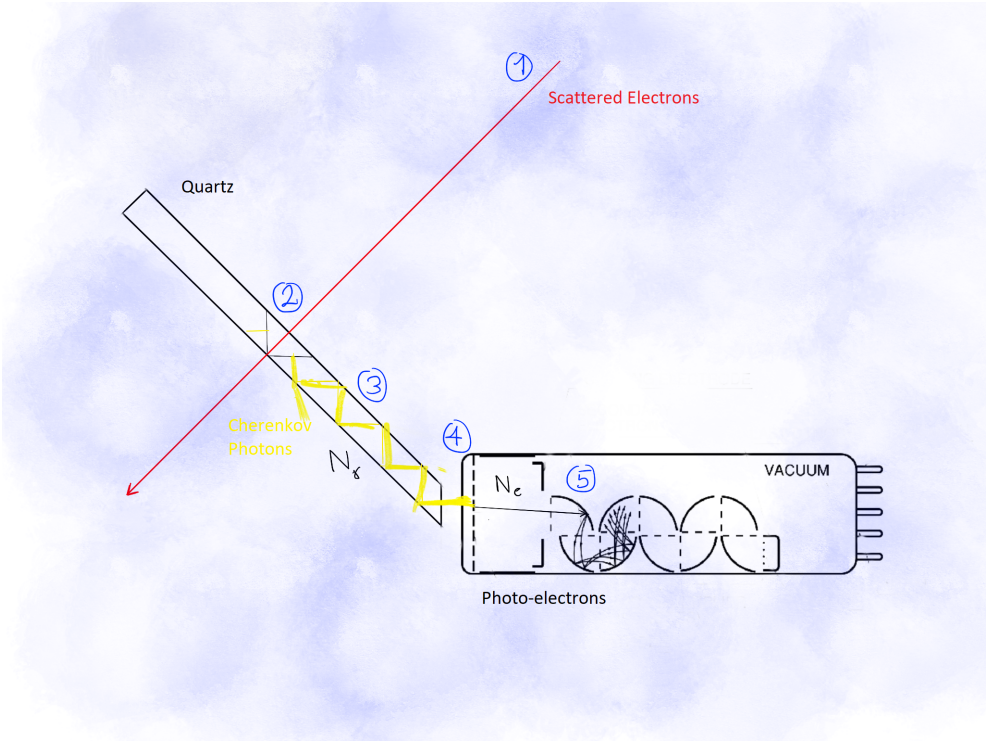

Figure 10: General picture with the fundamentals of the PREX-II/CREX design. (1) Scattered relativistic electron. (2) Cerenkov photons creation. (3) Total internal reflection. (4) Photoelectron creation. (5) Photoelectron multiplication.

The understanding of each previously numbered steps, requires the study of physical processes and PMT's properties, like the Cerenkov effect and the optical properties of quartz and photocathode, the PMT's quantum efficiency and gain. But before go-

ing into these details, let us state the importance of this new detector for the PREX-II experiment.

1.5.2 The Importance of the Detector Design

The PREX-II/CREX detector will be used to measure the flux of polarized electrons scattered by a lead and calcium targets by integrating the signal from the PMTs. The electrons impacting the target will be arranged in pulses according with their two possible polarization states. The detector signal will be integrated over the duration of the pulse. The integration has the advantage that there is no pileup or dead time, but it is not possible to identify and reject any background events. Fortunately with the HRSs in Hall A at JLab, elastically scattered events are physically separated from almost all inelastic events, and very clean samples are obtained with very small background, even though the signal is integrated.

For a 1 GHz incident scattered electron flux, it is impossible to distinguish the signal for individual electrons. Therefore the experiment requires a detector with resolution at the 25% level or better, and capable of measuring small differences in the electron flux. For an event-based, "counting" experiment the statistical error of A_{PV} is simply $1/\sqrt{N}$, where N is the number of asymmetry measurements (or helicity window pairs). For an "integrating" experiment with an average detector response signal $mean$ and width rms (finite resolution), the statistical error is inflated:

$$\delta A_{PV} = \sqrt{\frac{1 + rms^2/mean^2}{N}} \tag{11}$$

If the detector has a resolution of, for example, $rms/mean \sim 20\%$, the statistical error increases by 2% relative to an event-based counting experiment. Thus, if the detector has a reasonable resolution and the backgrounds are under control, few

statistics are lost by using the integrating data acquisition (DAQ) technique [9].

The resolution of the detector depends a great deal on its design. A design that leads to a long Landau tail will have a large $rms/mean$, (worse resolution) and may result in an unacceptable loss of statistics when the signal is integrated – due to the excess noise. A typical charge distribution from the PREX-II/CREX quartz detector can be seen in the Figure 11.

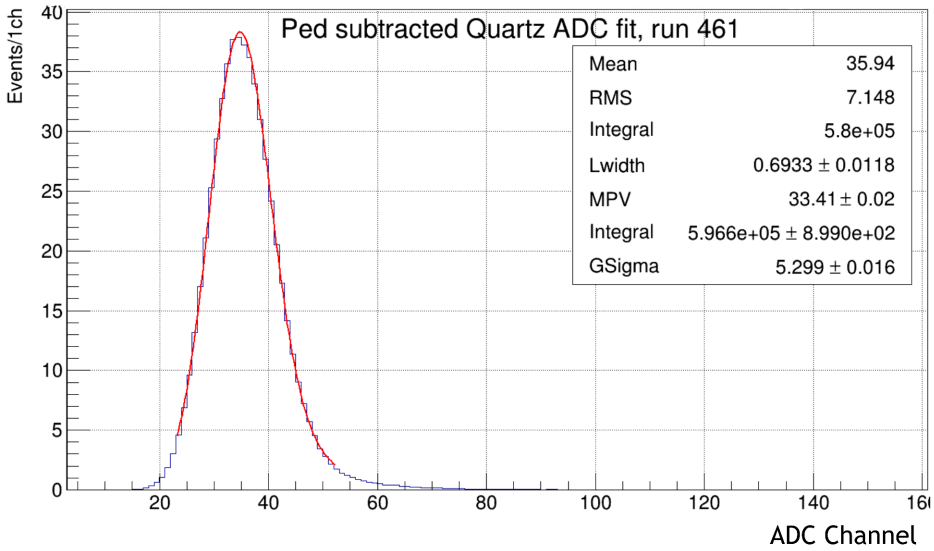

Figure 11: Typical data sample of PREX-II/CREX quartz detector. The fit used is a convolution of a Gaussian, describing the resolution for single electron events, and a Landau function, fitting the additional signal from secondary particles.

As indicated by Equation 11, minimizing the relative width (or resolution) of the detector response allows the statistical precision of the asymmetry measurement to asymptotically approach that of an event-based measurement (i.e. $1/\sqrt{N}$). This reinforces the importance of minimizing the high energy or high-light Landau tail associated with secondary particles (delta-rays), as these will increase the rms, worsening the resolution of the detector.

Additionally, for high rate experiments like PREX, the radiation damage becomes important and a high-purity fused silica (quartz) crystal is the material of choice be-

cause it can withstand extremely high radiation doses while maintaining light transparency in the UV through visible regime. This is the region of overlap between the produced Cerenkov radiation and PMT photocathode peak quantum efficiency.

The detector performance fundamentally depends on two physical processes: The Cerenkov mechanism and the total internal reflection (TIR) inside the quartz (which is dependent on critical angle as well as surface polish). The detector resolution is primarily determined by how efficiently it can deliver the produced light to the PMT, and this efficiency is determined by the constraints imposed by these two physical processes. That is, the interplay between the incident electron angle, the Cerenkov angle, and the critical angle for the fused silica bar.

1.5.3 Cerenkov Mechanism and Delta Ray Production

Cerenkov radiation is emitted by charged particles traversing matter if their velocity exceeds the phase velocity of light in the material, c/n, where n is the real part of the material's refractive index. This leads to the Cerenkov criterion:

$$\beta = \frac{v}{c} > \frac{1}{n} \tag{12}$$

The charged particle generates a light-cone shock-wave as it travels through the material. The increasingly acute angle of the cone with respect to the charged particle momentum, along which the photons are emitted is:

$$cos(\theta) = \frac{1}{\beta n} \tag{13}$$

Distributions of the Cerenkov angle and photon wavelength spectrum from the Monte Carlo, QSIM, can be seen in Figure 12.

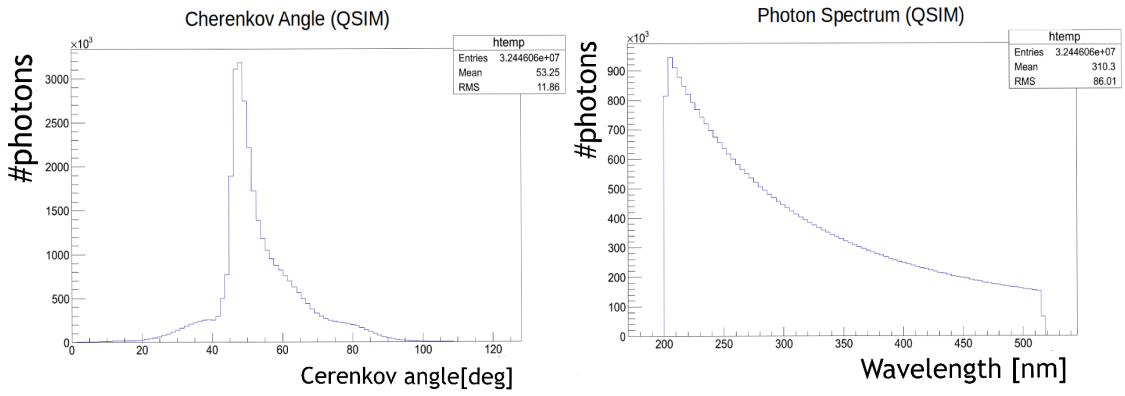

Figure 12: QSIM (Quartz SIMulation) distributions of the Cerenkov angle and photon spectrum. Cerenkov photons, for charged particles with velocity $v \approx c$, are emitted at an angle $\theta_C = 46.58$ deg (equation 13) relative to the charged particle direction of motion (left). The cuts in the photon spectrum (right) are given by the PMT quantum efficiency. The simulation corresponds to PREX-I detector being hit by cosmic muons. QSIM will be introduced in Chapter 3.

The mean number of Cerenkov photons that are produced by a particle with charge z per path length x and photon wavelength λ is:

$$\frac{d^2N}{dxd\lambda} = \frac{2\pi\lambda z^2}{\lambda^2}\left(1 - \frac{1}{\beta^2 n^2(\lambda)}\right) \approx \frac{2\pi z^2}{\lambda^2} sin^2(\theta_C) \tag{14}$$

As mentioned before, the photons are emitted on the surface of a cone, and as the mother particle slows down, the cone angle decreases, the emitted photon frequency increases and their number decreases.

The number of Cerenkov photons is directly proportional to the quartz thickness. As the thickness is increased, the average light produced per electron increases but the Landau tail of the photoelectron distribution increases (relative to the peak) and the resolution starts to quickly degrade. If the detector's quartz piece is too thin, then the peak light flash is too dim and the resolution, which effectively goes as $1/\sqrt{\langle \mathrm{PE} \rangle}$, suffers. The optimal thickness is found by a balance between having as large a $\langle \mathrm{PE} \rangle$ as possible while keeping the delta-ray production relatively low.

A delta-ray is a secondary electron produced inside the quartz by a hard scattering process. This secondary electron is relativistic and so creates additional Cerenkov radiation that can be seen by the PMT. This extra light shows up as a "high-energy" or Landau tail in the pulse height distributions of the detector response. Without these secondaries, the detector response would be purely Gaussian. Figure 13 shows a simulation of the PREX-II/CREX main detector pulse-height distribution. This figure shows the Gaussian signal from the detected "mother" electron along with the Landau tail component from delta-rays. The Landau tail component is isolated using the simulation and plotted in red (artificially by itself) in the figure.

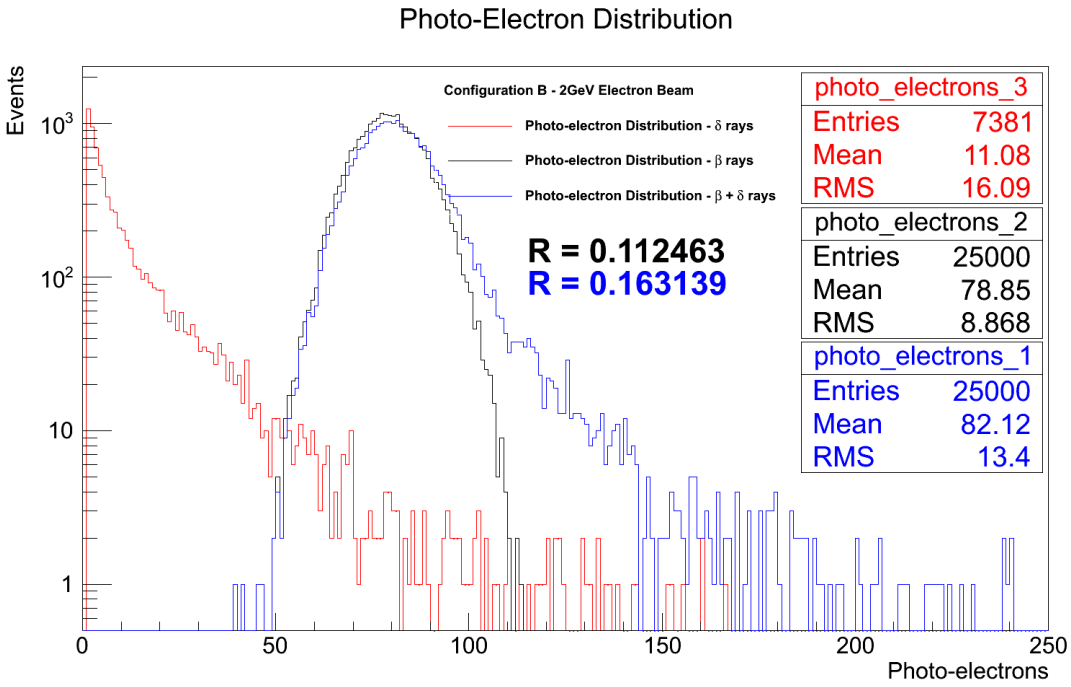

Figure 13: Simulated photoelectron (PE) distribution in QSIM for an early PREX-II/CREX design. Black PE distribution is coming from the primary electrons (β rays). Red distribution is coming from secondary electrons (δ rays) electrons. Blue Distribution is the total distribution ($\beta + \delta$). The signal from the beam is almost a perfect Gaussian as expected from a detector with perfect resolution where the error is only due by statistics. The Landau tail comes from the delta rays and tends to blow-up the detector's finite resolution.

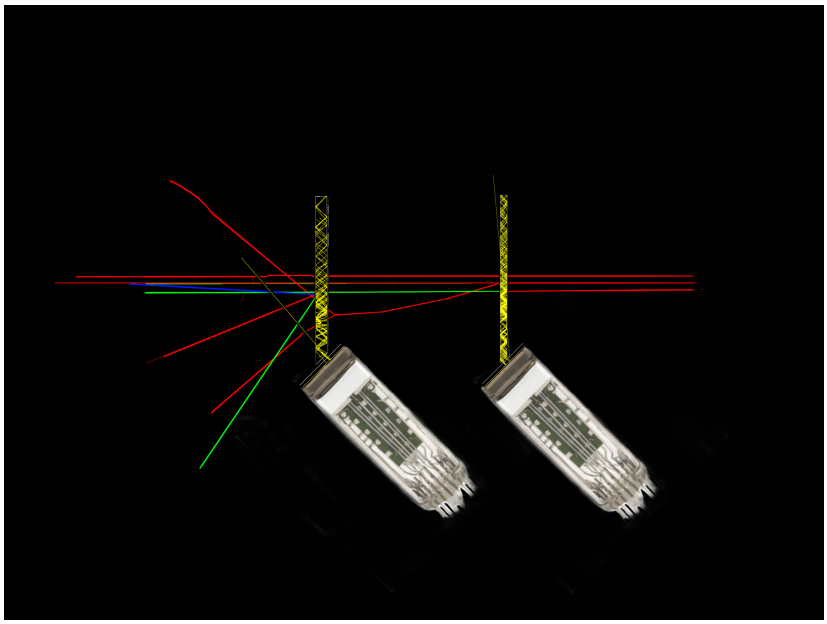

Figure 14: PREX-II/CREX tandem detector concept displaying particle trajectories producing Cerenkov photons (yellow) inside the quartz pieces. Notice the secondary electrons (delta rays) created by interactions of the primary electron beam with the medium. The primary electrons (red lines with straight trajectories in the picture) can emit gamma radiation (green lines) when being decelerated (Bremsstrahlung) and release secondary electrons by ionization. The gammas can pair produce electron-positron pairs (positron trajectory in blue).

Considering the importance of the choice of quartz thickness in the PREX-II/CREX detector, a tandem detector design was favored over a single detector (see Figure 14). With the tandem detector, we have the possibility of having two pieces of quartz of different thicknesses, 6 mm and 10 mm. A thinner quartz would reduce delta rays production and hence the, Landau tail. A thicker quartz would provide a greater light yield. Additionally having two quartz pieces and two PMTs per detector would provide a level of redundancy.

1.5.4 Total Internal Reflection

Total internal reflection occurs when a photon strikes a medium boundary at an angle larger than a particular critical angle with respect to the normal to the surface. If the

refractive index is lower on the other side of the boundary and the incident angle is greater than the critical angle, the photon cannot pass through and is reflected back internally.

Cerenkov photons, for electrons with velocity $v \approx c$, are emitted at an angle $\theta_C = 46.58$ deg relative to the electron's direction of motion. Using the same index of refraction, Snell's Law states the total internal reflection angle is 43.225 deg. This means that there is a narrow range of angles in which the photons created in the quartz will be trapped via total internal reflection. The total internal reflection inside the quartz piece allows its double functionality as media for light production and its use as a lightguide. For the PREX-II detector configuration, the total internal reflection is broken at the beveled face, which is parallel and close (∼3 mm) from the PMT's window–to maximize the photon detection (see Figure 15 and 16).

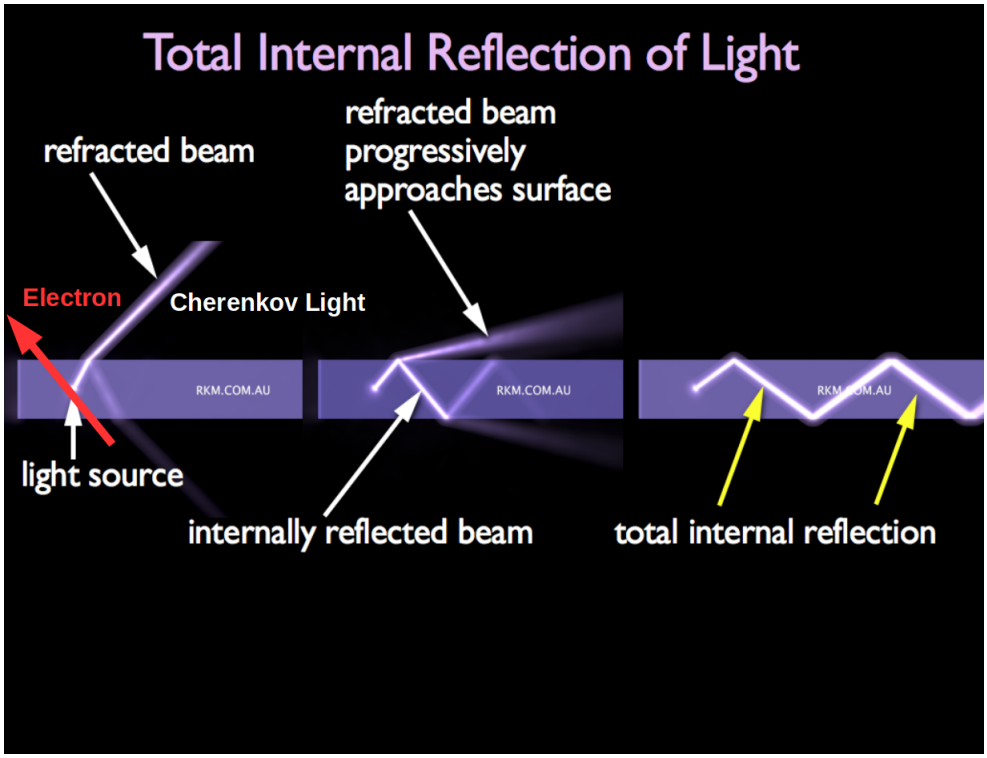

Figure 15: Total internal reflection.

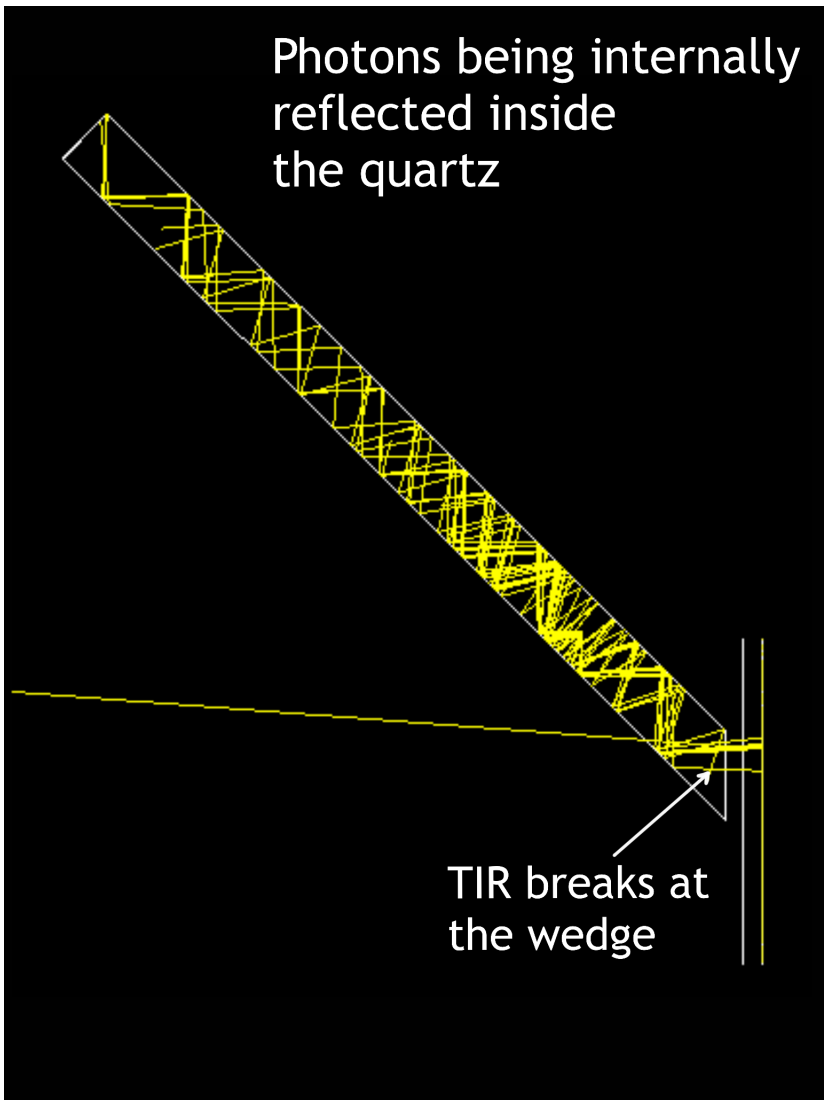

Figure 16: Image of a Monte Carlo simulation of light being internally reflected inside a quartz piece like the one used in PREX-II/CREX detector.

1.6 Other PV quartz-based Detector Development

The PREX-II/CREX main detectors are not the only quartz-based detectors being designed, constructed, and tested by the ISU parity violation group. These thin quartz and other quartz Cerenkov detectors are versatile and have properties that make them an attractive choice for beam monitoring and other applications in high radiation areas. We have been actively developing these other detectors in parallel

with the main PREX-II/CREX detector development.

These detectors include:

- The Small Angle Monitors (SAMs): A set of eight thin quartz detectors positioned around the beamline downstream of the target. These monitor the beam-target luminosity and "parity quality" of the beam. Historically, previous versions of these detectors have not worked well and thus a design overhaul was required for PREX-II and CREX. This detector system is described in detail in Section 4.1.

- The Shower-max benchmarking prototype for MOLLER. This is a quartz tungsten layered sampling calorimeter used to measure a parity violating asymmetry with an energy-weighted signal amplitude. This detector design along with test-beam results and simulation comparisons are given in Section 4.4.2

As with the PREX-II/CREX main detectors, the design development and optimization of these detectors will rely heavily on the QSIM optical Monte Carlo. In particular, the complexity of the Shower-max sampling calorimeter requires a mature and validated simulation in order to confidently understand and optimize the detector design. Details of the optical Monte Carlo, Quartz Simulation (QSIM), are given in the next two Chapters.

2 Detector Material Optical Properties and PMT Characteristics

In the previous section we discussed how we can use the Cerenkov effect and the TIR of light in quartz to build radiation detectors (thin quartz Cerenkov detectors) for precision electroweak experiments. In order to optimize the detectors design, in terms of PE yield and resolution, an accurate and complete understanding of the optical properties of the active medium and photo-sensitive device are required. The following sections detail these properties.

2.1 Optical Processes

In the most simple way, the optical processes, i.e. how light interacts with an optical medium, can by classified in three general categories: Reflection, propagation, and transmission (see figure 17).

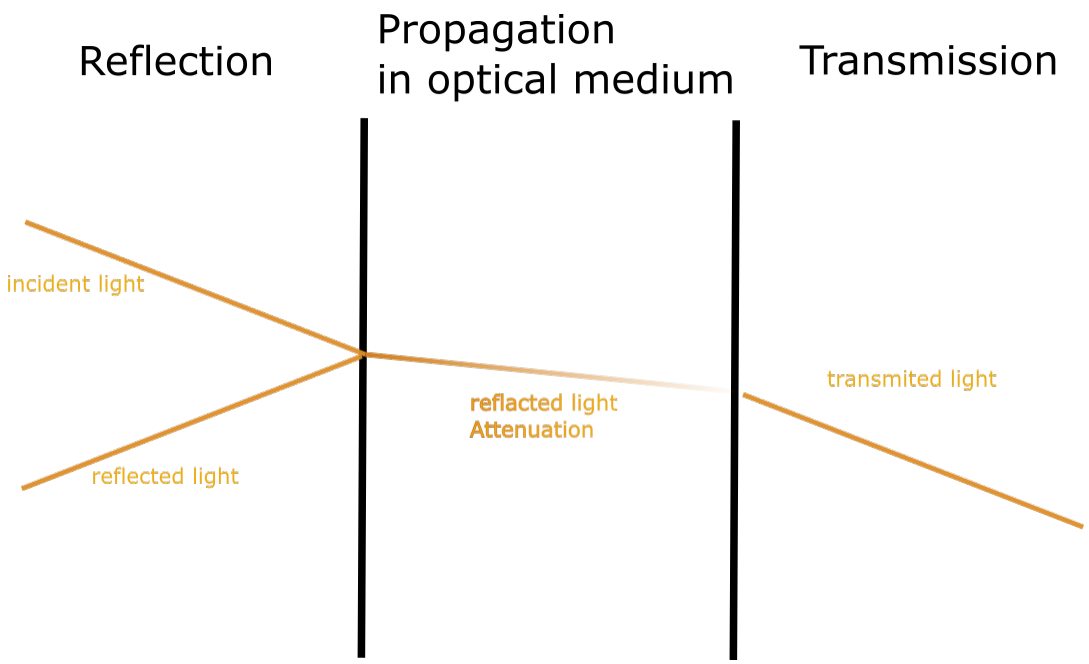

Figure 17: General Optical Processes.

The processes in optical medium can be:

- Refraction: Causes the light to propagate with smaller velocity than in free space. This reduction of velocity leads to the bending of light rays at interfaces described by Snell's law of refraction.
- Absorption: Causes an attenuation of the light. This occurs during the propagation if the light's frequency is resonant with the atomic energy levels in the optical medium. Absorption can be selective, for example rubies are red because they absorb blue and green light.
- Transmission: The non-absorbed light will naturally be transmitted.
- Scattering: This is the phenomenon in which light changes direction of travel and possibly also its frequency after being scattered by the atoms. The total number of photons remain constant, but the number going in the forward direction decreases because light is redirected in other directions. Scattering therefore can have the same effect as absorption. The scattering is elastic if the frequency of the scattered light is unchanged, and it is inelastic, if the photon's energy changes in the scattering.

2.2 Optical Coefficients

Many of the processes mentioned above can be quantified by a number of parameters that determine the properties of the medium at a macroscopic level.

The reflection at a particular surface is described by the surface's coefficient of reflection or reflectivity, R, and it is defined as the ratio of the reflected power to the power incident of the surface (electromagnetic waves carry energy proportional to the electric field squared). The coefficient of transmission, T, is defined as the ratio of

the transmitted energy to the incident energy carried by the photons. If there is no absorption or scattering, then, by conservation of energy, $R + T = 1$ [12].

The propagation of light through a transparent medium is described by the refractive index, n. This is defined by the ratio of the velocity of light in vacuum, c, to the velocity of light in the medium, v, according to $n = c/v$ [12]. The refractive index depends on the photon frequency, this is called dispersion. In colorless materials like glass, the dispersion is small in the visible spectrum, and therefore it makes sense to have a single unique refractive index for that material. However, for our precision simulations, the dispersive nature of the refractive index is very important and is further discussed in the next section.

The absorption of the light by an optical medium is quantified by its absorption coefficient, α. This is the fraction of the photon energy absorbed in a unit length of the medium[12]. Conversely, the inverse of the absorption coefficient, the absorption length, is the average distance a photon travels in the medium before being absorbed.

If the beam is traveling in the z direction, and the intensity at the position, z is $I(z)$, then the reduction in intensity for an infinitesimal propagation distance dz is $dI = -\alpha dz I(z)$. Integration gives us the Beer law[12]:

$$I(z) = I_0 e^{-\alpha z} \tag{15}$$

The absorption coefficient may also have a strong dependence on frequency such that an optical medium may absorb one color but not another. However, our high-purity quartz has very uniform absorption coefficients across the UV to visible spectrum.

2.3 Optical Materials

2.3.1 Quartz Optical Properties

Glasses are important optical materials, and they have been used for centuries in the elaboration of prisms and lenses in optical instruments, in addition to their more common uses in windows and glassware [12]. Most types of glasses are made from fused silica sand (SiO_2), commonly know as quartz, with other chemicals. Spectrosil 2000 is an ultra-high pure quartz (chemical purity over 99.9%). Pure silica is transparent in the visible region, absorbs in the deep ultraviolet due to electric transitions of the SiO_2 molecule, and absorbs in the infrared due to vibrational modes (see Figure 18). The transparency range thus goes from around 180 nm in the ultraviolet to beyond 2000 nm in the infrared.

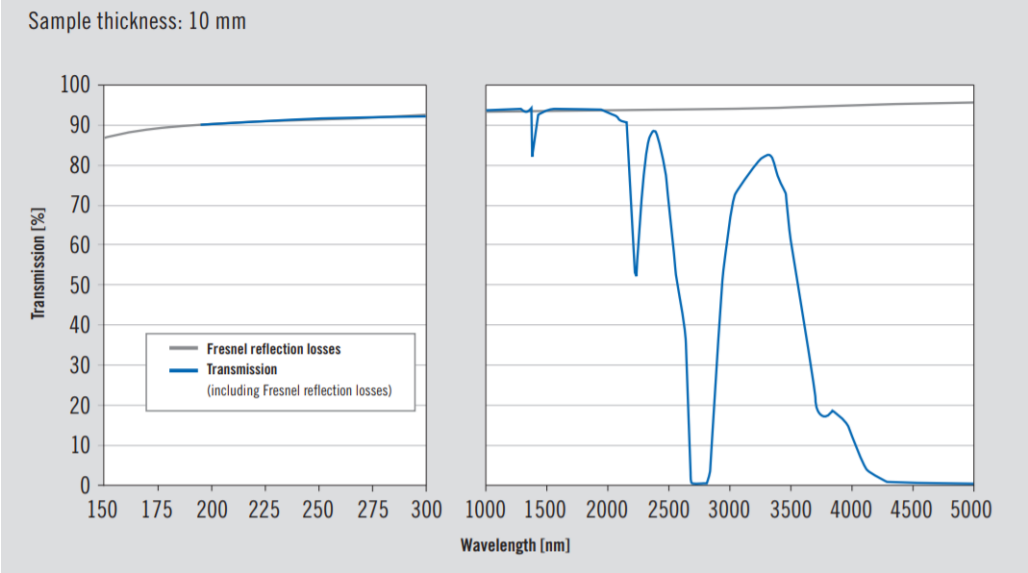

Figure 18: Spectrosil 2000 transmission.

The PREX-II/CREX and MOLLER experiments use Spectrosil 2000, a type III synthetic fused silica quartz crystal (it is produced by the hydrolyzation of $SiCl_4$ when sprayed into an OH flame). Spectrosil 2000 is a very homogeneous synthetic fused silica glass for deep UV optical applications. Spectrosil 2000 is chlorine-free, free

of bubbles and inclusions and due to its ultra-high purity, has an exceptional optical transmission in the deep ultraviolet and visible, with a useful range from below 180 nm through 2000 nm.

The refractive index increases with photon's energy in the near infrared and visible spectrum. This dispersion is due mainly by the interband absorption (absorption of light by electrons when exciting them to the conducting band) in the ultraviolet whose effect, despite being very small in the visible region, is still noticeable [12]. In the near infrared, the dispersion is also influenced by the vibrational absorption at the lower frequency (see figure 19).

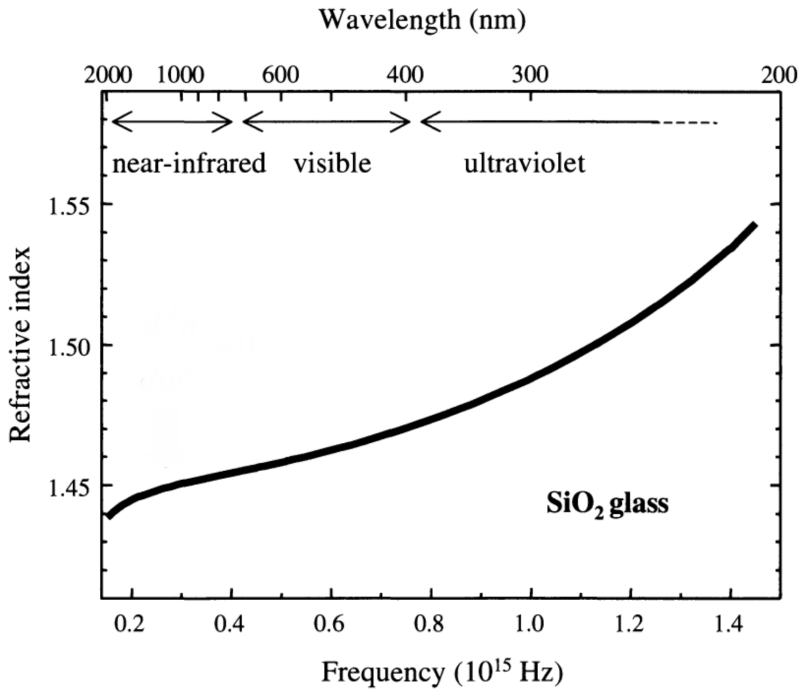

Figure 19: SiO_2 refractive index in the near infrared, visible and ultraviolet regions[13].

The Quartz simulation, QSIM, needs parametrizations for the optical properties of this quartz. These optical properties are the index of refraction[14] (Figure 20) and the absorption length[15] (Figure 21). The parametrization of the index of refraction

is:

$$n = 1.438 + (0.01197 E_\gamma/eV) - (0.001955 E_\gamma^2/eV^2) + (0.0004793 E_\gamma^3/eV^3) \qquad (16)$$

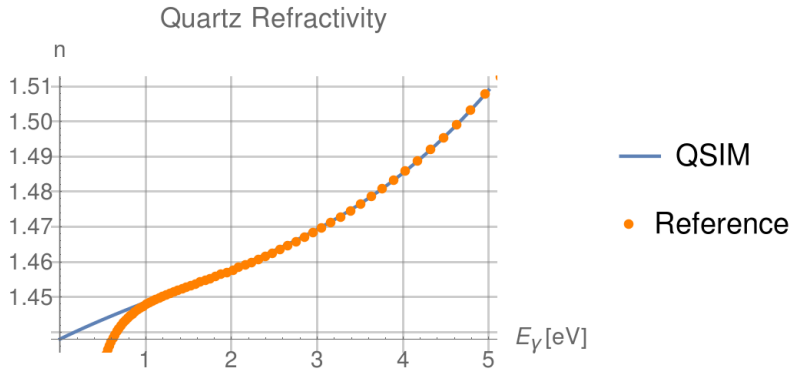

Figure 20: Quartz refractivity. Orange: Reference [14]. Blue: Parametrization used in QSIM.

The parametrization of the absorption length is

$$l = (e^{4.325} \times e^{1.191 E_\gamma/eV} \times e^{-0.213 E_\gamma^2/eV^2} \times e^{-0.04086 E_\gamma^3/eV^3}) m \qquad (17)$$

Figure 21 shows how this parametrization compares with other absorption indices with similar type-III quartz crystals.

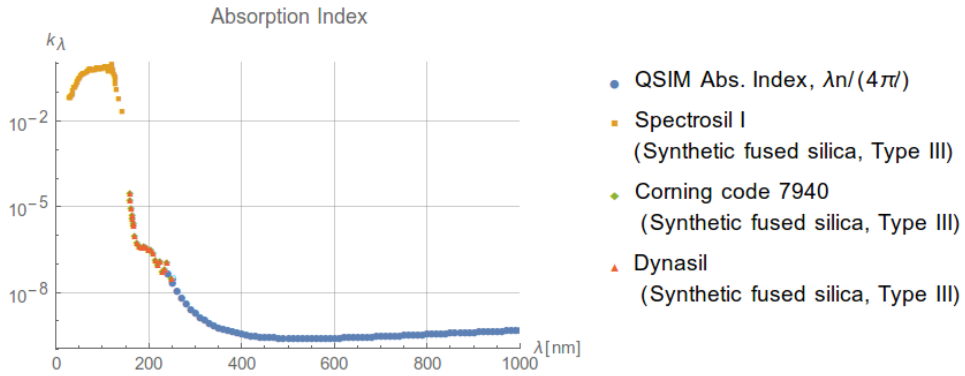

Figure 21: Quartz absorption index. Parametrization used in QSIM (Blue) compared with similar crystals reported in the literature.

The absorption index, k_λ is related to the absorption length, l, by

$$k_\lambda = \frac{\lambda n}{4\pi l} \tag{18}$$

where n is the refraction index and λ is the wavelength. We could not find references that report quartz absorption indexes above 225 nm, so we extrapolate values assuming an exponential decay law (Beer-Lambert law).

2.3.2 Radiation Effects Over Quartz Transparency

It is important for the experiments that the quartz transparency is not affected by exposure to radiation. If it turns opaque (due to radiation damage), the photon yield will be reduced. A measurement of the deuterium lamp spectrum transmitted through quartz was performed before and after the exposure of the quartz sample to a 8 MeV, 250 Hz electron beam from the 25B RF Linac accelerator at the IAC. The quartz sample, a 2.5 cm x 2 cm x 1.5 cm rectangle with a small bevel on one side-corner, was irradiated for 3, 8 and then 16 minute intervals.

In order to make a quantitative study of the affects of the radiation in quartz, an accurate calibration of the dose levels provided by the 25B Linac electron beam had to be made. Connor Harper did such a study using Optical Stimulated Luminescence dosimeters named NanoDot OSL [16]. These dosimeters consist of small carbon-doped aluminum oxide crystals. The electrons and Bremsstrahlung photons would deposit energy in the crystal by ionization of the lattice structure. Once the dosimeter is removed from the radiation source (electron beam), the dosimeter is exposed to a stimulating green light, this causes the crystal to luminesce blue light. After passing through a blue filter, the photons are detected by a PMT. The amount of light detected is proportional to the dose deposited in the dosimeter. The dosimeters were calibrated using a Cesium-137 source with a very well known activity, so the quartz

dose exposures can be calculated with accuracy.

During the irradiation test, the dose per beam pulse was calculated to be 253 Rad/pulse. This corresponds to ∼11 MRad, 30 MRad and 61 MRad of cumulative exposure for 3, 8, and 16 minutes, respectively (see Figure 22).

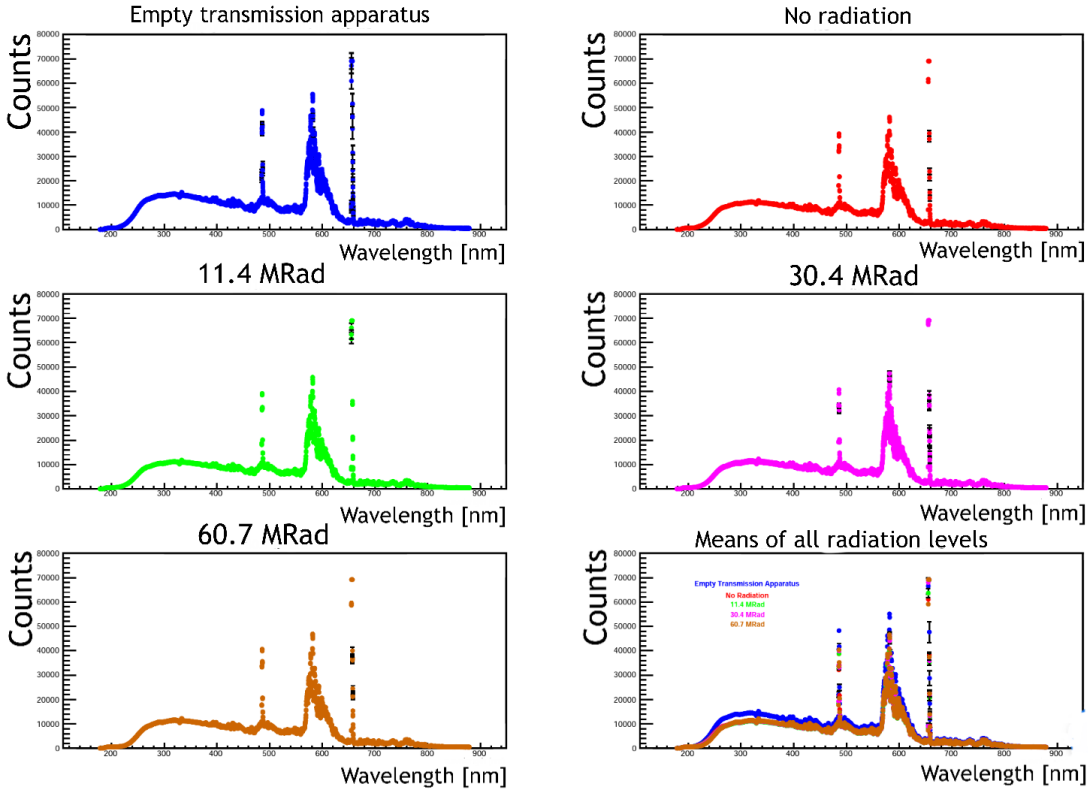

Figure 22: Light spectrum from a deuterium lamp after being transmitted though quartz, before and after the 11 MRad, 30 MRad and 61 MRad cumulative exposures.

The difference between the spectra before and after the irradiation is shown in Figure 23:

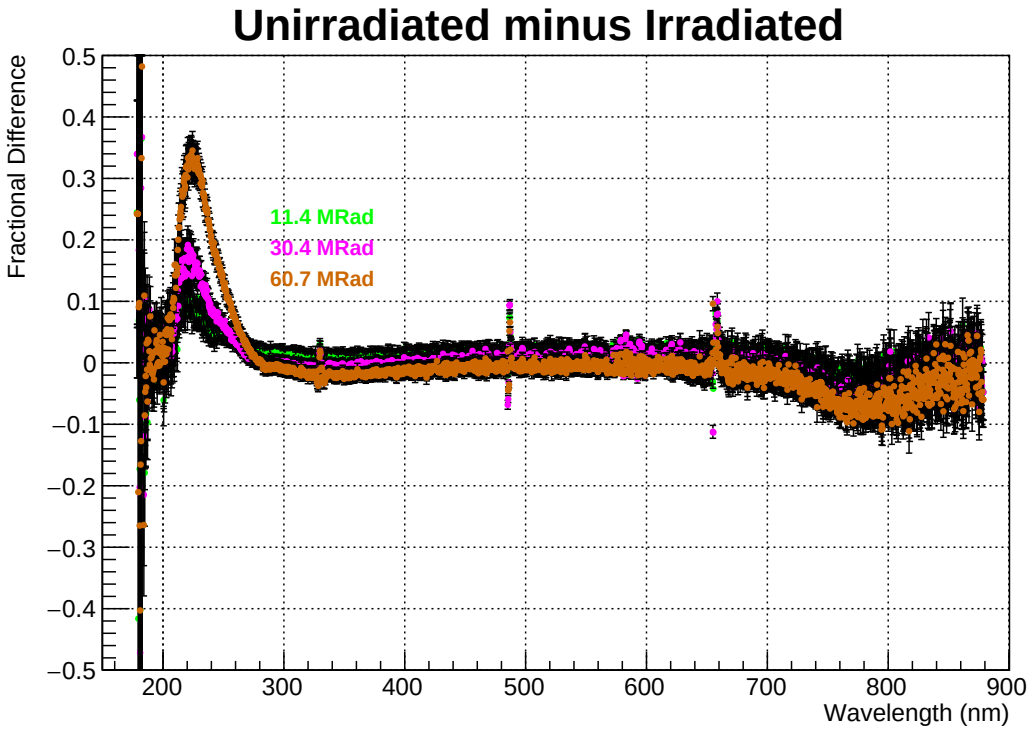

Figure 23: Relative change in quartz transparency as a function of wavelength observed during irradiation study.

As a consequence of apparent radiation damage, there is a noticeable decrease in transparency observed for wavelengths below ∼270 nm (Figure 23). However these consequences are reduced by the following three facts: The PMT's quantum efficiency is rapidly diminishing in the damaged region of the spectrum, UV light is strongly absorbed by the oxygen present in the air at wavelengths bellow 200nm (as the ozone layer absorbs sun's UV radiation [17]) and, in the case of having lightguides, their reflectivity is very low at the wavelength range where we observed radiation damage in the quartz transmission. The results in Figure 23 are preliminary and future irradiation studies will be conducted to verify and further investigate them.

2.3.3 Glass Grinding and Polish

Fused silica quartz is a material that can be machined, polished, blown or welded. Custom shapes can be made according to customer needs, from simple quartz tiles to more complicated welded assemblies. Finishing is usually done by grinding, fire polishing or even mechanical polishing [18].

Due to the fact that quartz is a brittle material and a superior surface polish is demanded for optical applications, the industrial grinding process is difficult and therefore expensive. Spectrosil 2000 is polished using a standard mechanical procedure with progressively finer and finer grits.

Usually the polish grade is quantified by the Total Indicated Reading, TIR (don't mistake it the total internal reflection), which is the difference between the maximum and minimum measurements of the surface with respect to the nominal surface plane (see Figure 24).

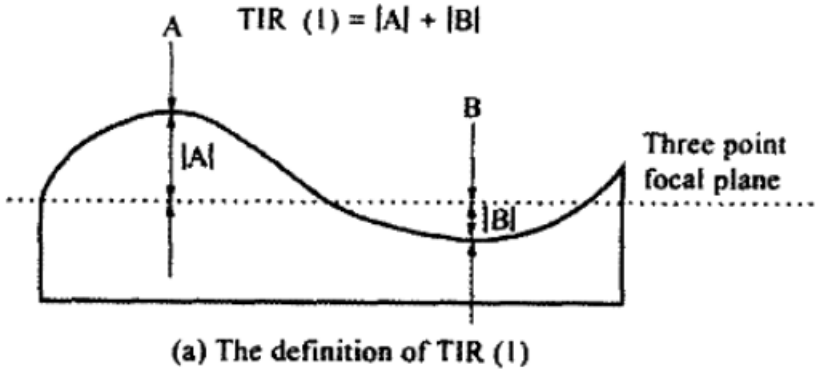

Figure 24: Definition of TIR: An industry standard quantity that represents the amount of deviation from surface flatness.

For the quartz tiles used in our experiment (see Figure 25), we requested a TIR of 20 Angstroms or better. The precision of the faces parallelism is 3 arc minutes (primary faces) and their perpendicularity 15 arc minutes. This provides a (near)

perfect optical-grade polish and geometry to give total internal reflection inside the crystal for the Cerenkov photons. We also request a specification on the maximum number and size of any possible surface chips in the quartz piece (these can and do occur during the cutting and/or polishing part of manufacturing). Finally, there is also a parallelism specification between opposite surfaces and therefore 90° angles at all corners (except the 45° bevel-cut end).

Figure 25: Polished quartz tiles for PREX-II/CREX detector.

Ideally, there must not be any material touching the surface and it must be free from scratches, dust, and finger marks. The mechanical polishing should involve movements along the intended photons travel direction, in this case, along the quartz tile surface. Particularly for long thin quartz pieces the quality of the surface is extremely critical. Considering the above, the optical surface properties of the quartz depend greatly on the quality and consistency of the manufacturer's polishing procedure. We expect that all the quartz pieces purchased from the same manufacturer will have close optical properties but not identical.

2.4 Reflective Metals

The shiny appearance of metals arises from their characteristic high reflection coefficients at all wavelengths in the visible region of the spectrum. The elevated reflectivity is the result of the interaction of light with free electrons that exist in the metal[12].

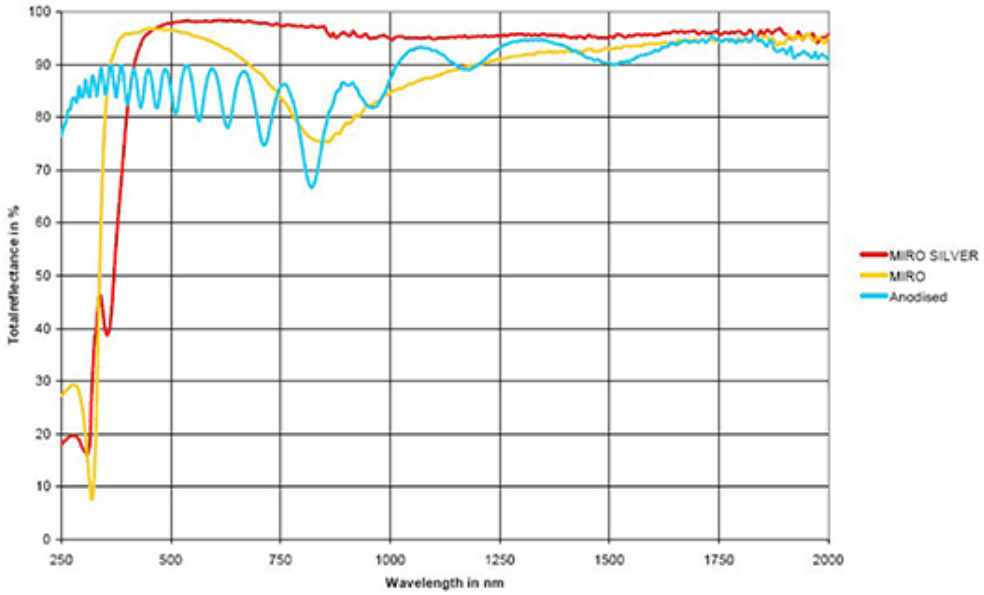

Figure 26: Example of manufacturer reflectivity measurements for different metal sheets commonly used for lightguides. These reflectivities are only for normal (or 90 deg) incidence.

The reflectivities of different aluminum sheets used to make lightguides are shown in Figure 26. The reflectivity is close to 100% (at a $\sim$ 90 deg incident angle) in the infrared and visible spectral region. The reflectivity then decreases considerably in the ultraviolet region[12]. This is a general characteristic for most metals. The cutoff frequency in the ultraviolet region is called plasma frequency, ω_p[12]. For $\omega < \omega_p$ incident electromagnetic waves in a plasma take the form of decaying stationary waves, rather than propagating waves. Therefore, for a frequency less than the plasma frequency, the electromagnetic wave will not propagate through the plasma. Instead, it will be totally reflected[19].

Metals reflect infrared and visible wavelengths, but partially transmit ultraviolet wavelengths (typically photons with energies with more of 10 eV). Because the Cerenkov light spectrum lies in the near ultraviolet and visible region, the metal chosen for the lightguide should have a plasma frequency as high as possible and special care in the lightguide design should be taken in order to reduce the number of reflections a photon should have before reaching the PMT (so-called "one-bounce" designs). Aluminum reflectors are rarely used without a coating over their surfaces, primarily for oxidation protection, but also to enhance reflectivity–often in the visible region which is the case for silver-containing coatings. These layers change the reflectivity of natural aluminum and oxidation protection layers can create undulations in the reflectivity from thin-film interference phenomena.

2.4.1 Reflectivity Measurements

Reflectivity measurements of the MIRO-27 and UVS mirrors at different incidence angles, before and after irradiation, were done using the Ocean Optics Flame spectrometer (UV-VIS grating configuration with a 2048 channel CCD light sensor) and the HD-2000 UV light-source (deuterium bulb–it has stable output from 190 nm to 2500 nm at 25W). A calibration mirror (NIST calibrated, aluminum on fused silica substrate) of known reflectivity ($\sim$ 87% at 250 nm - 93% at 1000 nm)[3] was used to measure a baseline reflectivity spectrum. The calibrated baseline reflected spectrum then allowed for absolute reflectivity measurements of our various lightguide samples (see Figure 27).

[3] "Values are calibrated at a 6 deg angle traceable to NIST and are included with the standard mirror in a calibration file on CD."

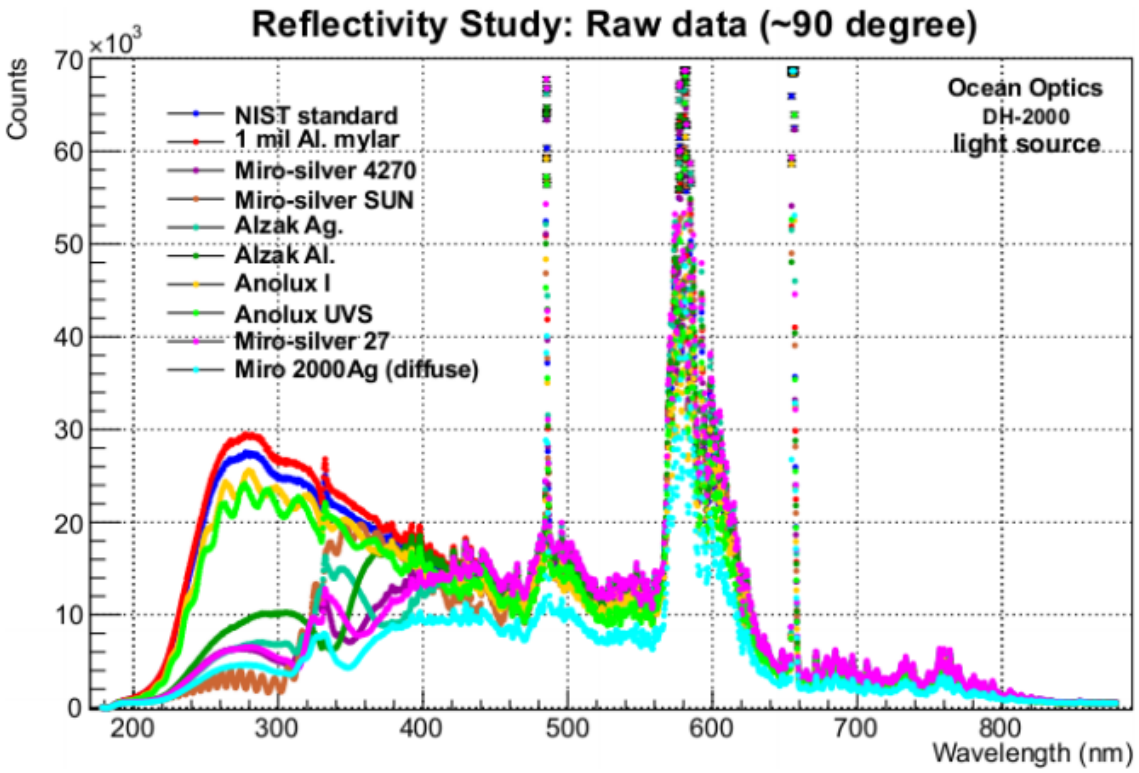

Figure 27: Measured spectrum reflected by different reflecting surfaces commonly used to make mirrors. The NIST standard is the reference mirror used for an absolute reflectivity calibration.

An irradiation study of different lightguide material performance was performed at the Idaho Accelerator Center (IAC). The material's reflectivity (for normal incidence) was measured after being exposed to an 8 MeV electron beam. The Linac that provided the beam can be operated up to 25 MeV, between 65 to 110 mA peak current, with a 4 μs pulse width, and with a repetition rate of 250 Hz.

The energy deposited in the reflective mirrors at 8 MeV is almost all due to inelastic collisions between the electrons and the mirror (11.9 MeV/cm). With a current of 65 mA at 150 Hz, the estimated deposited power is 22 W and gives a dose rate of 1.3 Mrad/s (Figure 28).

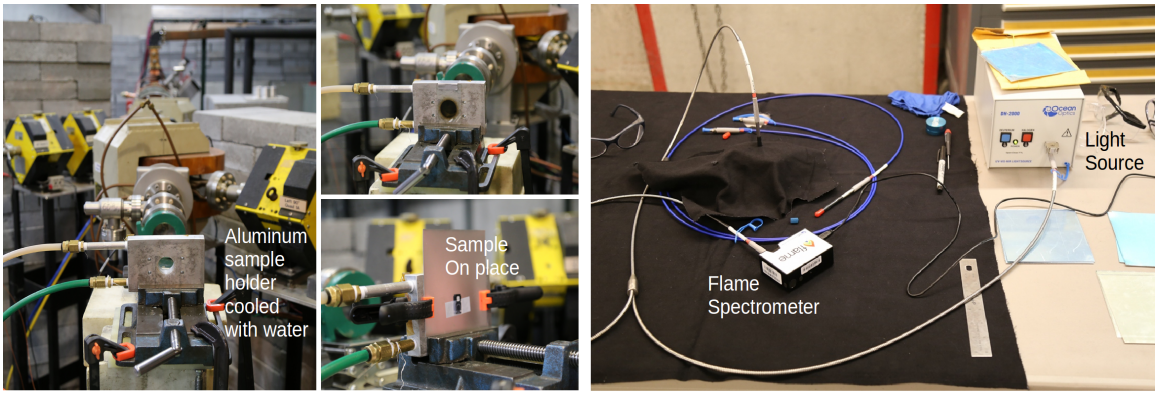

Figure 28: Irradiation study at IAC. The mirror sample is irradiated with a 8 MeV electron beam depositing a dose of 1.3 Mrad/s.

Figure 29 shows the reflectivity for two mirrors, UVS and MIRO-27, before and after irradiation. As it can be seen in the plots, the materials tested do not show significant detriment in their reflectivity. They show robustness against high radiation environments. This is a fundamental requirement for their application in experiments where they will exposed to high doses.

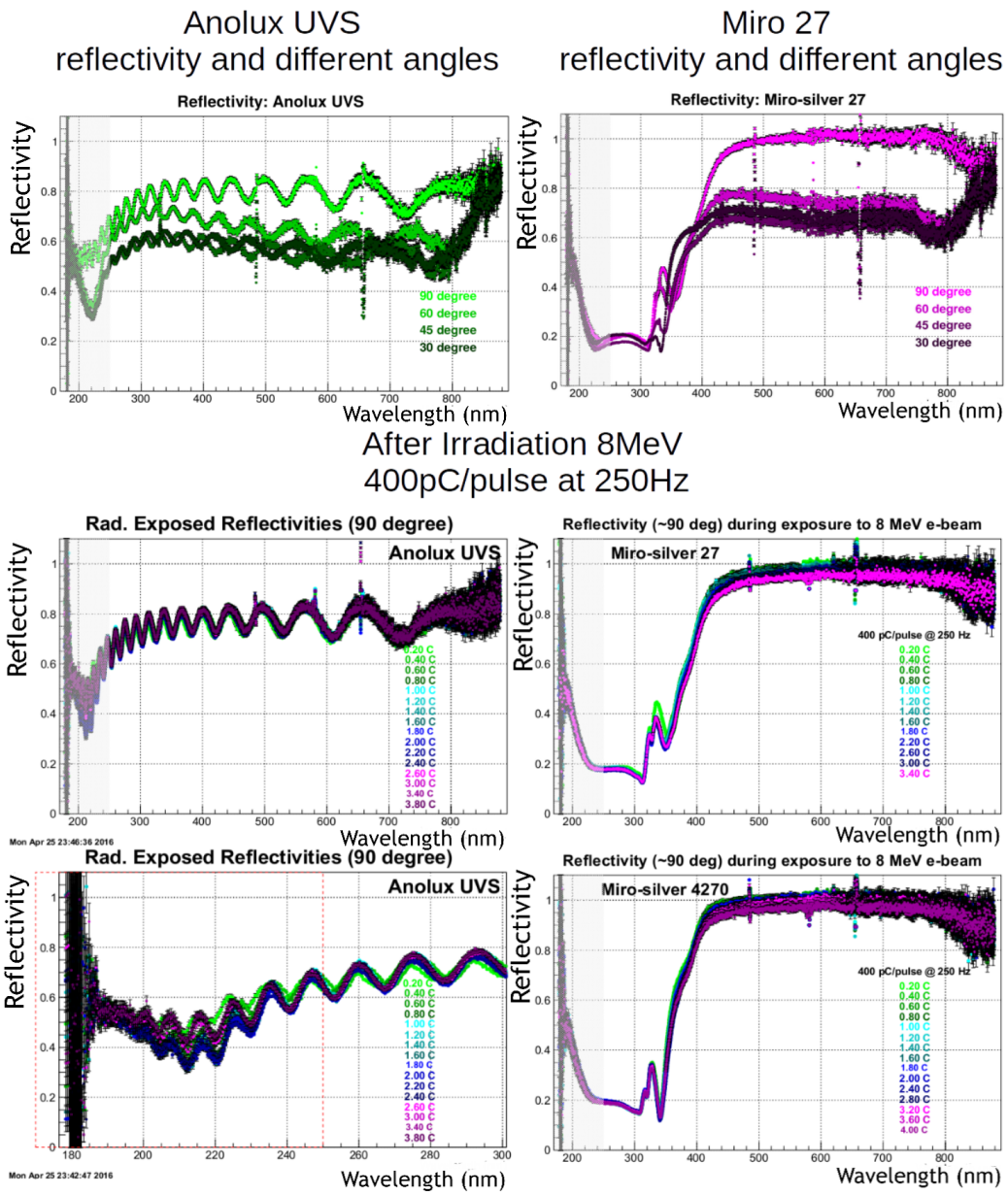

Figure 29: UVS and MIRO 27 light guide specular reflectivity measurements at four different angles (90, 60, 45, and 30 deg). The top set of plots show results prior to any radiation exposure. The bottom plots show the results (90 deg only) following several successive exposures. Dose exposure could not be calibrated precisely during this first-time, "engineering" run due to saturated dosimetry measurements. In general, no noticeable change in 90 deg specular reflectivity was observed for very high dose exposures.

2.5 PMT Characteristics

The photo-multiplier tube (PMT) is a photo sensitive device; simply put, a PMT is a device that converts light into an electric signal. It can provide extremely high sensitivity, low noise, a fast response, and variable amounts of amplification. It can detect photons at extremely low light levels, even single photons, and it's response can remain quite linear, even when scaling to billions of detected photons per second. These characteristics make the PMT an ideal device to pair with the our detector's Cerenkov radiators.

The PMT consists of a photocathode, where incident photons are converted to photoelectrons (PEs) with a quantum efficiency Q_e, and an electron multiplier (dynode) chain for amplification. The photocathode and dynode chain are all inside a vacuum tube. The photocathode consists of a thin metal film deposited on the inside surface of the PMT window. The dynode chain consists of 10 stages of progressive amplification which, in the end, essentially multiplies every PE by a common gain factor (typically 10^3 to 10^6) thus creating a measurable charge pulse from the PMTs anode signal output.

Q_e is defined as the ratio of the number of emitted photoelectrons, n_e, to the number of incident photons, n_p, that is, $Q_e = n_e/n_p$. However, there are some optical characteristics regarding the photocathode: The photocathode is glossy and a fraction of photons should be reflected at its front surface, however it still transmits most of the light. Typical PMT Q_e's are in the range of 25% for blue (400 nm) light. And typical cathode reflectivities for bialkali photocathodes are around 10%. These details are further discussed in the next subsection.

Most PMT applications, whether in research or in industry, are served by just three photocathode types: bialkali (KCsSb), rubidium bialkali (RbCsSb) and S20 (NaKSbCs)[20]. Each of these has a different spectral response: bialkali is more

sensitive in the UV range in comparison to the other two types, rubidium is more sensitive in the visible range, and the S20 can cover the infrared range better than the other two. All three types are sensitive in the UV region (to different degrees), but that characteristic is lost if the PMT window is made of borosilicate glass, which absorbs the UV light. In order to enhance UV detection, a UV-transmitting window such as fused silica is required.

The PMT we use has a bialkali "transmission" photocathode. The physical principles which form the operational basis for this type of photocathode can be explained with the energy band diagram of Figure 30.

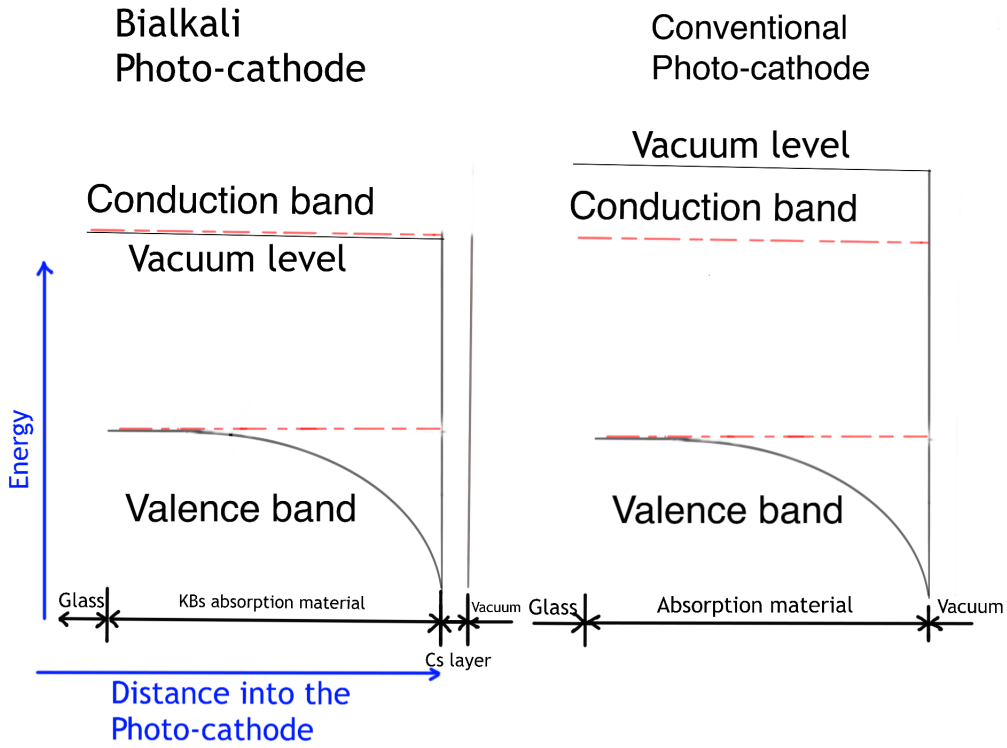

Figure 30: Energy level diagrams of a bialkali photocathode (left) and a conventional photocathode (right). Notice how close the conduction band is to the vacuum level for the bialkali photocathode, the electrons, excited to the conduction band by the absorption of Cerenkov photons, would escape easily to the vacuum inside the PMT.

When photons are absorbed in the K-Sb layer, electrons from the valence band are

elevated into the conduction band. In order to escape to vacuum, the electrons must travel through the material and overcome the energy barrier (vacuum level) at the boundary. In other to do this, they should have an energy greater than the vacuum level.

The high efficiency of the K-Sb-Cs derives from the fact that electrons near the bottom of the conduction band can diffuse large distances and the vacuum level is only slightly less (or ∼equal) to the bottom of the conduction band. These types of materials are called negative electron affinity photocathodes[21].

By contrast, in a conventional photocathode, the energy of the vacuum lies above the energy of the bottom of the conduction band. The excited electrons would lose energy rapidly, going below the vacuum level, before reaching the surface, and therefore, only the electrons produced near the surface can escape to the vacuum and contribute to the signal.

Apart from the optical properties of the materials used to make our thin quartz detectors, i.e. quartz pieces, wrapping materials and lightguides, the optical properties of the photocathode are of utmost importance. These properties are the photocathode absorption (closely related to the quantum efficiency), reflection, and transmission.

2.5.1 Photocathode Reflectivity

In a transmission PMT, like the ones we use, the photocathode is made of a thin layer of bialkali material which is applied by evaporation as a coating on the back side of the PMT quartz window during manufacturing (Figure 31). When a photon is absorbed inside this thin semiconductor film of thickness $\sim 20nm$, it may release an electron to the vacuum inside the PMT[22, 23].

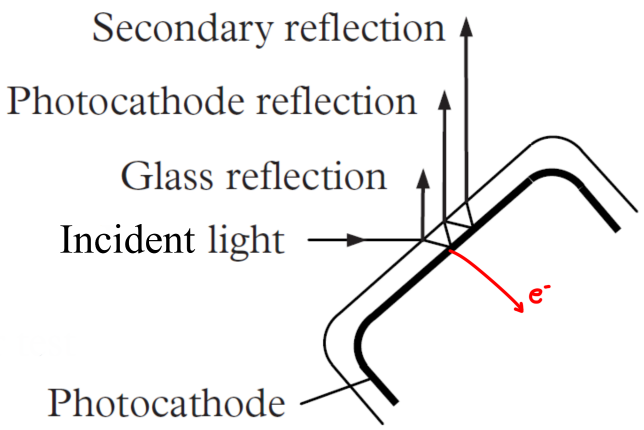

Figure 31: PMT drawing showing multiple reflections on the PMT quartz window - photocathode.

The photocathode in a "transmission" PMT is a thin semi-transparent semiconductor layer on the inside of the vacuum window. The succession of events, when light is incident on the PMT window, is as follows: a small fraction of light is reflected at the air–window interface while the remainder interact with the photocathode layer. Some of these photons are absorbed by the photocathode, others are transmitted through the layer without interaction, and the remainder are reflected. The photocathode thickness is a compromise between maximizing the probability that a photon results in a signal: if it is too thin, little light would be absorbed, on the other hand, if the photocathode is too thick, the photoelectrons cannot escape to vacuum easily.

The optical properties of the photocathode reflectivity, absorption and transmission are functions of the photon energy, angle of incidence, the refractive index of the medium in contact with the PMT window (air in our case) and the refractive index of the photocathode itself.

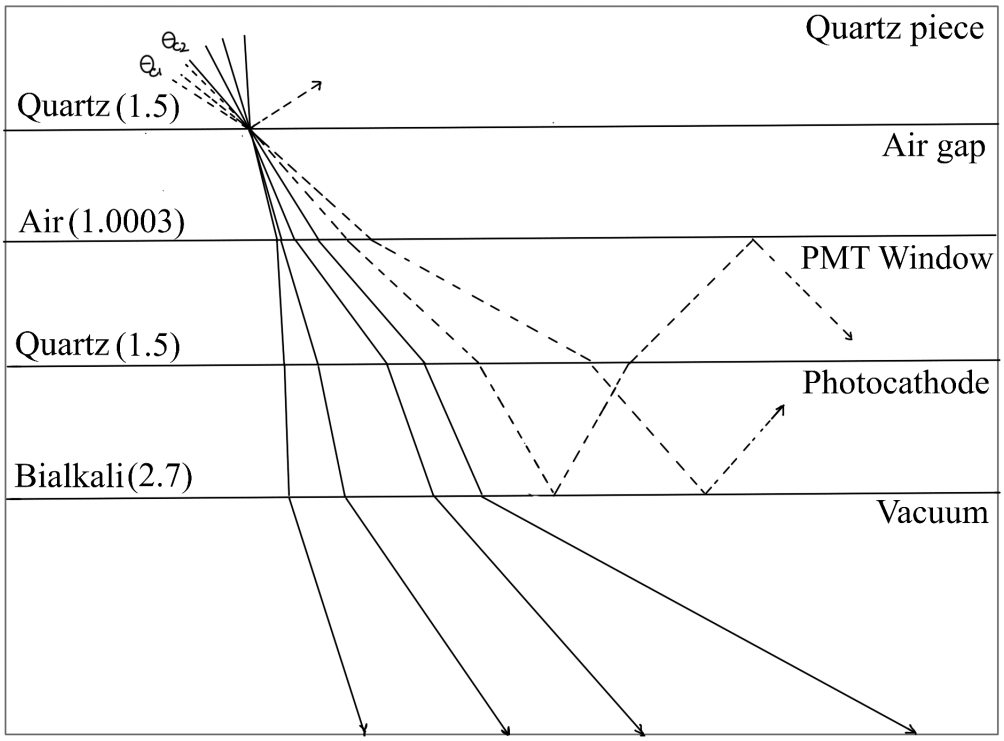

Figure 32: The propagation of light starts at its creation in the form of Cerenkov radiation inside the detector's quartz piece. Then, the light goes through an air gap, the quartz window, the photocathode and into the vacuum (solid lines). Light undergoes TIR at the boundary whenever it propagates from a more dense medium to a less dense medium. Photons internally reflected at the quartz window - photocathode boundary could get extra chances to get absorbed (dashed lines). Partial reflections (not shown) occur at all interfaces and for all incident angles in accordance with the Fresnel equations.

The refractive indices of a PMT window and the photocathode play a fundamental role in the efficient collection of light. Figure 32 shows a schematic of light propagation from the quartz piece or tile, where light is created in the form of Cerenkov radiation. After crossing the air gap between the quartz and the PMT, the light goes through the quartz window and cathode into the PMT's inner vacuum. Snell's law indicates that the angle at which a ray of light emerges after crossing a series of parallel layers depends only on the refractive index of the first and last medium [24]. Since the refractive index of air is just slightly bigger than that of vacuum, the window for TIR

is very narrow. Referring to Figures 32 and 33, we note that all light leaving the quartz tile at an incident angle of $\theta_{c1} \sim 43.603$ deg or less enters the vacuum unless absorbed by the cathode; for angles between $\theta_{c1} \sim 43.603$ deg and $\theta_{c2} \sim 43.619$ deg, light is either absorbed or reflected by the cathode–vacuum interface and returned to the quartz window. At incident angles >43.225 deg, light is reflected at the quartz – air interface and returned to the quartz tile. The difference, $\theta_{c2} - \theta_{c1}$, defines a narrow window for TIR. Due to the quartz refractive index dependence on photon wavelength, there is also some dispersion in the window.

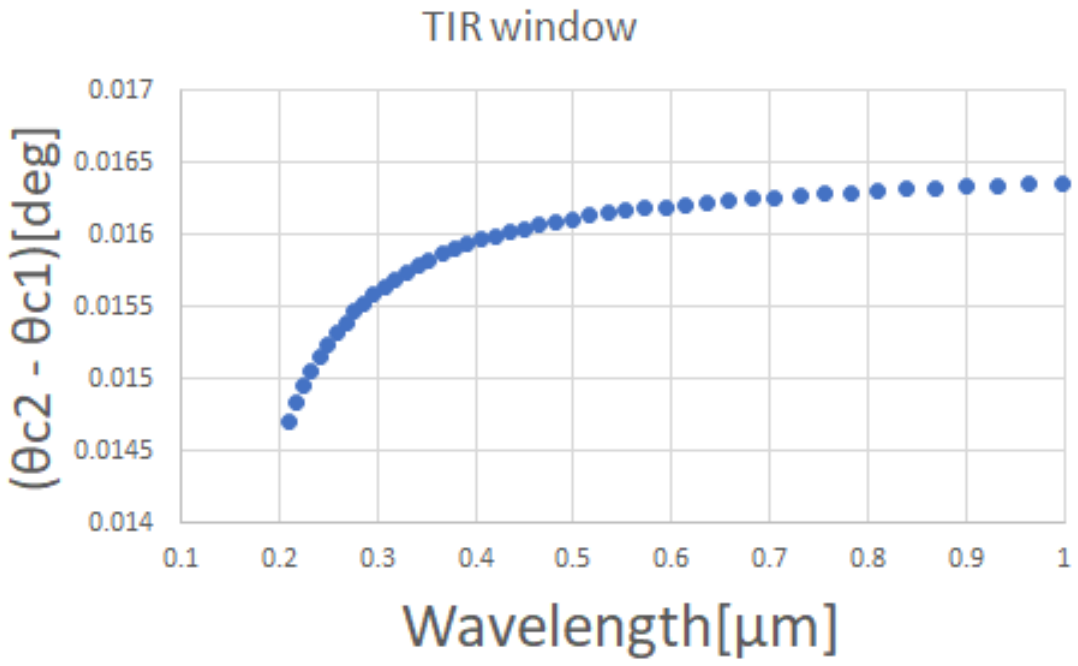

Figure 33: The incident angle window, $\theta_{c2} - \theta_{c1}$, for TIR at the PMT's quartz window and photocathode multi-layer. θ_{c1} is the critical angle for total reflection for multi-layer ($\theta_{c1} = 40.545$ deg for $\lambda = 210$ nm, $\theta_{c1} = 43.47$ deg for $\lambda = 780$ nm). θ_{c2} is the critical angle for total reflection in quartz assuming an air's index of refraction of 1.0003. The window for TIR is very narrow but get bigger at visible and near infrared range due to dispersion of light in quartz.

Note that partial reflections of incident light occur at every optical interface. Fresnel's theory for dielectric materials quantifies these partial reflections. The inclusion

of a photocathode adds complications in the determination of optical constants, i.e. the refractive index of the photocathode, $\boldsymbol{n} = n + ik$, which is a complex quantity because of the absorption in the photocathode (n $\sim$ 2.7 and k $\sim$ 1.5 for bialkali photocathodes[24]). The method adopted by several authors is to make optical measurements on photocathodes at multiple angles and multiple wavelengths for p and s polarized light (the two plane polarized components of the incident light, perpendicular and parallel to the incident plane). The data allow determination of the three constants, n, k, and d. A three-parameter best fit is sought that leads to the most likely set of optical constants.

Measurements of these optical constants are difficult to come by. The only known research into photocathode parameters published by an manufacturer company is from Timan (1976) while working for DuMont Electron Tubes and Devices Corp. Timan determined the refractive index, n , for different wavelengths. More recent publications come from Moorhead and Tanner (1996) [25, 26], for a Thorn-EMI 9124B PMT submerged in water (they mimicked the operation of the PMTs to be used in the Sudbury Neutrino Observatory) at a wavelength of 442 nm and at various angles of incidence. D. Motta and S. Schonert (2004) [24] measured the absolute reflectivity at near normal incidence for the bialkali photocathodes of 1.5 inch diameter 9102B and 9902B PMTs from ETL (Electron Tubes Limited) in air and water. The former equipped with a blue sensitive KCsSb bialkali photocathode. They were able to formulate the set of n, k, and d parameters as a function of the wavelength from 380 nm to 680 nm. Knowledge of these constants leads to the reflectivity, transmission, and absorption (see Figure 34).

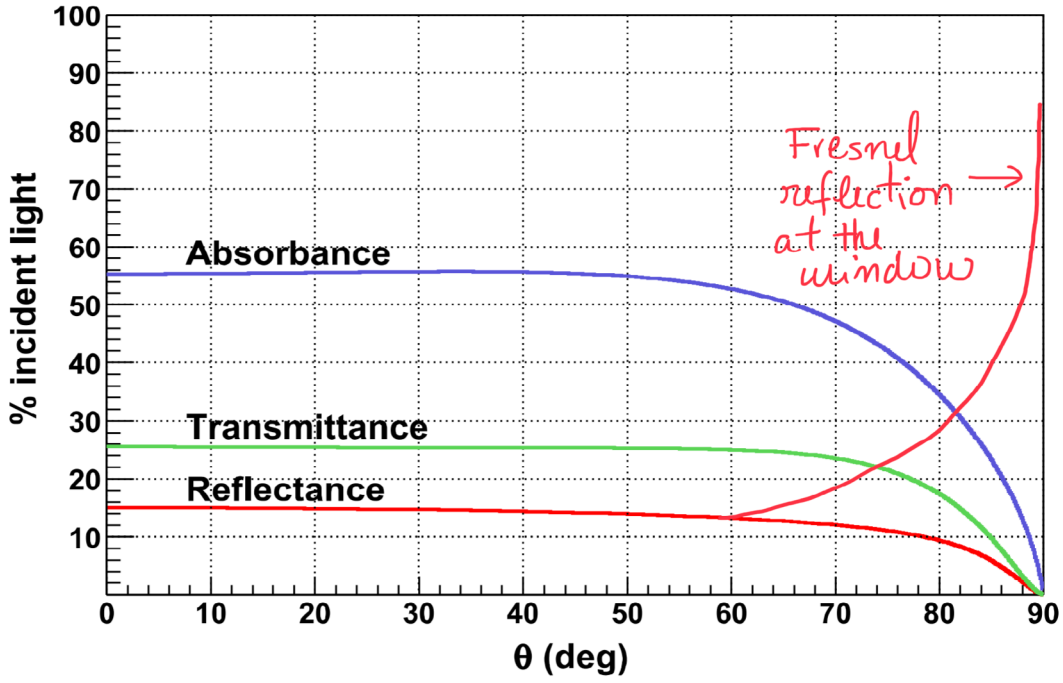

Figure 34: Bialkali photocathode absorption, transmission and reflectivity as function of the incident angle θ reported by Motta [24]. The Fresnel reflection at the quartz window was added by hand for illustration purposes.

The reflectivity of a bialkali photocathode, illustrated in Figure 34, was reported by D. Motta [24]. The cathode reflectivity reported in Figure 34 is approximately constant, 12.5% for angles of incidence, $\theta_i \leq 60\%$, and then drops to 0% without taking into account the contribution of the Fresnel reflection at the quartz window, which would increase rapidly to 100%.

2.5.2 PMT Quantum Efficiency

The photocathode quantum efficiency (QE) dictates a PMT's spectral photo-emission efficiency. It is defined as the ratio of the number of photoelectrons emitted by the cathode to the number of photons with specific wavelength incident on the window, and is usually expressed as a percentage. In QSIM, the quantum efficiency is included as a property of the cathode (sensitive) detecting surface (dielectric-metal interface).

The Hamamatsu R7723Q PMT (see Figure 35) is sensitive to photons with wavelengths between 160 - 700 nm (1.77 - 7.75 eV), so we limit optical property tables in QSIM to this range.

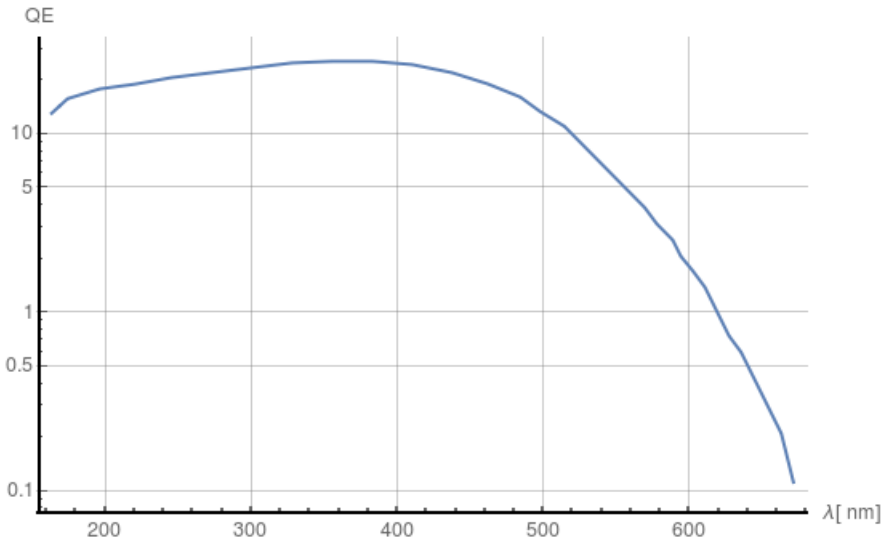

Figure 35: R7723Q Quantum efficiency, presented as a percentage, as function of the photon wavelength. The QE peaks at ∼25% near blue light wavelengths [27].

2.5.3 PMT Linearity

In a general sense, the PMT linearity is the degree of proportionality between an incident light signal and its resulting electrical signal output. The generic method to measure linearity involves two independent (and random) LED light sources, A and B, mounted within the same ambient light-proof enclosure; the light sources are viewed by a PMT operated at fixed high voltage (HV). The intensity of each light source is set to give approximately the same anode current. With the two anode signals referred to as I_A and I_B, respectively, a PMT produces an output of I_{A+B} when the two sources are both switched on. If the PMT is operating linearly, it is should be that $I_{A+B} = I_A + I_B$. The non-linearity manifests when the coincident sum current, I_{A+B}, ceases to be equal to the arithmetic sum, $I_A + I_B$ [20]. Measurements must start at low light levels, where there is negligible non-linearity— established by

verifying that $I_{A+B} = I_A + I_B$. A set of measurements is recorded by incrementing both I_A and I_B, more or less equally. The non-linearity can be expressed as:

$$\beta = \frac{I_{A+B} - (I_A + I_B)}{I_A + I_B} \tag{19}$$

The non-linearity will manifest at higher light levels depending on the applied voltage. The objective of the linearity measurement is to find a range of operation in which the PMT is linear, in order to reduce the systematic error in the asymmetry measurement. It is desirable to make the PMT non-linear response as small as possible.

The method described above is general, however there is no universal definition of linearity that applies to all applications. To measure the linearity (or non-linearity), it is important to choose a method that mimics the intended application. The PMT non-linearity measurements for our PVeS experiment are detailed in section 5.1.

2.5.4 PMT Gain

The photoelectrons released by the cathode are subsequently focused and accelerated towards the first dynode and then on to a series of dynodes, which are held at progressively different voltage potentials [4]. The photoelectrons strike the first dynode ejecting additional electrons. Subsequently, the released electrons will strike consecutively each dynode with more energy gained by the difference in potential, multiplying the number of electrons each time. The resulting current at the last dynode is collected by the anode and constitutes the output signal. The PMT's gain, g, is equal to the number of electrons produced at the anode, q_a, for every single photoelectron generated at the photocathode $g = q_a/e$. Some details and results of gain measurements

[4]The voltage operating range for these PMTs (R7723Q) is -700V to 2000V, with 8 dynodes with voltage ratios of 4:1:2:1:1:1:1:2:1. These PMTs have a gain of 10^3 to 10^6 respectively.

for the PREX-II/CREX detectors are given below.

In Lowe's study [28], the PMTs were calibrated at high voltage using a Poisson fitting model on the output charge distribution at very low light (single photon) conditions to extract from the fit parameters the gain values at high voltages. At the higher voltages and thus gains, the signal from a single photoelectron can be distinguished from the pedestal as well as the signal from two, three, etc. photoelectrons–as seen in Figure 36. The same fit algorithm also naturally calibrates or measures (absolutely) the "light level" during the gain measurements and this feature allows gain measurements at low HV using high light levels. For instance, for the fit shown in Figure 36, the parameter "mu" gives the mean of the Poisson which is a measure of the "light level". For this data, the light source produced 1.417 PE's on average per event or per LED pulse. This feature is also important for the simulation and analysis of the SLAC testbeam data, discussed in Chapter 4. The gain measurement plots as function of the voltage can be seen in Figures 37, 38 and 39.

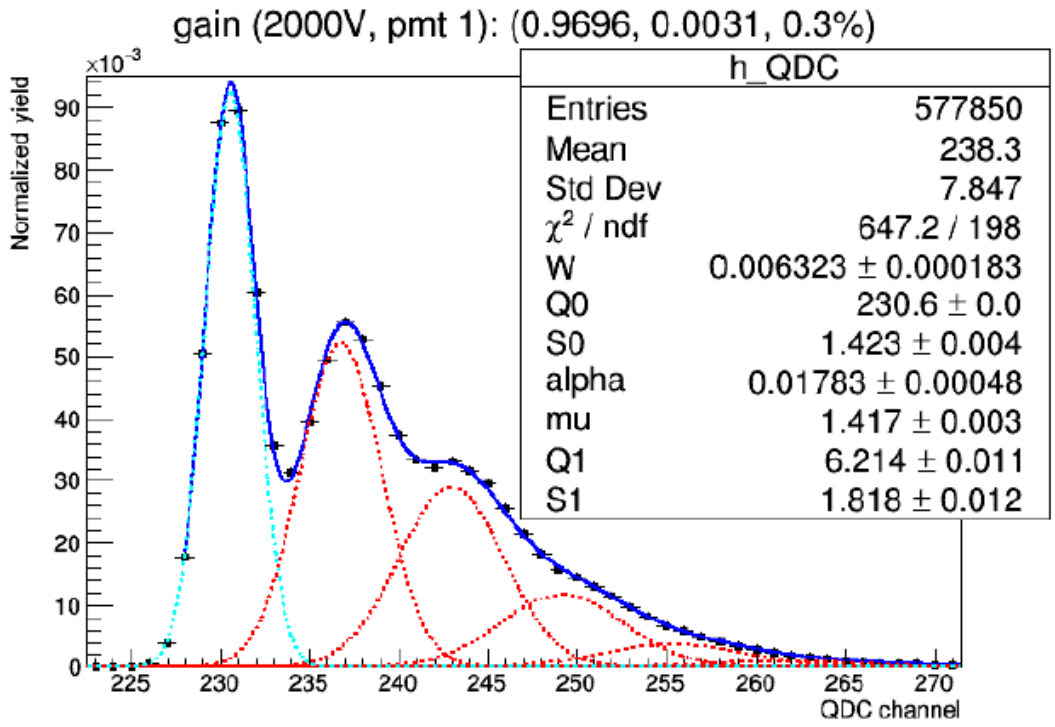

Figure 36: Charge distribution taken at the maximum voltage low light level with PMT1 measured by Brady. The cyan line is the pedestal, the red lines are PE peaks, and the blue line is the overall fit.

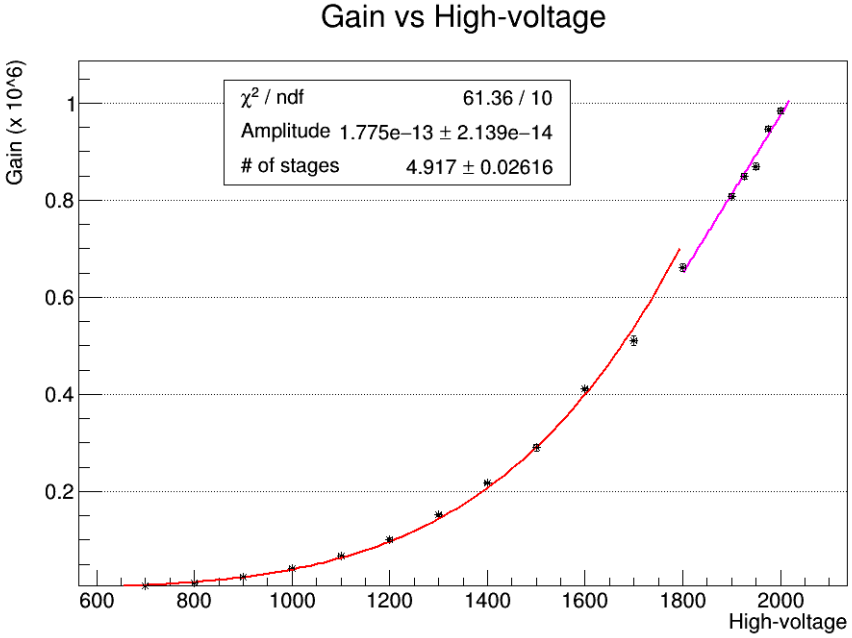

Figure 37: Measured gain of PMT1 as a function of voltage [Volts]. PMT1 is used in the PREX-II/CREX tandem detector. Measurements at high voltages and low light levels are linearly fitted by the cyan line.

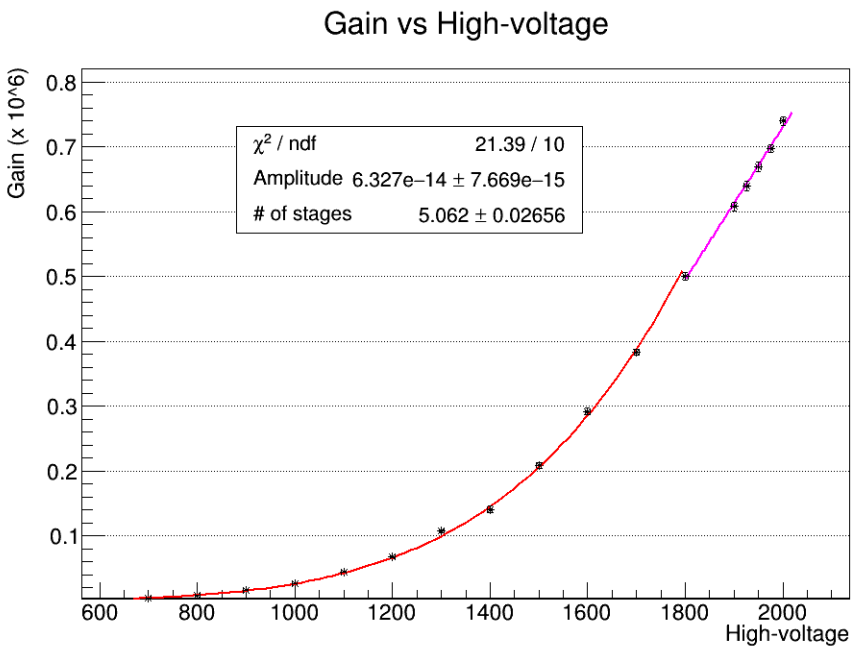

Figure 38: Measured gain of PMT2 as a function of voltage [Volts]. PMT2 is used in the PREX-II/CREX tandem detector. Measurements at high voltages and low light levels are linearly fitted by the cyan line.

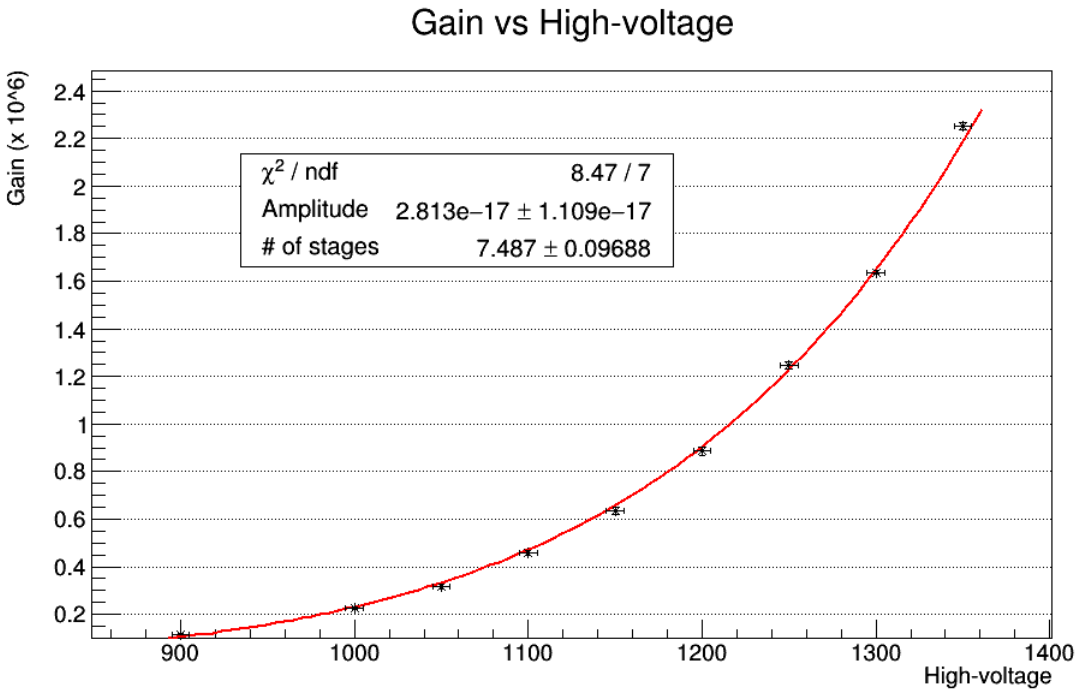

Figure 39: Measured gain of PMT5. PMT5 is used in the SLAC testbeam benchmarking 1A and 1B shower-max prototypes. These are introduced and further discussed in Chapter 4.

2.6 PMT window

We have mentioned before the importance of having a quartz window to enhance the transmission of UV light. But it is not the only way to utilize the window to increase the number of photoelectrons: we can 'recycle' the incoming light, i.e. to let it interact with the photocathode layer more than once. This can be achieved using the photocathode window as a lightguide [29, 30]. In this way, a single photon can have more than one opportunity to be absorbed and release a photoelectron into the PMT's vacuum: there is a finite probability of absorption for a photon at the first encounter with the photocathode surface. If it fails to convert, it may do so on a subsequent bounce, and so on. We borrow the formalism from reference [20] to calculate mathematically how much the quantum efficiency is enhanced by the multiple reflections for photons trapped inside the quartz window. The situation is depicted in Figure 40.

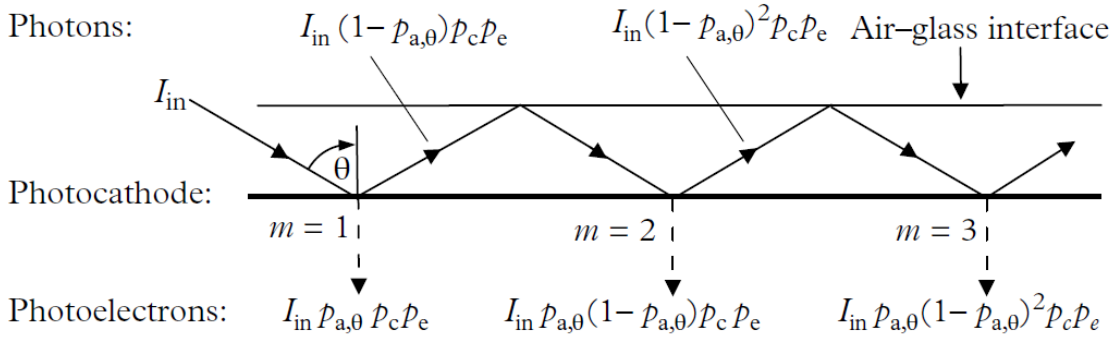

Figure 40: The passage of trapped light in a waveguide formed by the photocathode and the external window surface of a PMT. Figure from reference [20]

The photoelectric effect can be described as a three step process: the first, the absorption of an incident photon with a probability $p_{a,\theta}$ in the photocathode; the second, the promotion of an electron to the conduction band with probability p_c; and third, the escape of the electron into the vacuum with probability p_e.

For a photon with normal incidence, the QE, η_0, may be written as

$$\eta_0 = p_{a,0} p_c p_e, \tag{20}$$

where η_0 is, in general, a parameter given by manufacturers. For non-normal incident light, the QE, η_θ depends on the angle of incidence and would have to be measured empirically to know this dependence.

At the first point of reflection, $m = 1$ in Figure 40, a fraction on the input light, $I_{in} p_{a,\theta} p_c p_e$ is converted to photoelectrons, and the light remaining, $I_{in}(1 - p_{a,\theta}) p_c p_e$, proceeds to the next reflection point, $m = 2$ in the figure. A further $I_{in} p_{a,\theta}(1-p_{a,\theta}) p_c p_e$ photoelectrons are produced, with $I_{in} p_{a,\theta}(1 - p_{a,\theta})^2 p_c p_e$ remaining and so on. After a number m of reflections, the number of photoelectrons produced is:

$$\sum_1^m I_m = I_{in} p_{a,\theta} p_c p_e [1+(1-p_{a,\theta})+(1-p_{a,\theta})^2+...+(1-p_{a,\theta})^m-1] = I_{in} p_c p_e [1-(1-p_{a,\theta})^m]. \tag{21}$$

For a large number of reflections (m), the expression in square brackets tends to unity which leads to,

$$\eta_{\Sigma,\theta} \equiv \sum_{m=1}^{\infty} \frac{I_m}{I_{in}} = p_c p_e = \eta_0 / p_{a,0}. \tag{22}$$

The sum on the left represents the QE, $\eta_{\Sigma,\theta}$ for those photons that bounce inside the quartz window. According to Equation 22, the quantum efficiency, η_0, is enhanced by a factor $1/p_{a,0}$ for all wavelengths and for all kinds of photocathodes. An absorption of $p_{a,0} = 55\%$ for a bialkali cathode boosts the QE ~ 1.8 times for these photons that bounce inside the PMT window. Once an incident photon bounces inside the PMT, its probability of being absorbed and releasing a photoelectron almost doubles. And the photons with a wavelength for which $p_{a,0}$ is smaller are favored even more.

2.7 Additional reflections from inside PMT

A fraction of transmitted light interacts directly with the aluminized and photosensitive surfaces inside the PMT producing photoelectrons.

Most "transmission" PMT designs include a reflective internal support flange, in the form of a disc with a central hole, located in front of the first dynode. Some transmitted light is reflected by this flange and intercepted by the photocathode. A fraction of transmitted light interacts directly with the aluminized and photosensitive sidewall producing photoelectrons (see Figure 41). The probability of reflection on the first dynode is small but non-zero and photoelectrons can be created directly at the fist dynode[20]. Note however that photoelectrons ejected from the first dynode will not be fully amplified as they traverse one fewer stage of amplification.

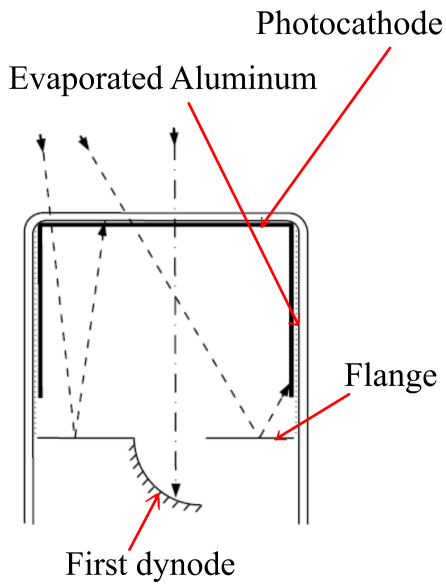

Figure 41: Illustration of how light transmitted through the photocathode is reflected on the photosensitive surfaces inside the PMT. Some photons are reflected on the PMT's aluminized wall or the internal support metallic flange. Some photons can release photoelectrons directly from the first dynode.

3 Geant4 Optical Simulations and Prototype Development

This chapter will discuss how Geant4 (GEometry ANd Tracking) can be used to simulate the response of a thin quartz detector. Geant4 is an ideal framework for modeling optical properties and processes related to thin quartz detectors and their associated lightguides. The simulation constitutes a powerful tool to improve or optimize the thin quartz detector designs and then to develop new, more complex detector geometries for future experiments–such as the Shower-max sampling calorimeter detector-ring for MOLLER.

3.1 Geant4

Geant4 is a popular $C++$ based software toolkit developed by CERN for the Monte Carlo simulation of the transport of particles through matter and the interactions they undergo. Geant4 covers many physics processes for electromagnetic and hadronic physics over a large energy range from eV to TeV. For these simulations, several aspects are considered:

- The geometry (G4Box, G4Trap, etc.)
- Materials and their properties (G4Element, G4Material, G4MaterialPropertyTable, etc.)
- Physics processes caused by the interactions (G4Cerenkov)
- The traversing particles and their properties (G4OpticalPhoton, G4Electron, etc.)
- Particle tracking through matter (G4Track, G4Step)

- Sensitive detector components and their user defined actions (G4SensitiveDetector)
- Access to simulation data
- Visualization

"In Geant4, a full simulation run (G4Run) has several parts. A G4Run is made of one or more events (G4Event), which combine one or more primary particles (G4ParticleGun is responsible of starting single events in a run), which are simulated one after the other. Each primary particle is created in the same position and with the properties (energy, momentum, and type) that have been specified by the user in the macro file. The primary particles and potential secondary particles from interactions are tracked through space on their way through the simulated volumes– e.g., quartz tile, PMT window, photocathode and lightguide (if used). The tracking of a particle stops if it leaves the mother volume or if it is stopped (physically) by either the total loss of its kinetic energy, its decay into other particle or its termination by a user-defined action. The track (G4Track) of each particle is divided into G4Steps. In general, one G4Step is the distance between two successive, discrete point interactions. An exception from this rule is that traversing the boundary between two different geometric volumes always defines the start/end point of a G4Step" [31, 32].

Geant4 contains extensive and flexible optical physics capabilities. This permits the simulation to commence with the propagation of a charged particle and complete with the detection of optical photons (G4OpticalPhoton) on photon-sensitive areas (G4SensitiveDetector), all within the same event loop. The optical photon transport functionality of the Geant4 package provides the possibility to set the optical properties for both bulk materials and surfaces and makes for a realistic simulation. Geant4's unique capability of starting the simulation with the propagation of a charged particle and completing it with the detection of the optical photons by

photo-sensitive areas, all within the same event loop, makes it an effective and comprehensive tool for realistically modeling the optics of Cerenkov detectors and their associated lightguides.

Geant4 has a special class of particles, optical photons. A photon is defined as optical when its wavelength is much greater than the typical atomic spacing. Optical photons are the only particles that can be reflected or refracted at optical boundaries, and are the only ones that can be created in an optical process.

In Geant4, optical photons are a class of particles detached from the higher energy gamma rays. This implementation allows processes arising from the wavelike property of electromagnetic radiation to be associated with optical photons. In Geant4, optical photons are produced in three physical processes: Cerenkov, scintillation and transition radiation.

Geant4's catalog of processes at optical wavelengths includes refraction and reflection at medium boundaries, bulk absorption and Rayleigh scattering, scintillation, Cerenkov radiation, wavelength shifting and total internal reflection.

The optical properties of the medium are stored as entries in a properties table associated to the material in question [33]. Each material needs at least a refractive index spectrum or an attenuation length spectrum as user input in the form of an array [34]. The precise value of the reflectivity, refractive index and attenuation length are linearly interpolated between two given values in the optical property arrays.

3.2 Cerenkov Process in Geant4

The flux, spectrum, polarization and emission of the Cerenkov radiation follows a well known formula in Geant4. As an example, in Figure 42, we have the spectrum of photons that arrive at the PMT window surface for the Small Angle Monitor (SAM)

detector, and how it compares to the formula in Equation 14, assuming a constant index of refraction. We can see how the simulated spectrum goes as $1/\lambda^2$.

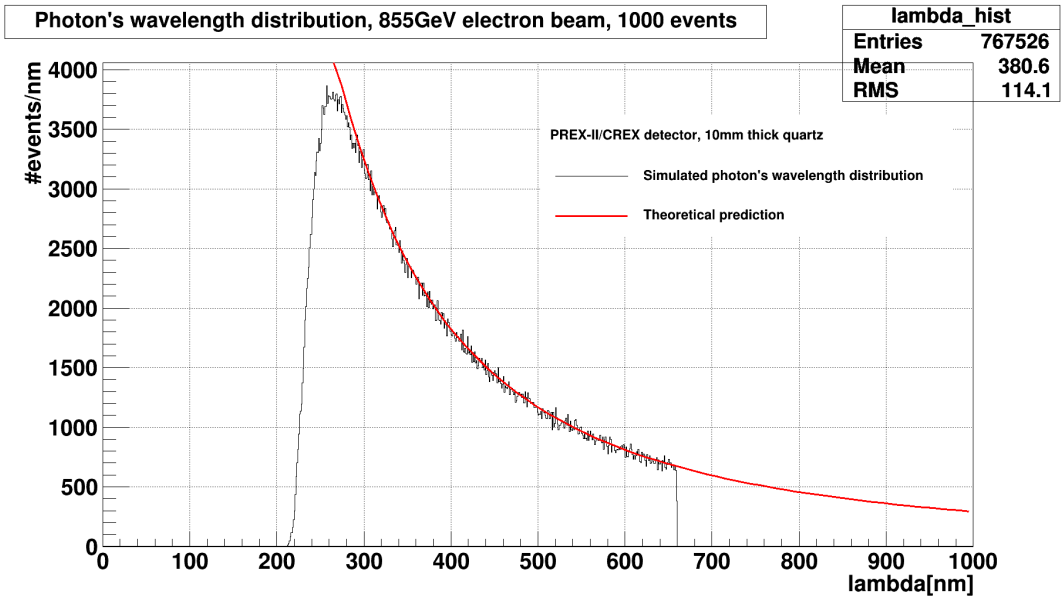

Figure 42: Comparison between the simulated photon spectrum that reaches the PMT in the PREX-II/CREX detector, neglecting the PMT's quantum efficiency (set to 1) vs the approximation in theoretical formula (Equation 14).

In Geant4, the number of Cerenkov photons per track length is calculated with the formula [31]

$$\frac{dN}{dx} = 370z^2 \left[E_{max} - E_{min} - \frac{1}{\beta^2} \int_{E_{min}}^{E_{max}} \frac{dE}{n^2(E)} \right], \tag{23}$$

where the energy range, $\{E_{min;E_{max}}\}$, is given by the array of energies given by the user and the range should cover the PMT's QE. The refraction index, $n(E)$, is fed in as an input. The number of photons produced is calculated from a Poisson distribution with a mean of $< n >= StepLength \times dN/dx$.

The energy distribution of the photon is then sampled from the density function,

$$f(E) = \left(1 - \frac{1}{n^2(E)\beta^2} \right). \tag{24}$$

The time and position of Cerenkov photons are calculated from quantities known at the beginning of the charged particle step, which is assumed to be rectilinear, even if there is a magnetic field present. By default, the tracking of a charged particle (like an electron), is postponed in Geant4 at the point of time when it creates new optical photons, because the number of Cerenkov photons generated in the length of the typical step is often very large. After the tracking of the optical photons is completed, the processing of the charged particle will continue.

The user can limit the step size by defining a maximum number of Cerenkov photons created during the step to optimize CPU use, but the actual number will necessarily be different for each step due to the Poissonian nature of the production. The smaller the maximum value, the shorter (and hence the more) steps are taken by the parent charged track, but the total photons generated by the track is unchanged.

The absorption of optical photons is a simple process which only kills the optical photons. The process requires the user to include empirical data of the absorption length in the material properties table.

3.3 Boundary Processes: Reflection and Refraction of Photons in Geant4

Reflection and refraction of optical photons can occur when a track cross a boundary between two volumes. Geant4 uses the normal vector that describes the boundary between the two volumes to calculate the reflection or refraction angles. These boundary processes are discrete and they are called at the end of each particle step. The code must first verify that the track is already in a boundary before getting into action.

When a photon arrives at the boundary between two media, its behavior depends on the nature of the two materials that join at the boundary. The boundary types in

Geant4 are:

- Dielectric-dielectric: The photons can be transmitted (refracted) or reflected (internal reflection). In the case where the photons can only by reflected, total internal reflection takes place. The PREX-II/CREX detectors use the TIR to drive the photons toward the PMT.

- Dielectric-metal: The photons can be absorbed by the metal or reflected back into the dielectric. If the photon is absorbed and the metal surface is defined as sensitive, the photon is detected according to the photoelectron efficiency (R7723Q's QE) of the metal. The PMT's photocathode surface is a detecting surface with dielectric-metal boundary; the dielectric is the PMT's quartz window and the metal is the photocathode. The SAM lightguides have a dielectric (air) to metal (aluminum) boundary as well, but they only reflect the photons according to their reflectivity since they are not defined as sensitive surfaces.

- Dielectric-black material: A black material is a medium which has no optical properties. In this case all photons are absorbed.

3.4 Optical Surfaces

The Geant4 optical surfaces can be used to simulate surfaces that are not perfectly smooth between two dielectrics. With Geant4 optical surfaces, several surface types and surface finishes can be specified. The optical boundary process relies heavily on the concept of surfaces. The information relevant to the surface is split into two classes. One class is the material category that keeps the information about the physical properties of the material itself, and the second class is the geometry category that holds pointers to the relevant physical and logical volumes (G4LogicalVolume) involved in the boundary process.

Objects of the second class can be retrieved by either specifying the logical volume entirely surrounded by the surface or the pair of physical volumes (G4PhysicalVolume) touching at the surface. The former is called a skin surface (G4LogicalSkinSurface), while the later is called a border surface (G4LogicalBorderSurface).

The first type of surface is useful in situations where the volume is coated with a reflector and placed into many different mother volumes. A limitation is that the skin surface can only have one and the same optical property table for all the enclosed volume sides. The border surface is made of the sides of an interface between a pair of physical volumes. So the user can choose different optical properties for photons arriving to different sides of the same interface.

At the boundary between two dielectrics, the optical photons can be totally internal reflected, refracted or partially reflected, depending on the photons wavelength, angle of incidence, and the refractive indices on both sides of the boundary. The optical photons can be absorbed by the metal or reflected back into the dielectric.

3.5 Optical Models

In order to include surface irregularities (roughness), the Geant4 optical models can be used. Geant4 has two optical models to simulate the transport of optical photons: GLISUR and UNIFIED. In the GLISUR model, the user modulates the quartz surface roughness using the GLISUR's ground polish parameter. In this model the surface is made up of micro-facets with normal vectors following a given distribution. The polish parameter modulates the normal vector distribution; it is 1 for a perfectly smooth surface where reflections are governed by Snell's law, and 0 for the maximum roughness, where the photons are reflected according with a Lambertian distribution (diffuse reflection from a surface with matte appearance)[35]. In the GLISUR model, a random point on a sphere of radius $(1 - \text{polishparameter})$ is generated and the

corresponding vector is added to the normal. The UNIFIED model allows the user to control the radiant intensity of the mirror surfaces. In the UNIFIED model, the angle between the micro facets normal an the average surface normal is assumed to follow a Gaussian distribution. While the GLISUR optical model is used for the quartz tiles, the UNIFIED model is used for the lightguides.

3.6 QSIM Framework

The quartz simulation, QSIM, is an application of Geant4 dedicated to the simulation of thin quartz Cerenkov detectors. We incorporated the PREX-II/CREX, SAM, and Shower-max detector geometries inside QSIM using the standard geometric solids build in Geant4. It uses the Geant4 optical surface models to simulate the transport of Cerenkov photons and their detection to estimate the detector's PE yield and resolution. The optical properties, like quartz reflectivity and absorption length, photocathode QE and reflectivity, and lightguide reflectivity are inputs to QSIM in the form of tables as function of photon energy.

The geometry and optical properties of the detector elements considered in the simulation are specified inside the code by modifying the QSIM source code, specifically the `qsimDetectorConstruction.cc` file. Figures 43a and 43b show the QSIM geometric models of the PREX-I detector and the PREX-II/CREX detector prototype. Notice that only the objects with relevant optical surfaces and the photocathode are included in the model. For a more how-to discussion of QSIM, see appendix 6

Figure 44 shows the geometric model of the SAM detector, which is characterized by a long lightguide designed to funnel the photons from the quartz piece in one extreme to the other, where the PMT is located. Only one photon track is displayed, it bounces 4 times on the lightguide before it does reach the PMT.

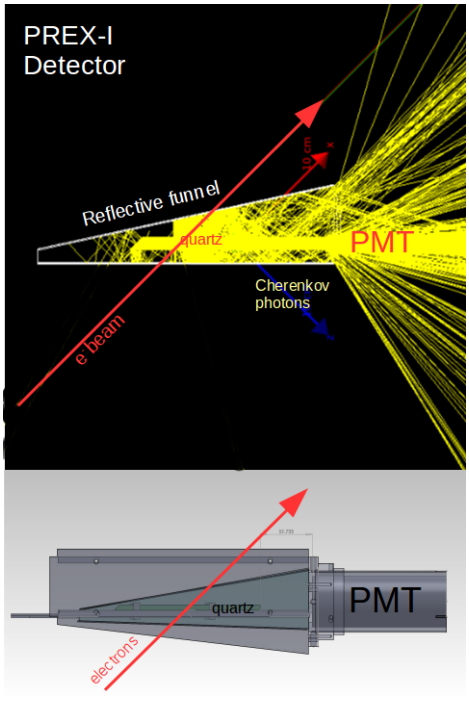

(a) PREX-I simulation visualization and CAD drawing.

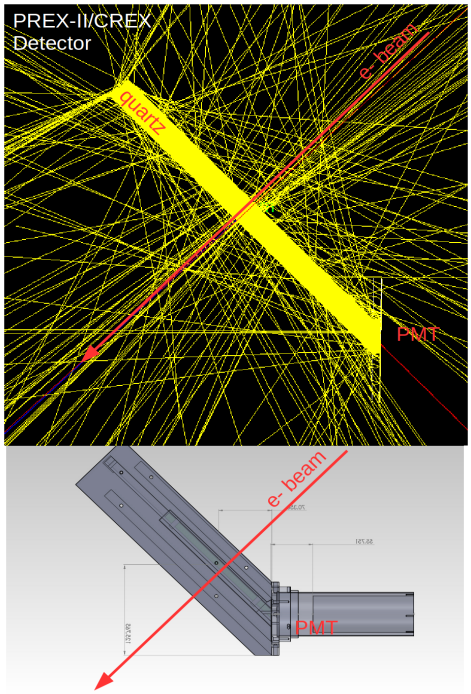

(b) PREX-II/CREX simulation visualization and CAD drawing

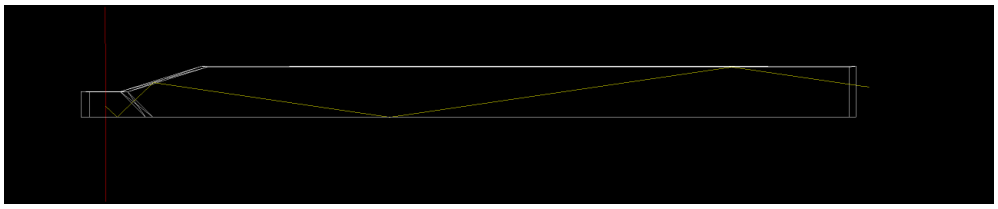

Figure 44: QSIM visualization of the SAM detector geometry with the track of single optical (Cerenkov) photon (yellow) created by an electron (red) inside the quartz.

It is important to describe what happens to the photons when they arrive at the photocathode: For our simulations (Figures 45 and 46 display a one event visualization), from the total number of photons generated in one given event that make their way to the photocathode surface, $\sim$ 12.5% are reflected, $\sim$ 25% are absorbed and make a photoelectron, and the rest are terminated ($\sim$ 62.5%). On the other hand, in reality, from the 62.5% of the photons that are neither absorbed or reflected in the simulation, $\sim$ 37.5% of the photons would be absorbed, however would not produce a photoelectron. And $\sim$ 25% would be transmitted (refracted) through the quartz

glass and the photocathode coating. 17.5% of the photons would be reflected back by different reflecting surfaces located behind the photocathode, 4.38% of them will make a photoelectron. This is summarized in Table 2.

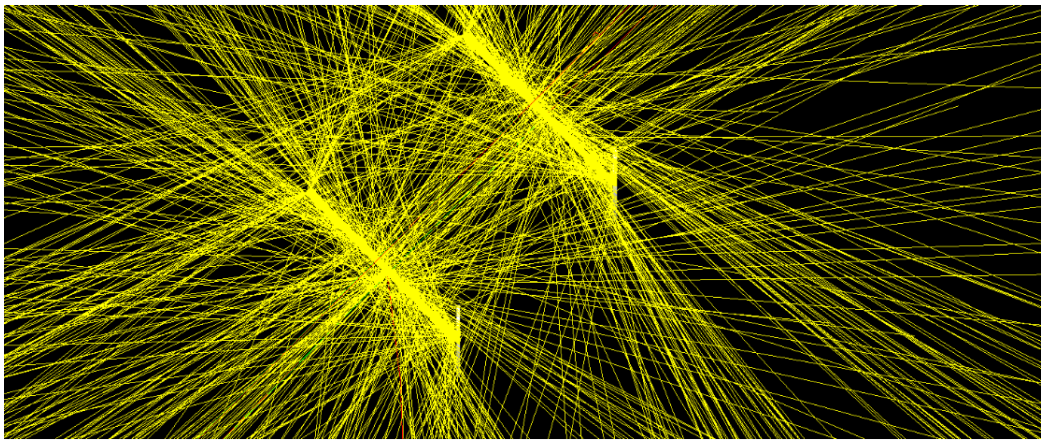

Figure 45: PREX-II/CREX tandem detector visualization of one simulated event in QSIM. The light rays (in yellow) can be seen being internally reflected with some escaping the quartz due to the (unwrapped) quartz surface roughness.

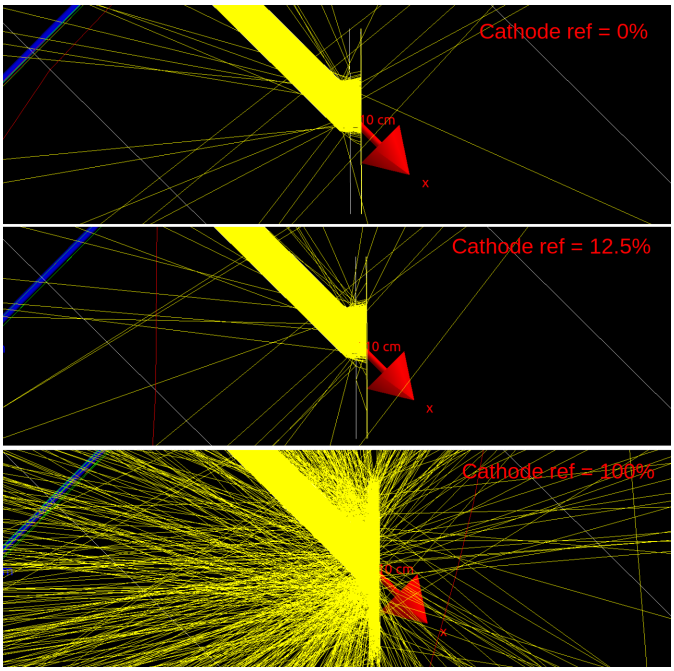

Figure 46: Close-up view on the quartz bevel and the PMT's window and photocathode. Each picture corresponds to the simulation of one-event using three different values of the cathode reflectivity. Notice the effect of a higher reflectively of the cathode: Some of the reflected photons would bounce back inside the PMT window and get another chance to be absorbed by the photocathode.

Simulation		Reality	
Reflected	12.5%	Reflected	12.5%
Absorbed	25.0%	Absorbed	25.0%
Termination	62.5%	Absorbed without making a a PE	37.5%
		Transmitted	25.0% (17.5% reflected back)

Table 2: This table summarize the optical properties of the photocathode as modeled in the simulation and what happen in reality. In the simulation, there is not transmission.

The optical Monte Carlo simulations can be used to design an optimize the Cerenkov photon collection at the photocathode. In order to get the best results the simulation should be compared with real data. Such data was obtained in controlled beam tests and was used to tune the simulation parameters. This simulation benchmarking is presented in the following chapter.

4 Beam Tests and Simulation Benchmarking

4.1 New Luminosity Monitor: SAMs

The predecessors of the SAMs, the Luminosity Monitors (LUMIs) consists of eight Cerenkov detectors concentrically placed around the beam line, in four opposing pairs, at $\sim$ 7.5 m downstream of the target center. They are each mounted inside individual vacuum tubes that, when inserted into the beam pipe, reach to within 5.5 cm of the beamline center. The original LUMI detectors were designed to monitor beam-target luminosity (target melting or boiling) as well as parity-quality beam parameters–helicity correlated beam parameters (HCBPs): position, angle, and energy on target. However, the original LUMIs, first installed in 2002 and then refurbished in 2008, did not work (well) due to a non-optimized lightguide geometry and too long (radially) of a quartz radiator–causing too large a variation in rate interception. In 2015, the LUMI was redesigned and renamed the Small Angle Monitor (SAM) because it monitors the flux of primary and secondary beam particles emerging from the target at small angles ($<$ 1 deg). At these small scattering angles, and thus negligible momentum transfers, the parity violating asymmetry (A_{PV}) is effectively zero within measurement capability. Combining this feature with the extremely high flux rates at the SAMs (GHz - THz), makes these highly sensitive null-asymmetry monitors as well as monitors of HCBPs and target density changes. A CAD render of one complete SAM assembly is shown in Figure 47 and a simulated event visualization is given in Figure 48.

Each SAM detector is made up of a small quartz radiator ($\sim$ 2 cm long), features an optimized air-core aluminum lightguide geometry with MIRO27 specular reflecting internal walls ($\sim$ 35 cm long), and uses a 2-inch Hamamatsu R375 PMT with either a conventional high-gain base (voltage divider circuit) or a unity gain base (unity gain

is needed when operating at the very high rates for PREX-II/CREX).

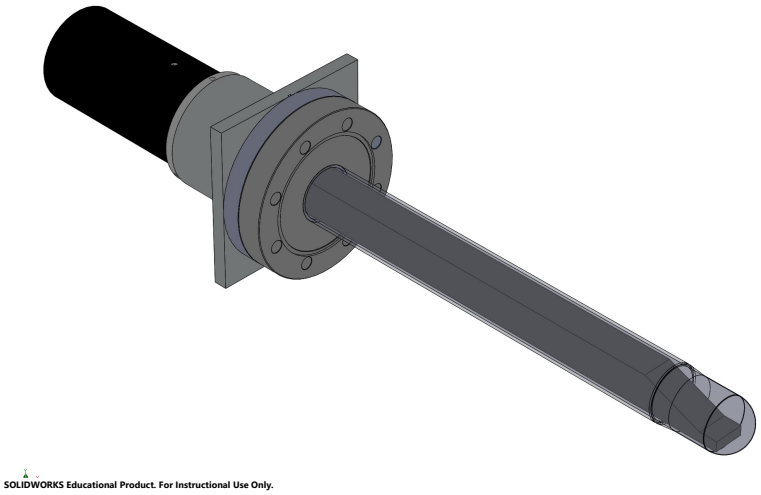

Figure 47: SAM detector assembly where the lightguide and quartz are shown inside the vacuum insert tube. Note the end-cap of the casing is spherical (0.012" thick) instead of the previously used flat (0.065" thick) end-cap.

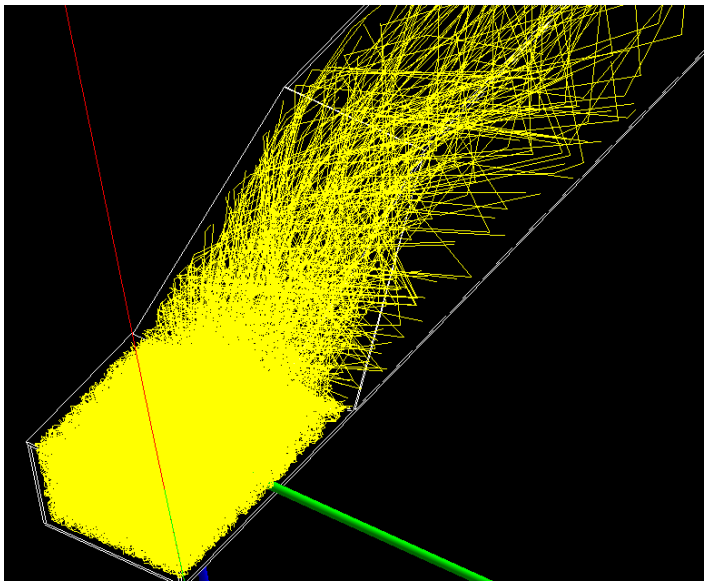

Figure 48: Picture shows the SAM detector quartz being hit by an electron (red) from above, many Cerenkov photons (yellow) are created inside the quartz. Notice how they are internally reflected inside the quartz and how the light bounces inside the lightguide. The lightguide geometry was optimized to reduce the number of bounces that the photons undergo before reaching the PMT at the other side of the lightguide.

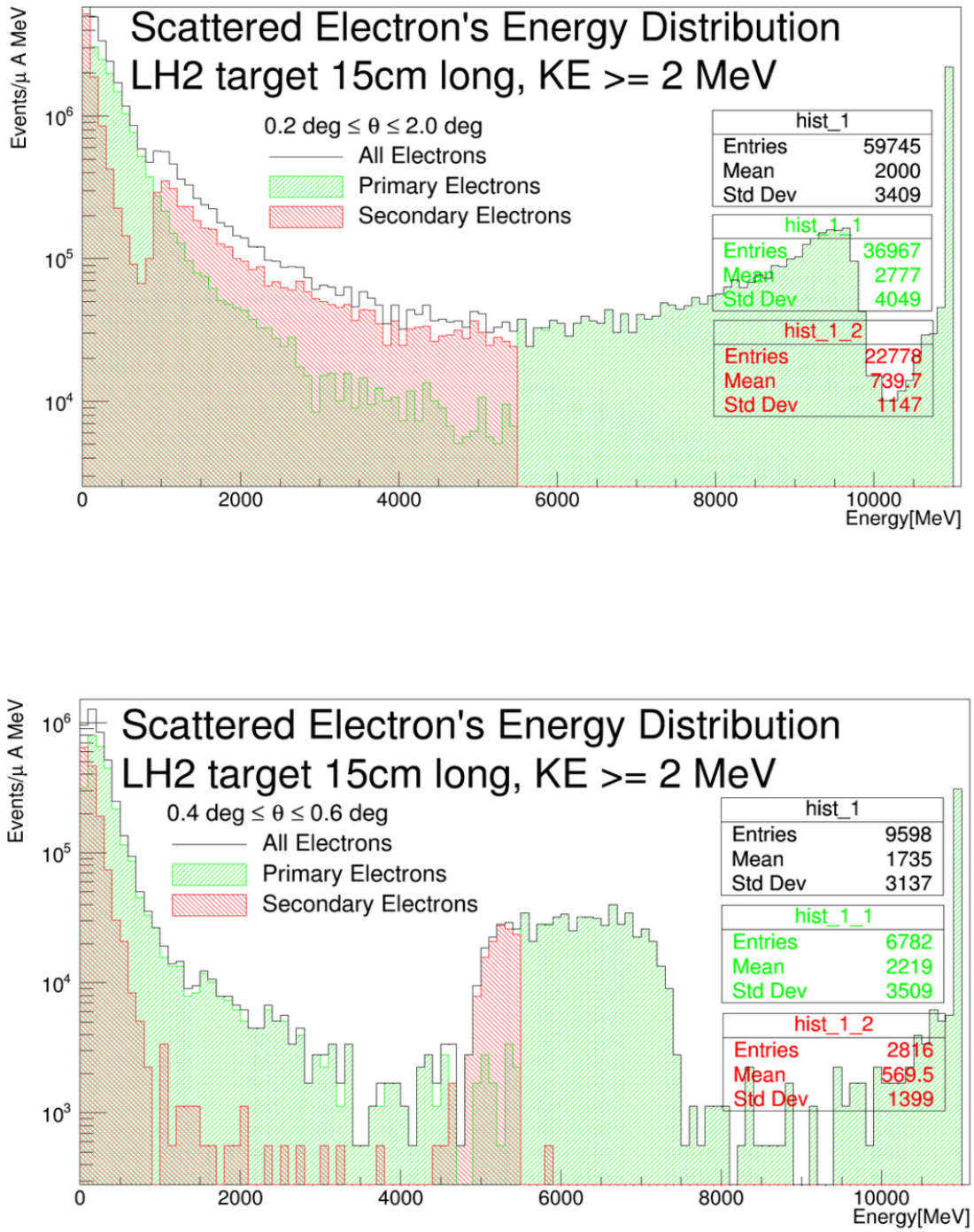

Figure 49: Simulation of scattered electron flux and energy per μA beam current emerging from a 15 cm long LH_2 target with azimuthal angles between 0.2 deg to 2.0 deg (top plot) and 0.4 deg to 0.6 deg (bottom plot). Incident beam energy is 11 GeV. The scattered electron flux comes from Moller (e-e) and Mott (e-p) interactions in the target.

The LUMIs, the previous luminosity detectors, were introduced first in the HAPPEX-II experiment, which used a 15 cm cryogenic liquid hydrogen gas target (see Figure 49 to see the electron flux generated from such target). The signal width was sensitive to density variations in the target, which could boil due the heat produced by the high current beam. Since the luminosity is proportional to the target density and the beam current, the LUMIs were considered luminosity detectors. The Q_{weak} experiment in Hall C at JLab used LUMIs as well, including some improvements to them: the addition of a 1.0 cm thick lead pre-radiator, new redesigned lightguide, a thicker, shorter quartz radiator and the use of a unity gain PMT. The new Hall A SAM design is based on the improved Q_{weak} LUMI design.

The quartz piece is placed close to the beam, and detects electron flux at very small angles (~ 0.5 deg). Because the rates of scattered electrons hitting the quartz are high at these small angles, the integrated signal would have a small statistical width (due to very high rate detection) and can be used to detect small helicity-correlated beam fluctuations. These studies were used to determine the optimal running conditions of the beam and estimate the contribution of target density fluctuations to the statistical error of the experiment. This becomes very important if the high beam currents are used to get more statistics.

The raw LUMI ADC values from each helicity window are used to calculate the asymmetry (equation 1). The statistical widths of the asymmetry distributions are analyzed. If no broadening of the asymmetry widths are observed, the widths should follow a Guassian distribution with $\sigma_n = \sqrt{n}$. The deviation of the widths from counting statistics in all LUMIs indicates the presence of target density fluctuations or helicty-correlated fluctuations.

However, monitoring the radiation produced by a high density target, like the one used in Q_{weak} or PREX, is more difficult. For this reason, the LUMI detectors

required an upgrade. Only a fraction of the initial light flux traverses the lightguide, reaching the PMT and their collection should be optimized. Most of the Cerenkov photons produced inside the quartz, leave it at a near perpendicular angle with respect to the quartz's bevel surface. With this information, Kevin Rhine [36] developed a Mathematica script in which he did a geometrical study of the long lightguide. He optimized the angle of the so-called "one-bounce" (funnel) mirror part of the lightguide. In this way, most of the photons would have a minimum number of reflections before being directed to the PMT window located at the opposite end of the $\sim$ 35 cm long lightguide (see Figure 50).

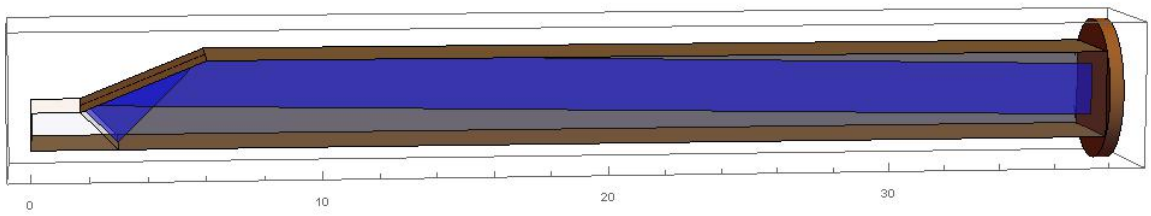

Figure 50: Kevin Rhine's optimized geometry for the SAM lightguide. The lightguide is made from a single metal mirrored sheet (MIRO27), machine cut and hand folded. The quartz radiator (white trapezoid) is contained inside the lightguide at one end. From the quartz end, the rectangular lightguide extends all the way to the PMT window. The most crucial part of the design is the angle of the "one-bounce" mirror just above the quartz; this angle was chosen to direct the most light to the PMT with the fewest reflections (the blue shadow in the figure shows the path of the one-bounce photons).

The Figure 51 shows QSIM's distribution of α, the angle between the Cerenkov photon momentum and the quartz wedge surface in the x-z plane (see the diagram in Figure 51b). The photons are reflected from the mirror's upper inclined surface. The distribution peaks sharply at $\sim$ 42 deg and as intended with the geometrical study, these photons are more likely to suffer only one or two bounces before reaching the PMT window. In contrast, the photons of the left part of the spectrum, reflected at smaller α angles are more likely to suffer multiple bounces on the mirrors surfaces

with a high probability to be absorbed. The upgraded monitor system (Figures 51a and 51c), which consist of several Small Angle Monitors (SAMs), is installed in Hall A at JLab.

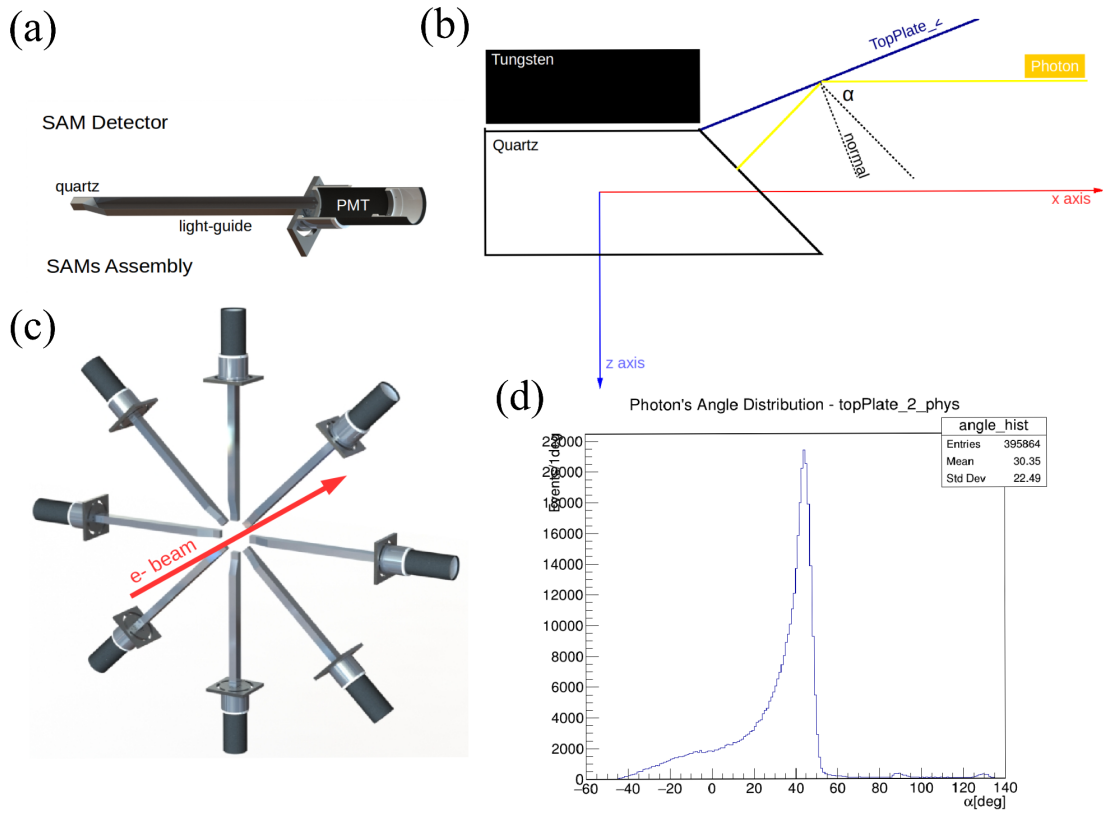

Figure 51: (a) CAD cross section of a single SAM detector. (b) Schematic side-view of SAM quartz and one-bounce mirror angle α. (c) CAD depiction of the array of eight SAM detectors around the beam line. The long lightguides allows the quartz radiator to be close to the beamline while keeping the PMT at a safer distance. (d) Distribution of the number of photons reaching the PMT as a function of α. This study gives a clear optimal angle for the one-bounce mirror.

A tungsten radiator could also be placed in front (or upstream) of the quartz to increase its signal size (albeit at a cost of reduced resolution). The reason for this idea is to ensure that the light reaching the PMT is dominated by Cerenkov light from the quartz and not scintillation light from scattered electrons traversing the "air" in the lightguide's cavity. There is also Cerenkov light produced by charged

particles traversing air, but this light is along the direction of the charged particle (since index of refraction is near 1) and would need too many reflections to make it to the PMT. The scintillation light on the other hand is generated isotropically and can go directly to the PMT. Thus, the idea of a pre-radiator was considered for the SAMs. The enhancement in the signal from the tungsten pre-radiator comes from electromagnetic showering in the tungsten which creates many more charged particles (electrons and positrons) that relativistically traverse the quartz, making more Cerenkov photons per incident scattered electron (or particle) from the target; these scattered particles produce gamma rays (via Bremsstrahlung) when traversing the tungsten. The gamma rays in turn produce electron-positron pairs (via pair-production), thus effectively creating a shower of secondary electrons (and positrons) over the quartz (see Figure 52).

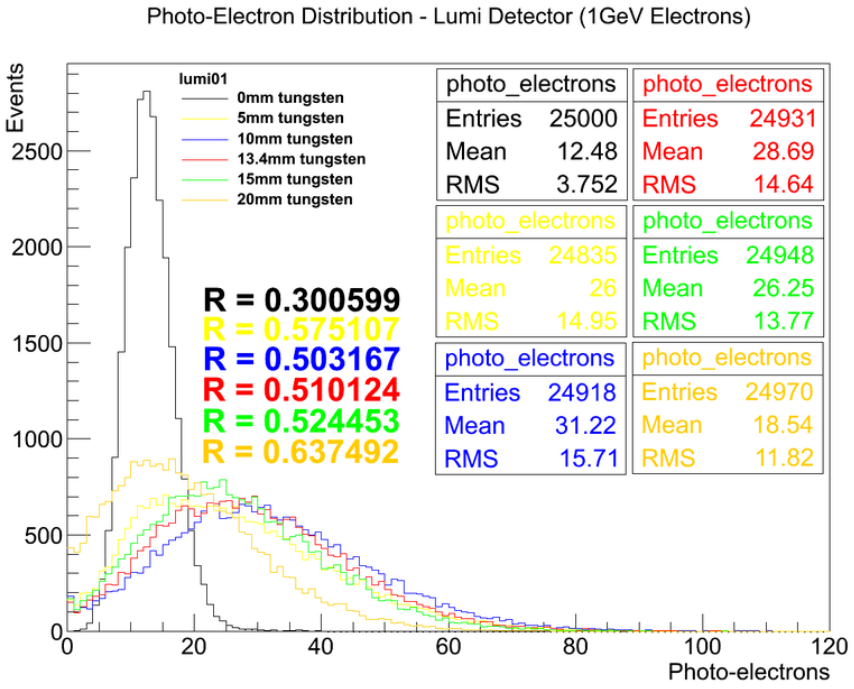

Figure 52: Simulated photoelectron distribution for LUMI detector using different tungsten radiator thicknesses. The use of a tungsten radiation would increase the resolution, $R = RMS/Mean$. According with the simulations, the radiator optimal thickness is 10 mm.

In the PREX-II experiment, though, the radiation safety requirements prohibited the use of a tungsten pre-radiator, and it was necessary to redesign the vacuum insertion tubes, reduce the overall length of the SAM lightguide and reduce the thickness and size of the quartz radiator. Recall that the vacuum insertion tubes allow the SAM detector lightguides to be inserted deep into the beamline and close to the beam (see Figure 47 for a CAD of the new insertion tube with spherical end-cap–which greatly reduces unwanted radiation production in the Hall). The PREX-II SAMs required a modification of the lightguide design, shortening it from 15.57 inches to 14.192 inches, and the angle of the one-bounce mirror was increased from 16.6 deg to a more optimized 22.5 deg due to the decreased thickness of the quartz (6 mm thick instead of 13 mm).

4.1.1 SAMs Parasite Test in Hall A

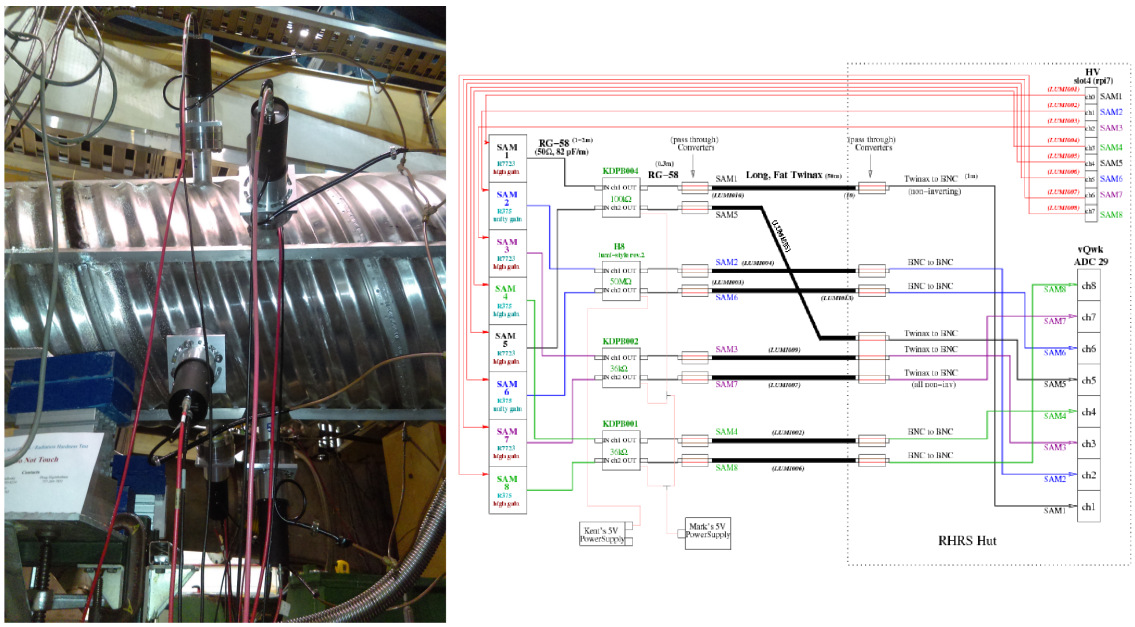

Figure 53: Left: SAMs installed in Hall A beamline, JLab. Note there is a 15 cm separation along the beamline between two sets of four SAMs. This ensures no interferences between the vacuum insertion tubes. Right: Wiring configuration for the SAMs.

Uncontrolled helicity correlated fluctuations in beam current, energy and position and angle on target can contribute large sources of systematic error in the the "main" integrating detector A_{PV} measurement. The SAMs play an important role in diagnosing and/or monitoring these correlations during the experiment. This is due to the SAMs extreme high rate detection and thus very narrow asymmetry widths–which are extremely sensitive to any slight changes in the beam or target performance.

The initial SAMs were first installed in December 2015, just before the completion of the JLab 12 GeV beam-energy upgrade. The goal was to use an upcoming experiment (called DVCS) to parasitically "commission" the SAMs (as well as other beam monitors for PREX-II/CREX). The DVCS experiment used a 15 cm long liquid hydrogen target cell and various beam energies between $\sim$ 2 and 8 GeV. Simulation predictions for the expected SAM rates were validated from asymmetry widths within 30% using the PE yields from testbeam data (discussed in the next results section) combined with PMT gain estimates. This was a nice validation of the operational design of the SAMs. Another purpose of the parasitic tests was to verify the parity quality of the beam following the 12 GeV energy upgrade. To do this, new Beam Current Monitors (BCMs) and Beam Position Monitors (BPMs) were also commissioned during this time. These monitors provided measurements of helicity correlated positions and currents for the various beam energies. The resolutions of the BCMs and BPMs was also cross-checked using the SAM data.

4.2 2015 and 2016 MAMI Test Beam Results

A number of tests were conducted in two different electron beam facilities: the Mainz Microtron (MAMI) and the SLAC linear accelerator. These tests were executed in order to examine the performance of the new PREX-II/CREX tandem detector, SAMs, and MOLLER Shower-max detector. We collected valuable data that is used

to benchmark the Monte Carlo simulation.

During May and June of 2015 and 2016, the PREX-II/CREX main detector prototype and SAMs were tested using the Mainz's Microtron (MAMI) 855 MeV continuous wave electron beam. This beam provided single electrons at requested rates between $10^2 - 10^4$ Hz. The tests were carried out at the X-1 test-stand (experimental area) of the facility. The test-stand (see Figure 54) has a rotable platform on which the detectors were mounted and then exposed to the electron beam. The beam emerged from a thin vacuum pipe window approximately one meter upstream of the platform pivot.

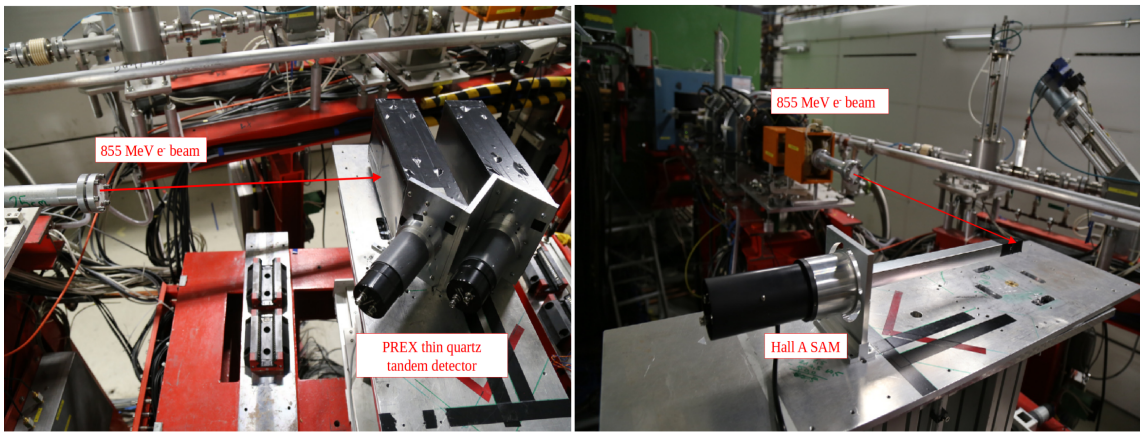

Figure 54: Experimental area. Left: PREX-II/CREX tandem detector placed on the rotating platform. Right: SAM detector. Red arrows show the approximate electron beam trajectory.

4.2.1 SAM Prototype Tests

The SAM detector was tested using two lightguides made with different reflective surfaces: MIRO-27 and UVS (Figures 55 and 56, respectively). The reflectivity of the lightguides as a function of the photon wavelength and angle of incidence (Figure 29) was approximated with a simple step function in QSIM. The fairly complicated reflectivity distributions, as a function of wavelength, were approximated using two

constant levels with a discontinuous step at the chosen wavelength. The inset plots in Figures 55 and 56 show the chosen levels and reflectivity values used in QSIM.

Although the lightguide reflectivity depends on both the photon incident angle and wavelength, QSIM only takes into account the second. However using an angle that averages over all the angles gives a close approximation and greatly simplifies the QSIM coding for this feature; also allowing it to run faster. A somewhat surprising find here is that the MIRO-27 sheet gave better results (more PEs) than the UVS for the SAM detector. This was surprising because the UVS has better UV reflectivity. The relevant simulation parameters for the SAM simulations in QSIM are given in Table 3. Figure 57 shows a visualization of the SAM simulation for one event.

SAMs' Benchmarked Parameters	MIRO27		UVS	
Quartz(tungsten) thickness[mm]	13(10)		13(10)	
Quartz Polish	0.98		0.98	
Wrapping reflectivity (0.5 polish)	0.9825		0.9825	
Lightguide reflectivity	0.85	for $\lambda > 350nm$	0.665	for $\lambda > 250nm$
	0.2	for $\lambda < 350nm$	0.6	for $\lambda < 250nm$
PEs (peak)	9(41)		6(22)	
RMS/Mean	0.38(0.48)		0.42(0.49)	

Table 3: Simulation parameters benchmarked with photoelectron distributions for SAM detector with MIRO27 and UVS lightguides with and without tungsten pre-radiator. Values inside parenthesis correspond to distributions where a tungsten radiator was used.

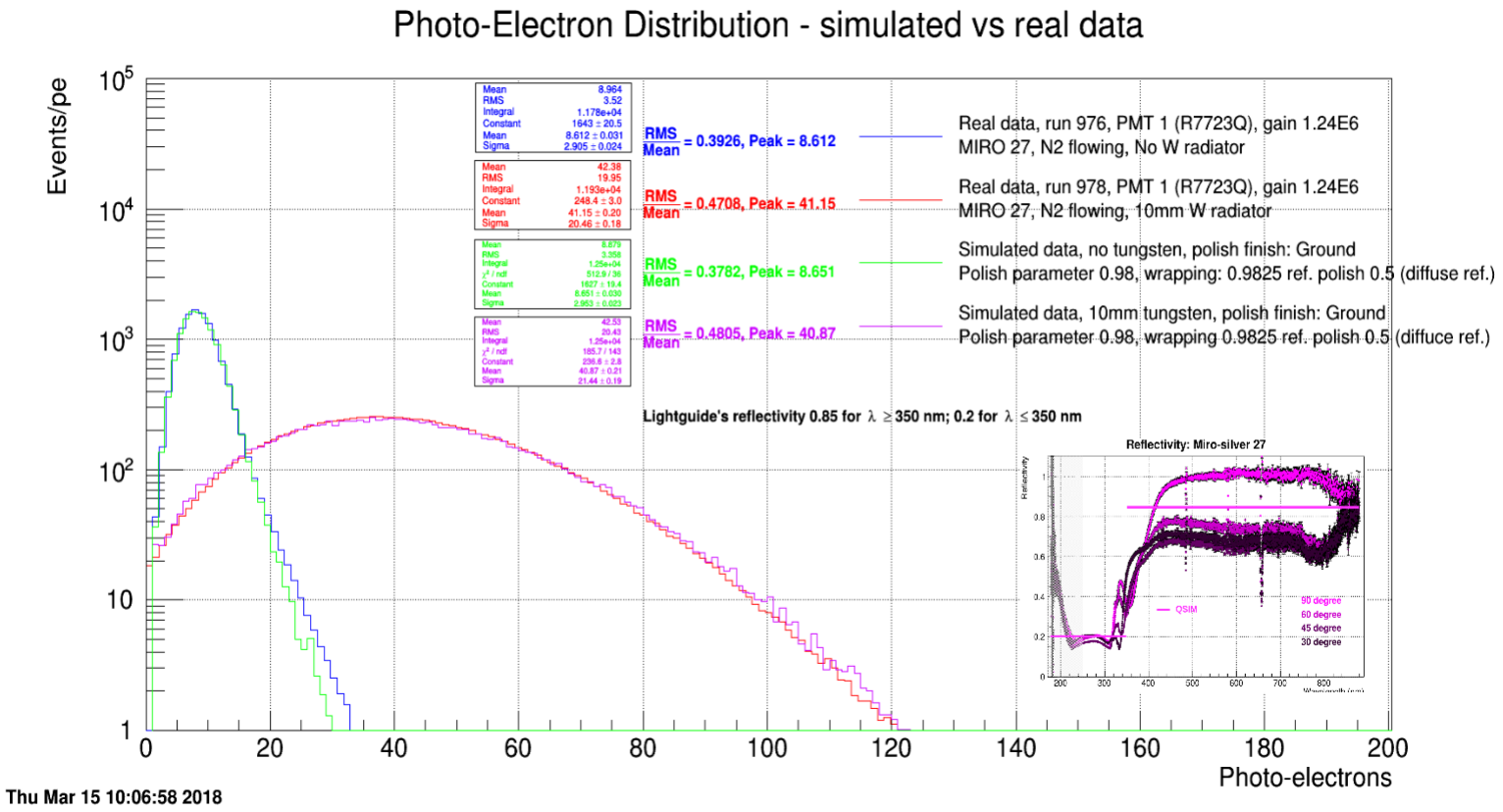

Figure 55: photoelectron distribution for SAM detector with MIRO-27 lightguide. Blue: Real data without 10 mm tungsten pre-radiator. Green: Simulation without 10 mm tungsten pre-radiator. Red: Real data with 10 mm tungsten pre-radiator. Violet: Simulation with 10 mm tungsten pre-radiator. The lightguide reflectivity used is: 0.85 for $\lambda \geq 350$ nm and 0.2 for $\lambda \leq 350$ nm.

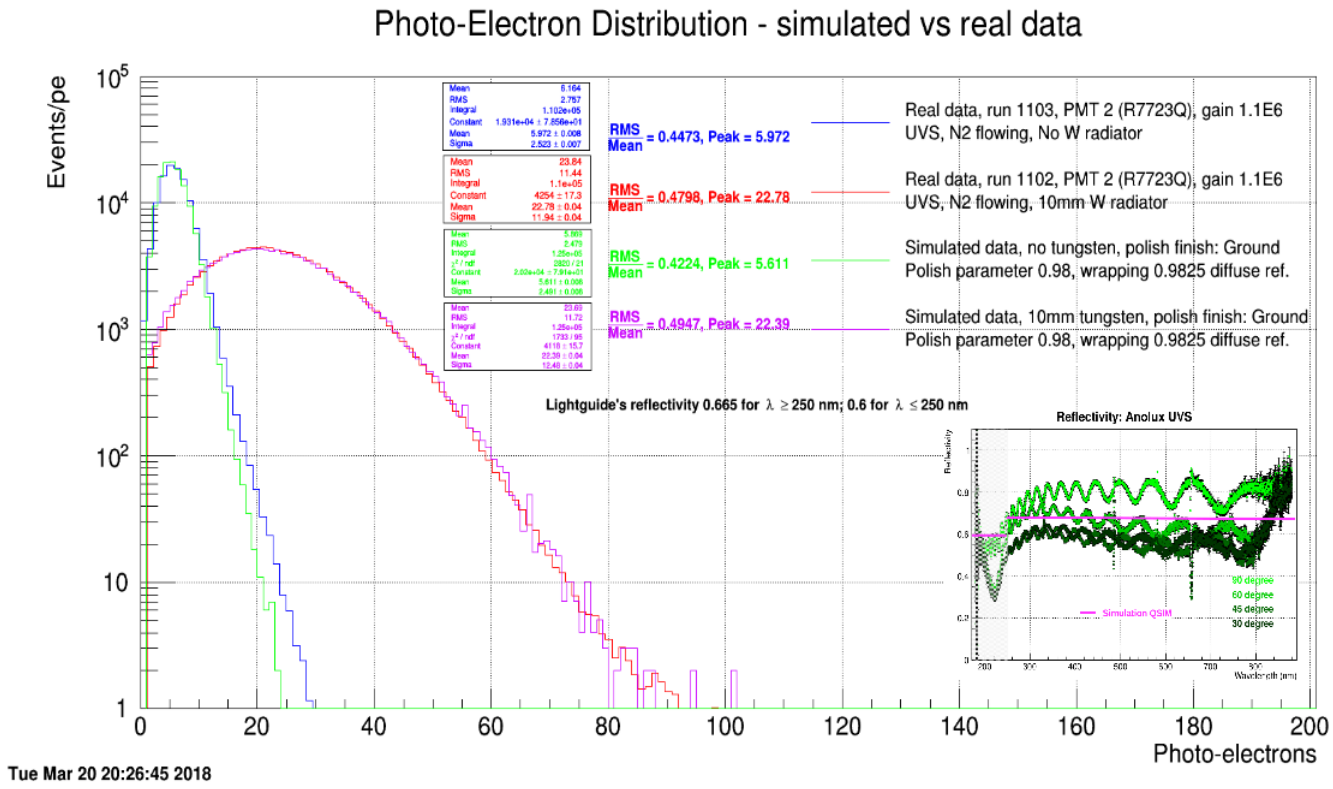

Figure 56: photoelectron distribution for SAM detector with UVS lightguide. Blue: Real data without 10 *mm* tungsten pre-radiator. Green: Simulation without 10 *mm* tungsten pre-radiator. Red: Real data with 10 *mm* tungsten pre-radiator. Violet: Simulation with 10 *mm* tungsten pre-radiator. The lightguide reflectivity used is: 0.665 for $\lambda \geq 250$ nm and 0.6 for $\lambda \leq 250$ nm.

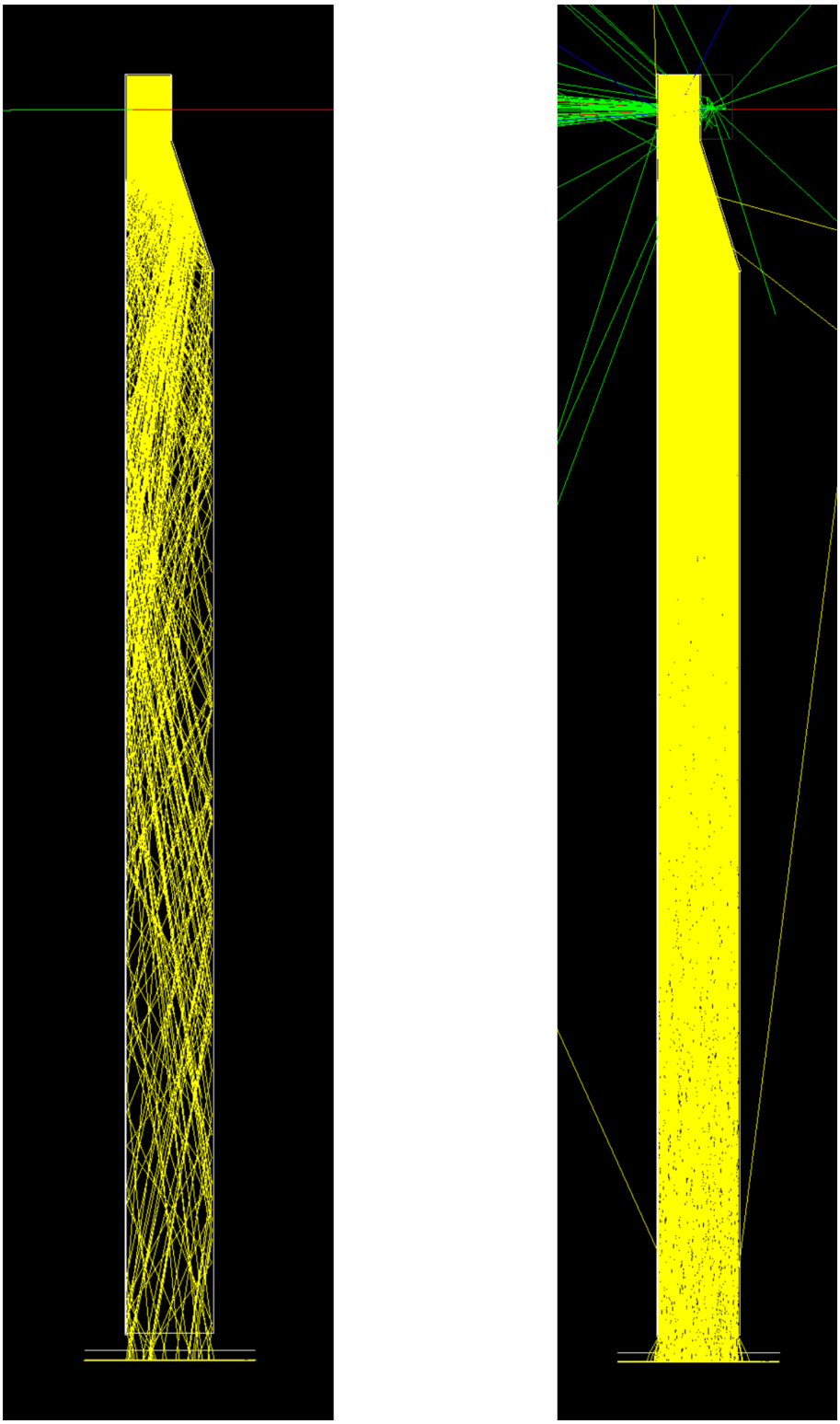

Figure 57: SAM detector visualizations in QSIM. Electron comes from the right The right SAM image has a 1 cm tungsten pre-radiator while the left image has no pre-radiator.

4.2.2 PREX-II/CREX main Detector Prototype Tests

During the 2015 testbeam, the PE yield dependence on the incoming beam angle was studied with a "single-mount" PREX-II/CREX main detector prototype. These angle scans were individually performed for both 6 mm and 10 mm thick unwrapped (bare) Spectrosil 2000 quartz radiators. In 2016, the tandem mount PREX-II/CREX and the initial SAM detector were tested using aluminized Mylar-wrapped quartz tiles. Two Hamamatsu R7723Q PMTs, with measured gain values of 0.98×10^6 (PMT1) and 0.74×10^6 (PMT2) at -2000 V, respectively, were used in the detectors. A CAEN V965 analog-to-digital converter (ADC) with 200 fC/Channel charge sensitivity was used to record the detector signals. This device is also referred to as a QDC since it digitizes the integrated charge within the signal gate.

4.2.3 Data collection

The experimental setup consisted of the PREX-II/CREX main and SAM detector prototypes placed on the rotary stage intersecting the beam line. Two crossed scintillating paddles were placed behind the detector to provide the master coincidence signal which triggered the acquisition of the event. Both the detectors and two trigger paddles were powered by a VME high voltage module CAEN V6533N.
The signal from both scintillators went to a Phillips 715 discriminator set to 75 mV threshold. If the signals surpassed the threshold, they were duplicated with a LeCroy fan-out module so they could be displayed in the oscilloscope. After being duplicated, both scintillators signals were sent to a CAEN N405 logic unit where a AND logic gate checks their timing coincidence. If the two trigger signals overlap in time, the coincidence signal was sent to a logic OR gate to be compared to a clock signal in order to inject pedestal triggers into the data samples.

The signal from the OR logic gate triggers the V965 QDC, which is controlled by a readout unit which supervises the DAQ triggering. The scintillator signals are timed in such a way that they arrive first with enough time to form a timing gate.

The prototype detector signals were delayed (using long cables) so that they arrive at the QDC input at the precise time the trigger gate is established. Figure 58 shows an oscilloscope screen snapshot of the various signals involved in the data acquisition .

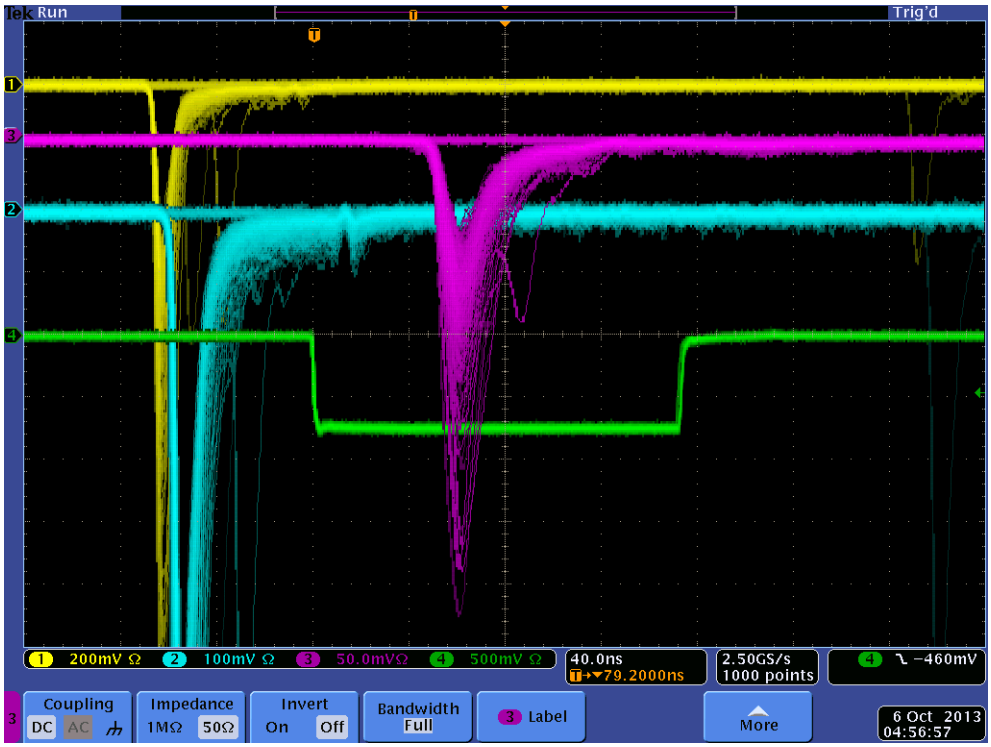

Figure 58: Scintillator signals (cyan and yellow traces) arrive before the prototype (violet) signal, which has been delayed by a long cable such that it arrives within the gate (green trace). This scope snapshot has a 40 ns per division time scale. The coincident gate is 160 ns long. The timing of the prototype signal is set such that it arrives inside the gate approximately 60 ns after the start of the gate. This time gap is required due to the "dead-time" in the QDC when registering the arrival of the gate signal at its input.

4.3 Comparison of QSIM and Mainz Test Beam Data

The data collected during the beam tests can be used to benchmark various simulation parameters. This is done by setting and controlling as many parameters in the simulation as possible and then allowing one or two parameters to be varied in order to best match the real and simulated data (PE) distributions.

One of the most important simulation parameters is the QSIM quartz polish which can vary depending on the specific tile used, the manufacturer, and the type of polishing technique used. In order to tune the polish parameter in QSIM, one needs to compare real data with simulation. To do so, the real data (acquired by the ADC) has to be converted from raw ADC values, which range from 0 to 2^{12} into photoelectrons. Following the pedestal subtraction from the raw ADC signal, the conversion to PEs is given by the ratio of the ADC sensitivity (200 fC per channel) and the gain of the PMTs used. The gains of all PMTs used during the tests were known at the 5 - 10% level (refer to section 2.5.4). The conversion of the raw ADC signal to PEs is given in the equations below, where $\#ADC$ is the pedestal-corrected ADC value of an event and $\#PEs$ is the corresponding number of photoelectrons; all high voltages were set to 2000 V.

$$\#PEs \times (1.602 \times 10^{-4} fC) \times Gain = \#ADC \times 200 fC/Ch, \tag{25}$$

where $Gain(PMT1) = 0.98 \times 10^6 \pm 10\%$ and
$Gain(PMT2) = 0.74 \times 10^6 \pm 10\%$, gives

$$\#PEs = 1.274 \times \#ADC(PMT1), \text{and} \tag{26}$$

$$\#PEs = 1.687 \times \#ADC(PMT2). \tag{27}$$

Equations 26 and 27 can be used to calculate the number of PEs for each ADC value which is specified as a number of ADC channels. For PMT1, each ADC channel is equivalent to 1.274 photoelectrons, and for PMT2, each channel is 1.687 photoelectrons.

In 2015, the PE yield of the single mount PREX-II/CREX prototype with a 6 mm thick unwrapped Spectrosil 2000 quartz crystal was measured at various incident angles when irradiated with the pinpoint 855 MeV Mainz electron beam. This first

measurement result is shown in Figure 59 along with the QSIM expectation. Note that prior to achieving this result, the simulation's fixed parameters were vetted as best as possible and the quartz polish parameter was tuned. A polish of 0.98 was found to give best agreement.

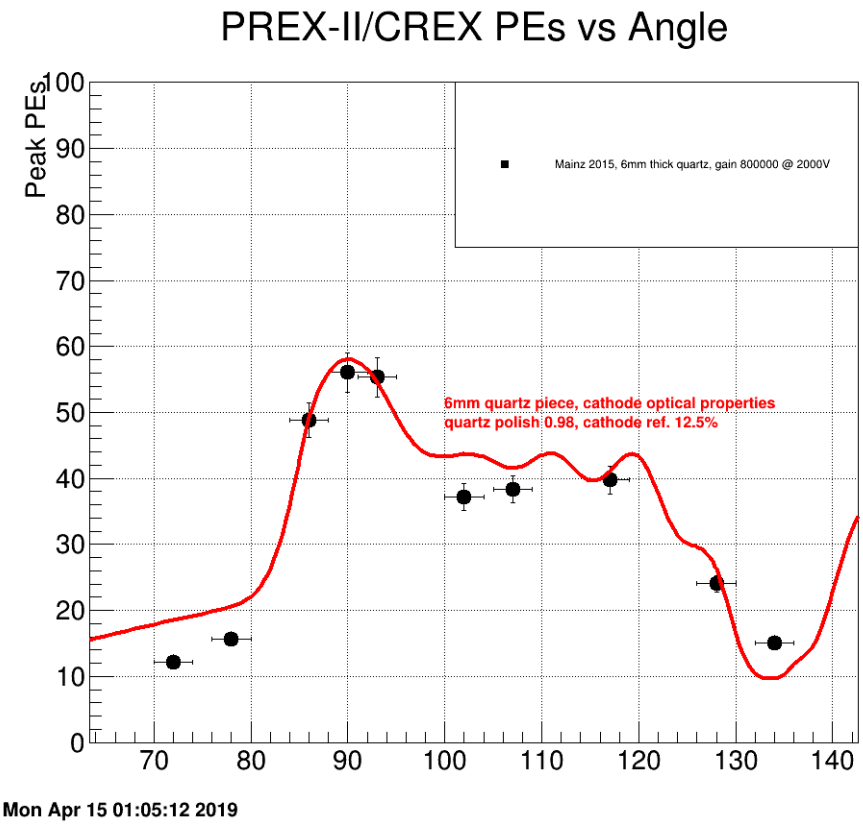

Figure 59: Photo-electron yield distribution peak value versus incident angle (90 deg is when the quartz piece is perpendicular to the beam). R7723Q PMT gain is 0.8×10^6. The QSIM polish parameter is 0.98 and cathode reflectivity of 12.5%. Note that the precision in the measured angle is estimated at ±2 deg due to the analog nature of its readback.

The QSIM polish parameter is tuned to match the peak PE value at 90 ± 2 deg beam incidence, then the same polish parameter (0.98) is applied to the data for the other angles. The simulation shows agreement within the 5% experimental error of the data points near ~ 90 deg, but some disagreement between data and simulation is seen at other angles far from 90 deg. Moreover, the wriggles seen in the simulation are not necessarily seen in the data, although the data's angular granularity is large.

Overall "reasonable" agreement is seen here, as the data follows the general trend of the simulated expectation: minimum at 45° and 135° and maximum at 90° with a plateau region between 100° and 120°.

In 2016 the tandem mount PREX-II/CREX prototype was tested using aluminized-Mylar wrapped around 6 mm and 10 mm thick quartz pieces. We again used our same Hamamatsu R7723Q PMTs (#1 and #2), which have quartz windows for UV detection. Figures 60 and 61 compare the data and simulation. They show agreement in the mean, peak and RMS values inside the 5% experimental uncertainty. Note that the MAMI testbeam allowed very high statistics data collection in relatively short time–allowing more tests with more precision to be conducted. The benchmarked parameters for the quartz polish and Mylar reflectivity from this testbeam study are given in Table 5

Figure 62 shows the mean, peak, RMS and resolution values for the photoelectron distributions in Figures 60 and 61. Some of these values are resumed in table 4. The major contribution to the experimental error (red bars) is the uncertainty in the PMT's gain. The statistical error in the simulated data is very small in comparison to the systematic error of the real data. The values from simulated distributions are contained inside the experimental error, therefore it can be claimed that the simulation is accurate at the level we know the gain of the PMT used.

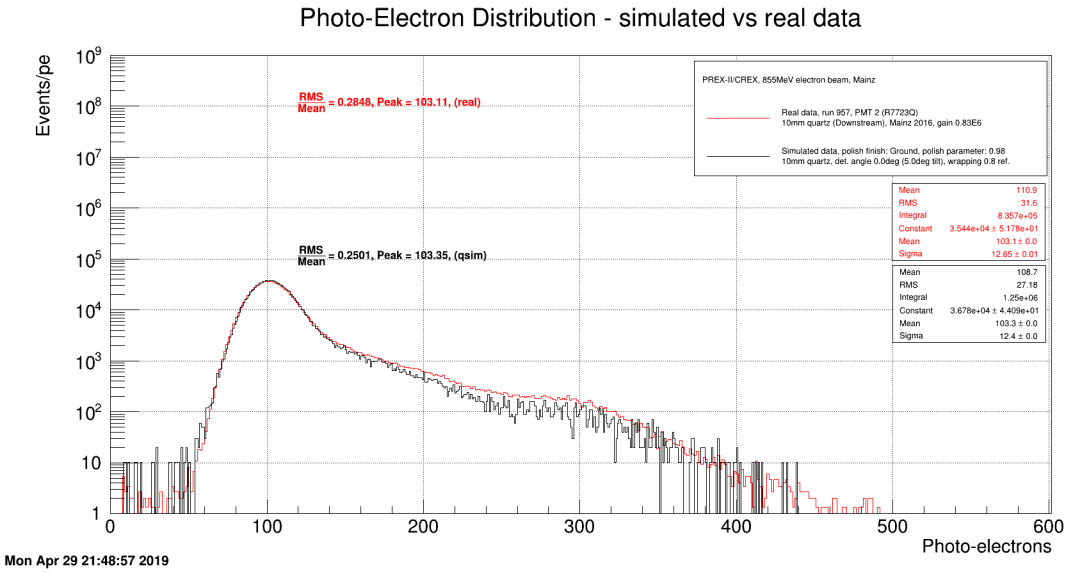

Figure 60: PREX-II/CREX tandem detector PE distributions. Real (red) and simulated (black) data for the Downstream 10 mm thick, aluminized-Mylar wrapped quartz tile. Note the effect of the 6 mm thick tile, that is upstream of the 10 mm tile, is to enhance the Landau (delta-ray) high-light tail and worsen the resolution.

PREX-II/CREX Prototype - peak PE and resolution

Thickness $[mm]$	PMT1 gain$[10^6]$[5]	PEs-peak	δ(PEs-Peak)	RMS/Mean	δ(RMS/Mean)
6	0.95	46.58	2.25	0.1992	0.023
6	0.97	57.19	2.83	0.2088	0.022
10	0.65[6]	90.46	4.52	0.1706	0.016
10	0.92	106.76	5.01	0.2032	0.017

Table 4: PREX-II/CREX main detector prototype. Peak PEs and resolution values.

PREX-II/CREX Prototype - simulation benchmarked parameters

Thickness $[mm]$	Polish parameter	wrapping reflectivity[7]	PEs-peak	δ(PEs-Peak)	RMS/Mean	δ(RMS/Mean)
6	0.98	n/a	47.08	0.01	0.2038	0.00042
6	0.98	0.8	57.00	0	0.1865	0.00038
10	0.98	n/a	89.77	0.01	0.185	0.00038
10	0.98	0.8	106.81	0	0.1857	0.00038

Table 5: PREX-II/CREX main detector prototype. Simulation benchmarked parameters.

[5]The measured values is $0.98 \times 10^6 \pm 10\%$
[6]StonyBrook's PMT
[7]Aluminized Mylar

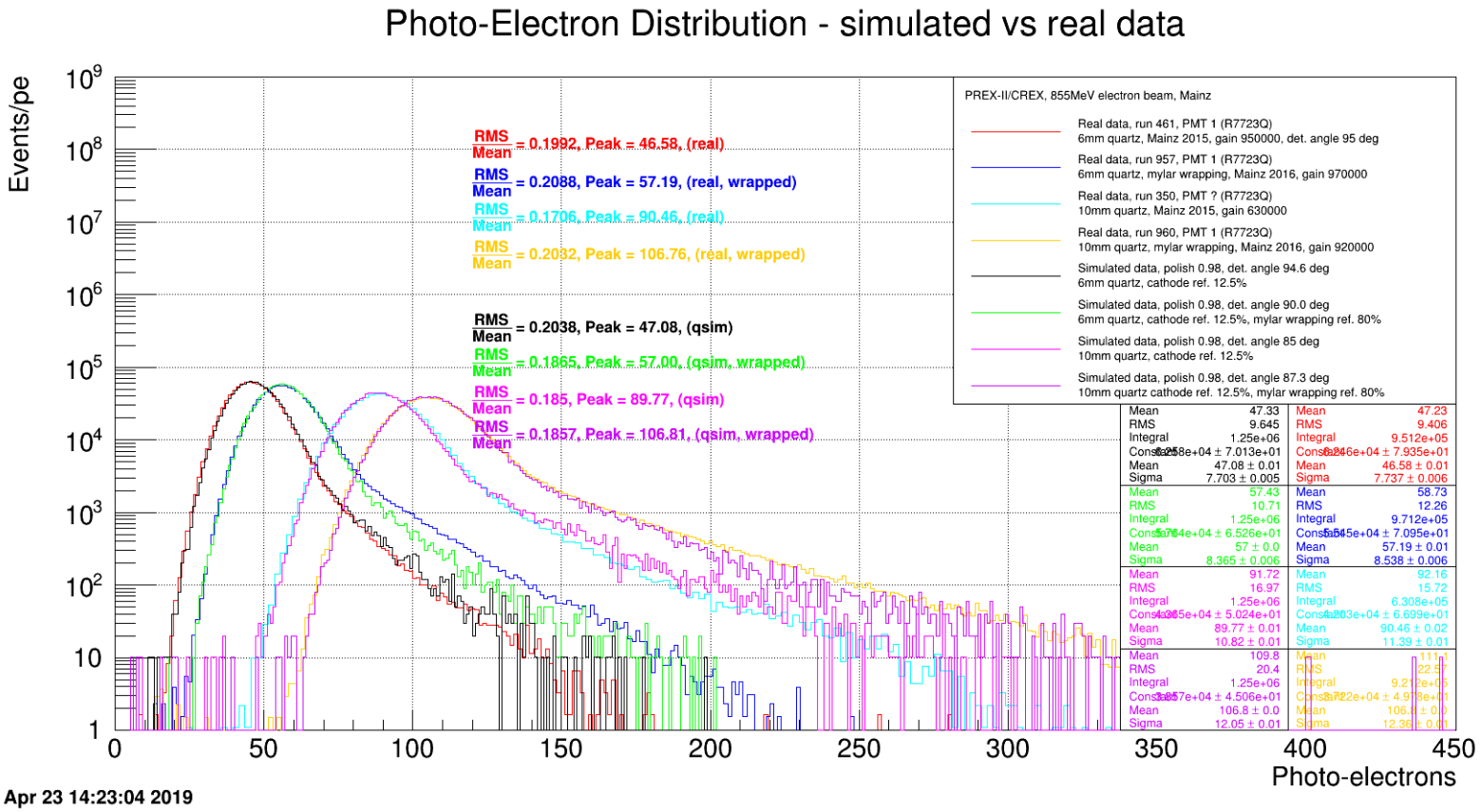

Figure 61: PREX-II/CREX tandem mount PE distributions: real and simulated for Upstream 6 and 10 mm quartz, wrapped and unwrapped. For 6 mm thick quartz (bare): Red (real) and black (simulated). 6 mm thick quartz (wrapped): Blue (real) and green (simulated). For 10 mm thick quartz (bare): Cyan (Real, data taken with a different PMT and quartz piece belonging to Stony Brook group) and purple (simulated). 10 mm thick quartz (wrapped): Yellow (real) and magenta (real).

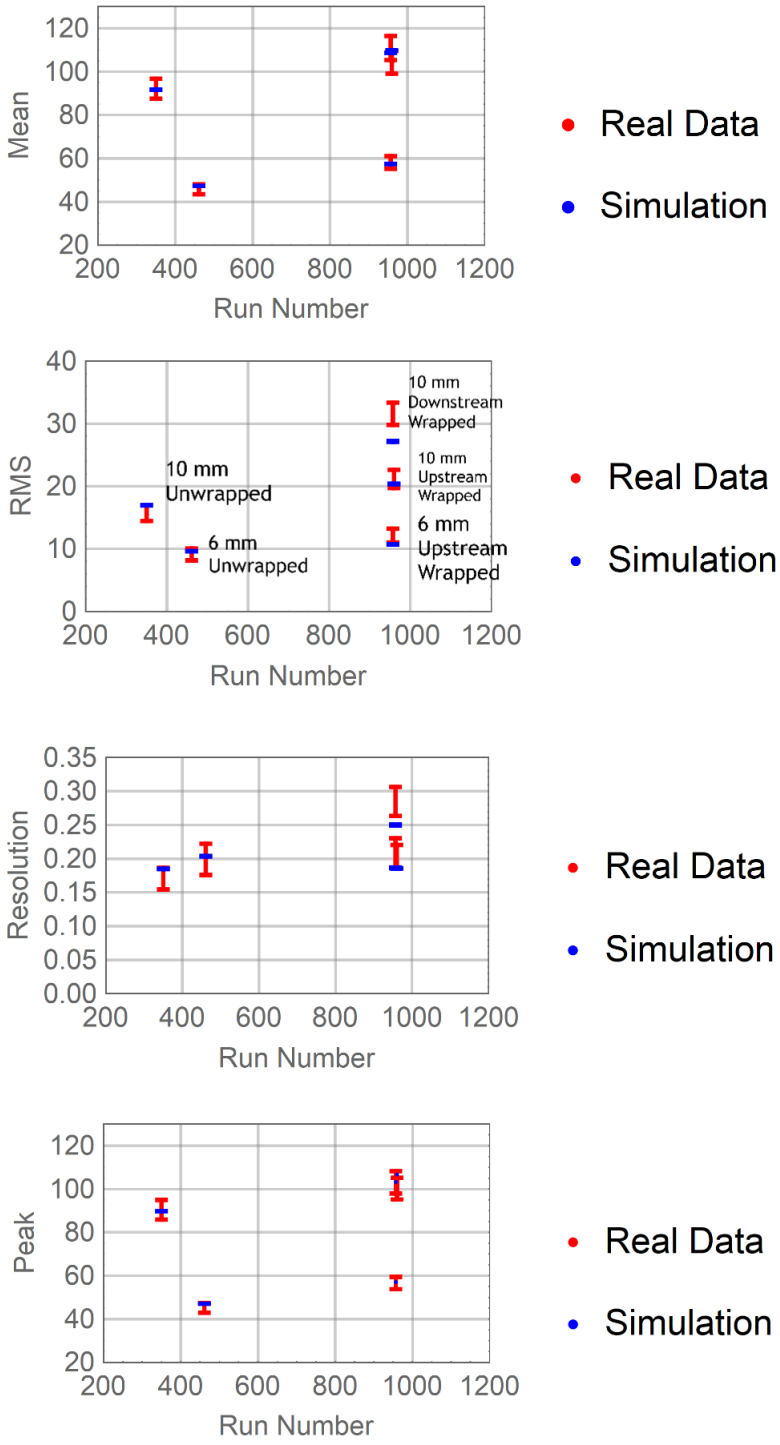

Figure 62: Mean, peak, rms and resolution values with their respective errors from the distributions in Figures 60 and 61. A gain of $0.98 \times 10^6 \pm 5\%$ for PMT1 is assumed. The major contribution in the experimental error (red bars) is the uncertainty in the gain value.

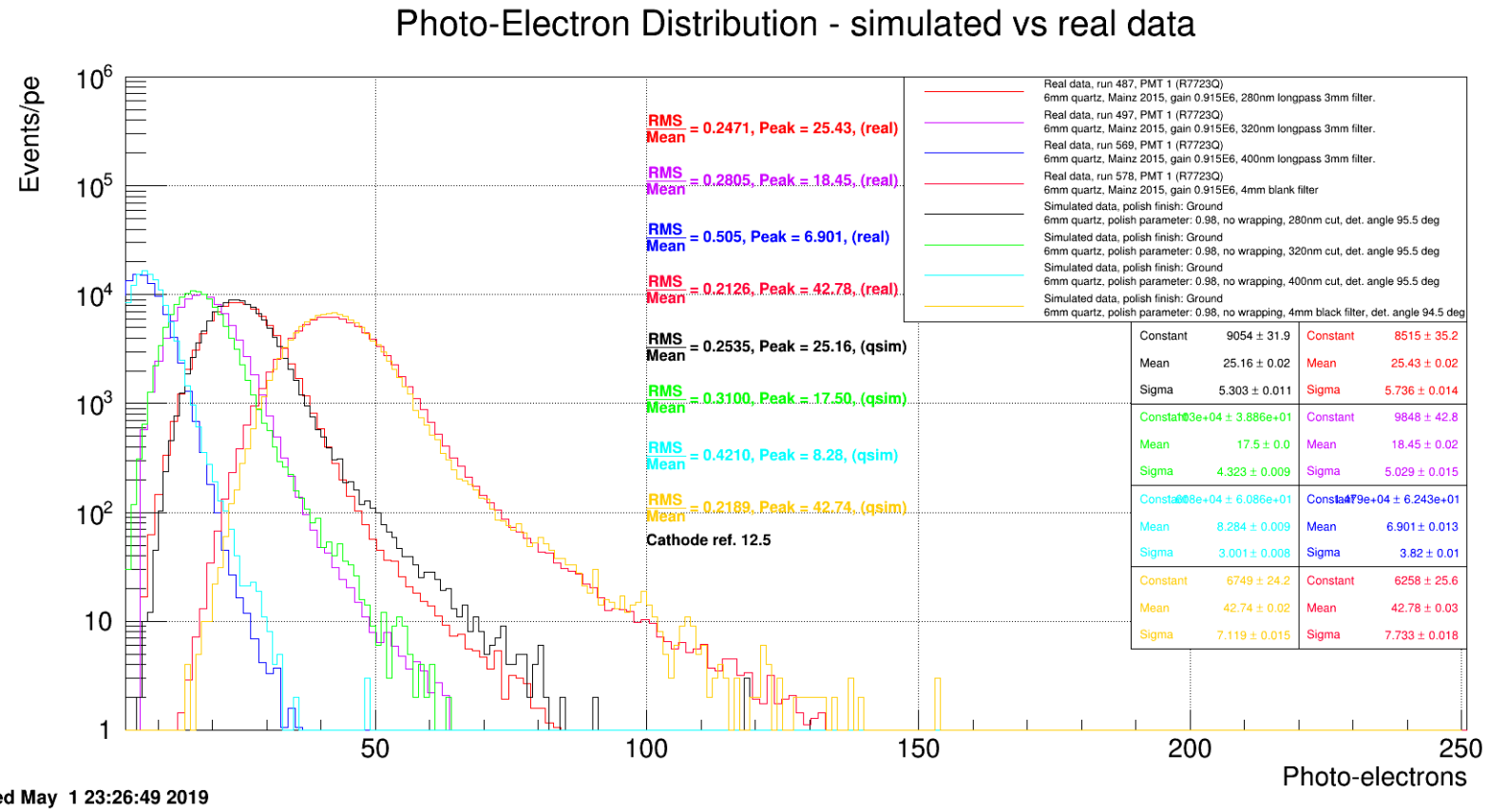

Figure 63: PE distributions, real and simulated, for PREX-II/CREX Upstream, 6 mm detector, using various filters: 3 mm thick, 280 nm, 320 nm, and 400 nm long-pass filters and a ”blank” calibration filter made of a 4 mm thick UV quartz. This data allows a check of QSIMs Cerenkov light generation and our quartz dispersion table. When the same filters are applied to QSIM, the simulated data matched the real data.

Another detailed study performed in 2015 at MAMI was a light filter study using long-pass filters. That is, filters that allow wavelengths of light above a specified minimum cutoff to pass through while blocking shorter wavelengths. A filter holder mechanism was designed to fit in between the PMT window and the quartz bevel for the PREX-II/CREX detector. Data was taken for the Upstream, 6 mm thick quartz using three different long-pass filters with cutoff wavelengths of 280, 320, and 400 nm. In addition, a "blank" filter made of fused-silica quartz (UV transparent) was used to calibrate the measurements which are shown in Figure 63 along with their corresponding simulated data.

The relative differences in the mean values from simulated and real distributions are between 1.23% (6 mm wrapped) and 5% (10 mm wrapped). These values are consistent within the 5% experimental uncertainty in the PMT's gain measurement. The relative differences in the RMS values are between 3.9% (10 mm wrapped) and 16.3% (10 mm wrapped downstream). This last value, corresponding to the 10 mm thick wrapped quartz piece placed downstream the beam in the PREX-II/CREX tandem detector, presents the major difference between simulated and real distributions (see Figure 62).

Overall, the comparison indicates that the Geant4 Cerenkov production mechanism and quartz dispersion table inputs are accurately representing the distribution of photons emerging from the quartz bevel and incident on the PMT. The simulated distribution of Cerenkov photon wavelengths from the filter study are displayed in Figure 64. One can see from this figure the effect of the wavelength or energy cutoff (sharp vertical lines) on the spectra. A QSIM visualization of a single MAMI electron beam event for the PREX-II/CREX tandem detector is shown in Figure 65.

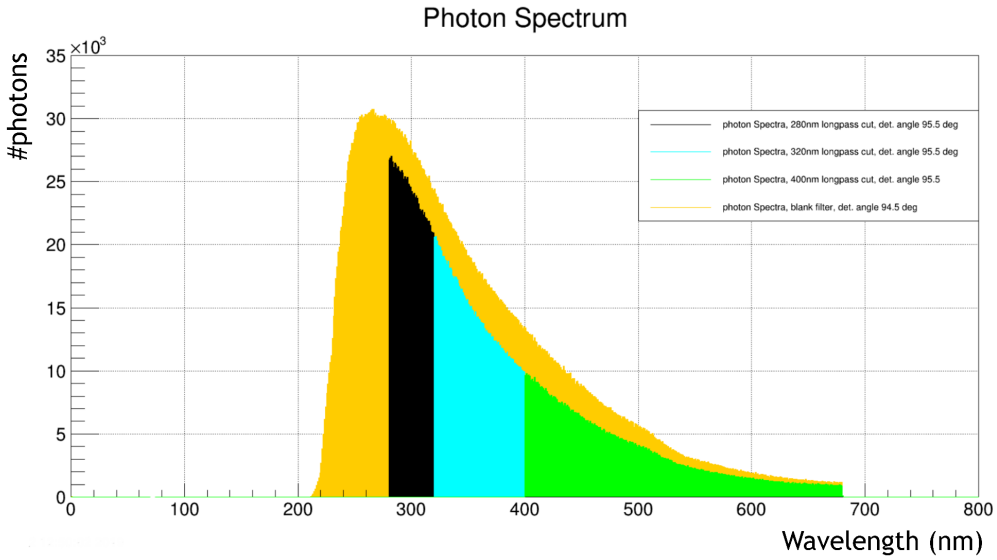

Figure 64: Photon spectrum sensed by the cathode. Black, cyan, and green areas corresponds to 280 nm, 320 nm and 400 nm filters, respectively. The yellow area corresponds to the blank filter area, it stands taller compared to the other areas because of a slight difference in the detector angle (closer to 90 deg). The peak in the Cerenkov spectrum occurs between 250 - 280 nm.

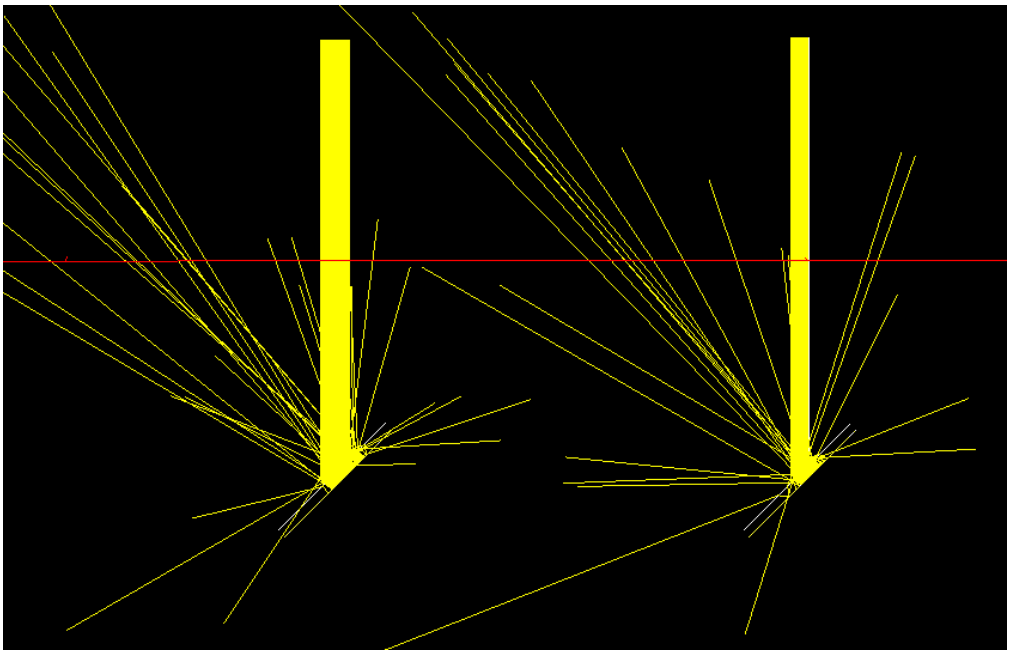

Figure 65: PREX-II/CREX detector visualization in QSIM. Electron travels from right to left.

4.4 2018 SLAC Beam Test

In early December 2018, a beam test was carried out at the End Station A Test Beam (ESTB) facility at SLAC (see Figure 66). It can provide a varied range of energies from ∼2 GeV to ∼16 GeV, beam intensities that range from a single electron (which is what we want) up to $\sim 10^9$ electrons per pulse at a rate of 5 Hz.

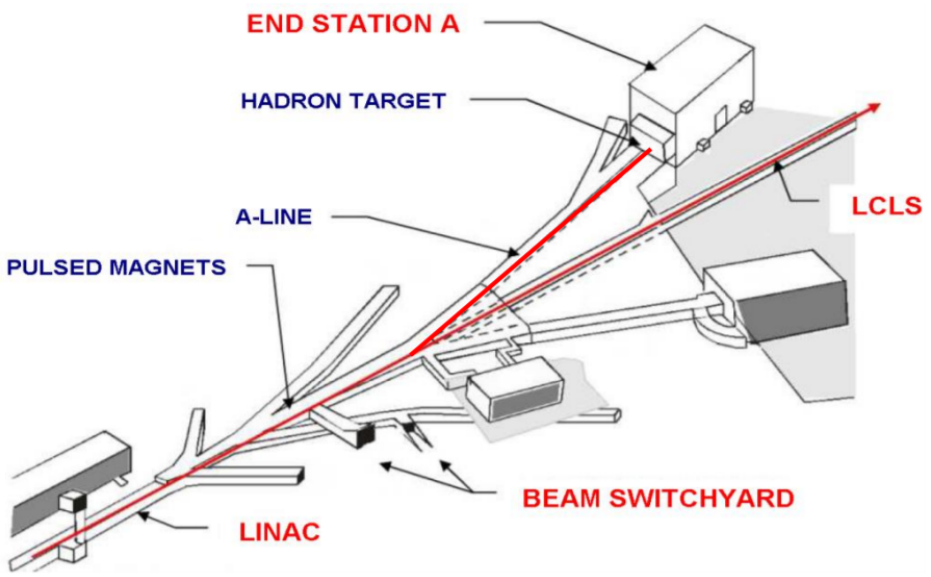

Figure 66: ESTB facility at SLAC. The beam from the SLAC linac, created for the Linear Coherent Light Source (LCLS) project parasitically siphoned off to End Station A to provide a 5 Hz testbeam with electron multiplicities that follow Poisson statistics with a mean near one.

Several detectors were tested including the PREX-II/CREX final main detector, with a 6 *mm* thick quartz pieces placed upstream, and a 10 *mm* thick quartz piece placed downstream, the same pieces used during the Mainz beam test. Note that we wanted to test 5 mm thick quartz, but the new pieces did not arrive in time for the beam test. The MOLLER Shower-max full-scale and benchmarking prototypes were tested as well. Schematic CAD views of the test beam stand with benchmarking shower-max and PREX-II/CREX detector assemblies are shown in Figures 67 and 68.

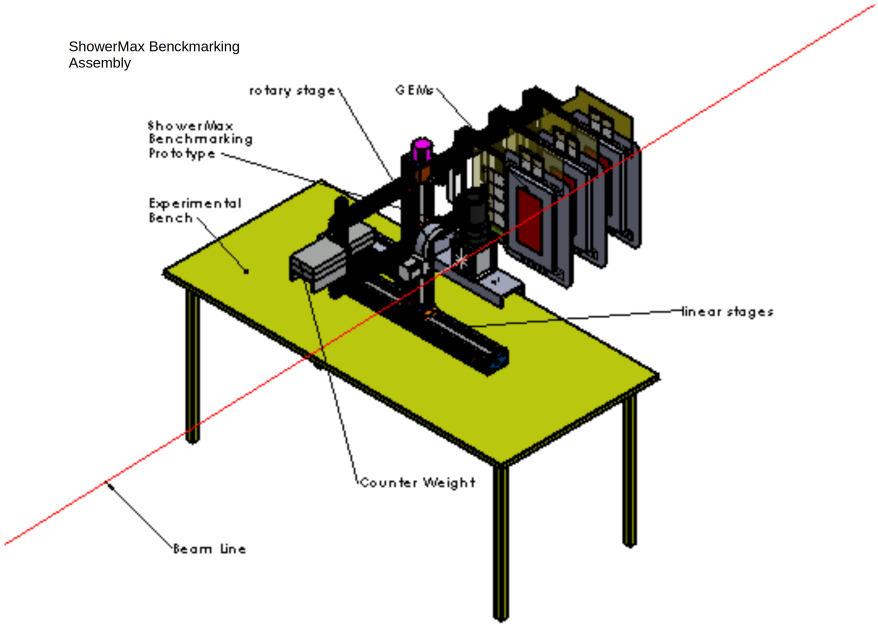

Figure 67: Shower-max benchmarking detector and SLAC test beam stand CAD. The beam (red line) travels from the top right of the figure, goes through three Gaseous Electron Multipliers (GEMs) and through the benchmarking prototype.

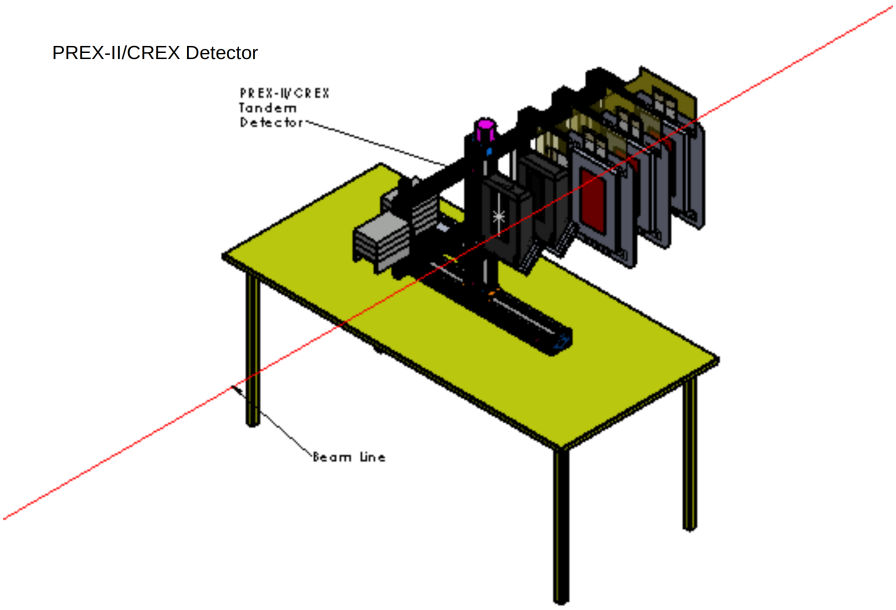

Figure 68: Same CAD as in Figure 67 but for the PREX-II/CREX final tandem detector. The three GEMs are required for tracking beam electron trajectories and multiplicity.

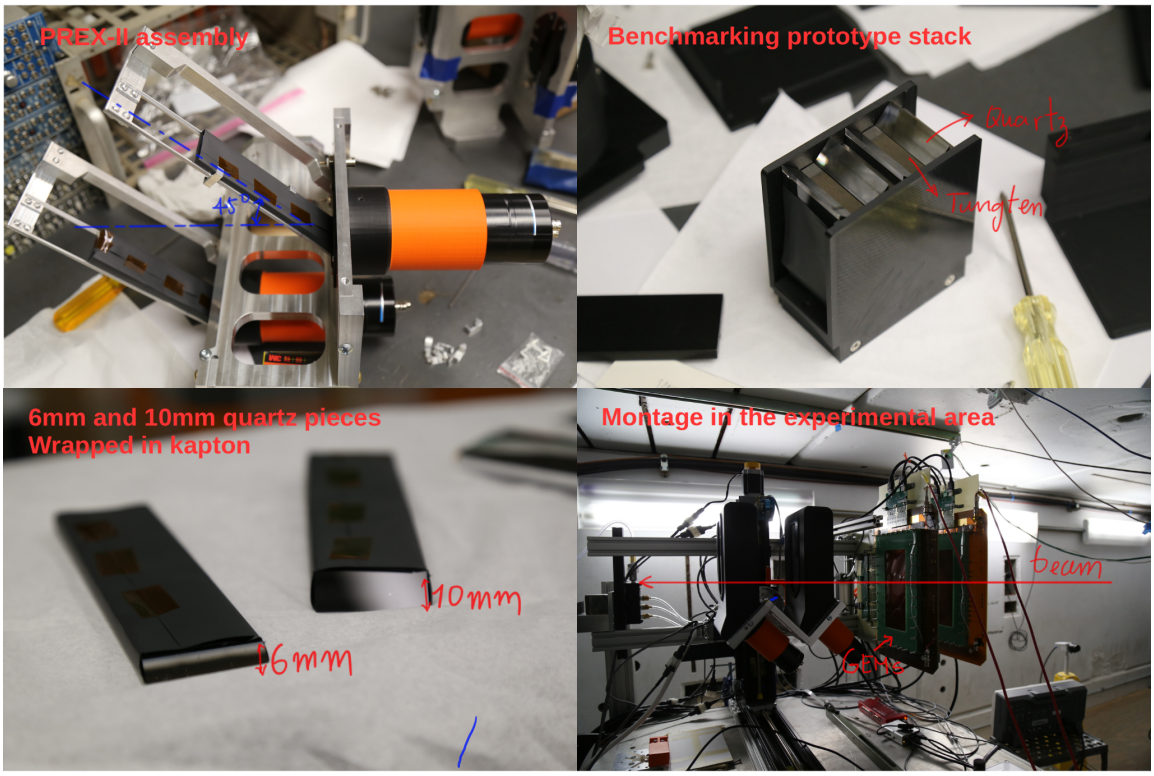

Figure 69: Top left: PREX-II/CREX assembly. Top right: Quartz-tungsten stack for benchmarking prototype. Bottom left: 6 mm and 10 mm thick quartz pieces for PREX-II/CREX detector wrapped in Kapton. Bottom right: PREX-II/CREX detector over the experimental area. GEM's can be seen placed upstream the beam.

Photos showing details of the PREX-II/CREX detector and the Shower-max benchmarking prototype and SLAC test beam stand are shown in Figure 69. The detectors were assembled in a room adjacent to the End Station A before bringing them into the experimental area and installing in the test stand (one detector at a time). This was done in order to optimize the use of beam time and minimize the radiation exposition of tools and other objects that don't need to be present inside the End Station when the beam is on. The Shower-max quartz pieces were covered with a thin (3 mil) light tight Kapton polyimide film to protect them from scratches when sandwiched with tungsten. The PREX-II/CREX quartz was also wrapped with the Kapton to possibly improve resolution. Many of the detector parts were made with Ultimaker 2+ and s5 3D printers, reducing time and cost of fabrication as well

as allowing more flexibility in custom part designs. Figure 70 shows a visualization of a single electron event during the SLAC test beam.

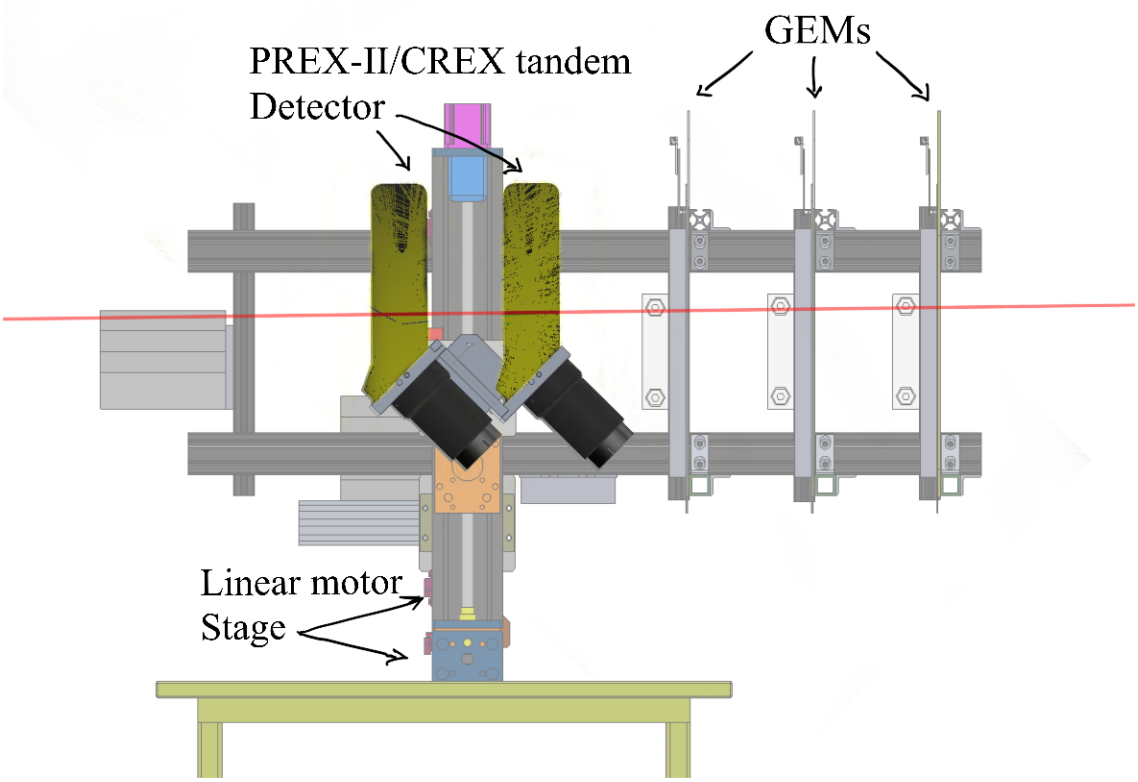

Figure 70: Visualization of one 5.5 GeV electron (red, travels from right to left) hit on the PREX-II/CREX detector during the SLAC beam test. The electrons first go through the 3 GEMs and then through the PREX-II/CREX tandem detector. The 6 mm quartz piece is placed upstream and 10 mm is placed downstream.)

The 16-channel CAEN V965 QDC was used to digitize the signal from the detectors. Initially, a coincidence signal from two crossed scintillator paddles, placed just downstream of the test stand and detector assembly, was used to trigger the data acquisition. Later, a Linac RF pulse signal from the accelerator was used as the trigger. Given the Poisson statistical nature of the beam's electron multiplicity, that is sometimes there were 0, 1, 2, or 3, ... electrons at a time in the beam, Gaseous Electron Multiplier (GEM) detectors [37] were needed to track beam particles in order to ensure proper alignment between beam and detector and identify the single electron beam events.

The characteristics of the SLAC testbeam were vastly different from the MAMI testbeam. While the MAMI beam was a pin-point, single electron beam, the SLAC beam was spread-out over approximately a 1 cm by 2 cm horizontal tear-drop shape (see Figure 71). However, the SLAC ESTB is the only facility in North America (and possibly the world) that can provide 10 GeV-level electron testbeam energies. Figures 72 and 73 give a sense of the GEM tracking data collecting during the tests.

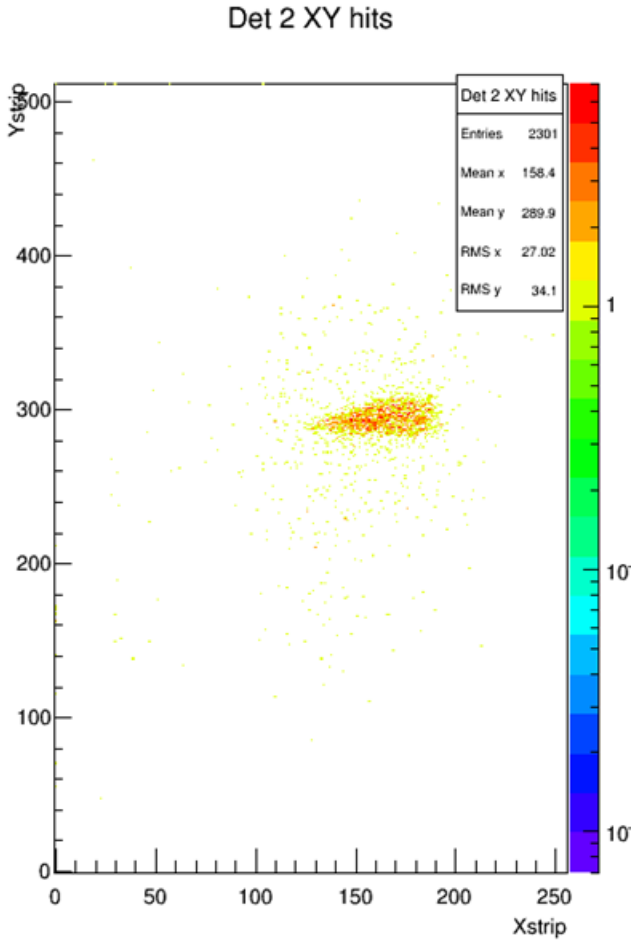

Figure 71: 2D map of electron hit on one GEM (10 cm $\times$ 20 cm sensitive area with 400 μm, xy-pitch). The SLAC 5.5 GeV electron beam spot for the ESTB facility is a fairly well defined $\sim$ 1 cm $\times$ 2 cm "tear-drop" shape.

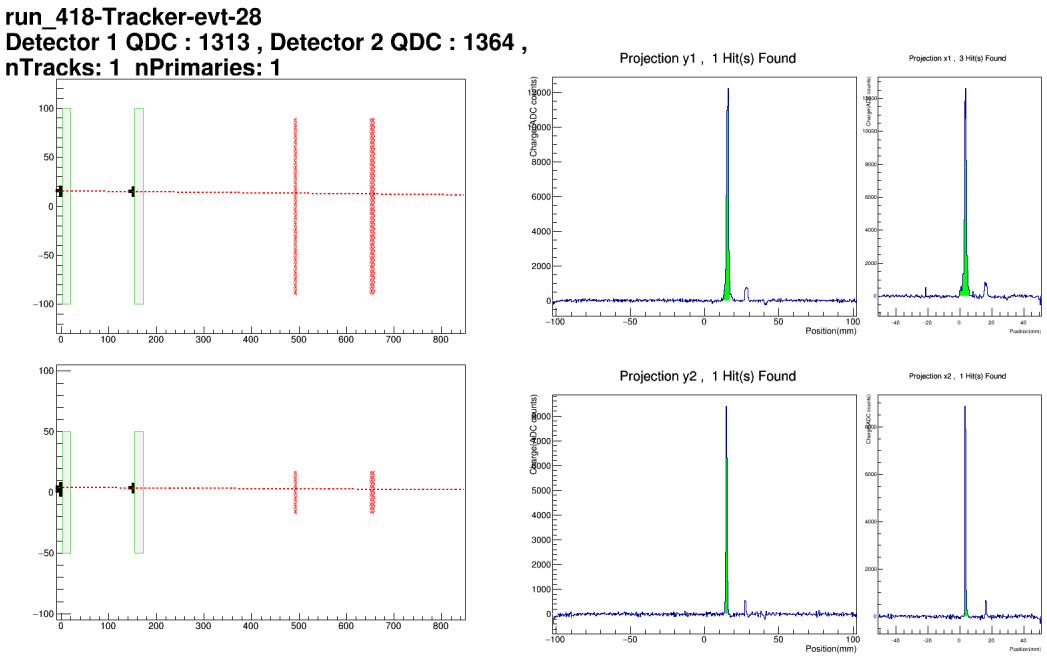

Figure 72: GEM-based event visualization for the SLAC test. Left-top: side view of two GEMs and tandem quartz; Left-bottom: top view. Electron tracks are in red (a single track can be seen in this particular event), green areas correspond to two GEM detectors, red lines correspond to the two Tandem detector quartz pieces (6 mm and 10 mm thick). Right: GEM ADC charge collected by the GEMs projected onto vertical (top plot) and horizontal (bottom plot) axes. GEM analysis by Tao Ye of the Stony Brook group.

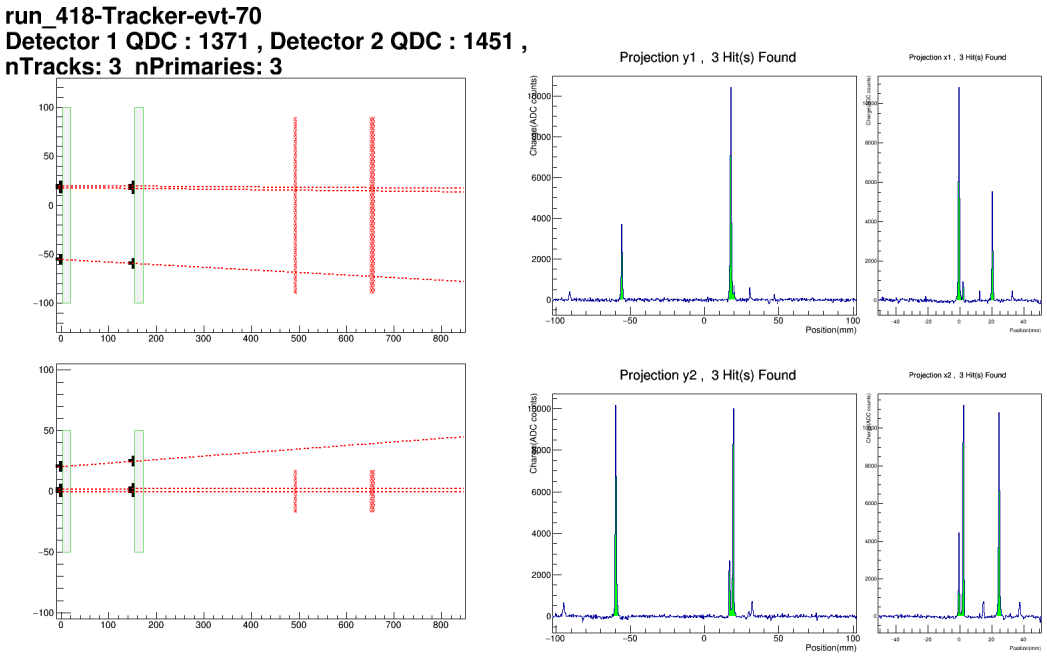

Figure 73: Same as Figure 72 except for a three-track event.

The high energy capability of the SLAC testbeam is needed to test the MOLLER shower-max detector which has a light response that is proportional to the incident electron energy. It should be noted here that the single thin quartz, PREX-II/CREX detectors give the same light flash regardless of the particle energy–as long as the particle is highly relativistic (above the threshold for Cerenkov production). The SLAC electron beam was set to 3, 5.5 and 8 GeV at a very low intensity; as stated, the number of electrons per event follows a Poisson distribution with a mean near 1 and at a rate of 5 Hz (very slow data collection).

4.4.1 PREX-II/CREX Detector Test Results

Sample SLAC testbeam results for the PREX-II/CREX 6 mm and 10 mm quartz pieces in the upstream and downstream positions, respectively, are given in Figures 74 and 75. One can immediately see the Poissonian character of the beam multiplicity. The first peak in these PE distributions corresponds to 1-electron events, the second peak corresponds to 2-electron events and so on. Up to 3- or 4-electron events can be easily distinguished. While these figures are specifically from the 8 GeV beam energy runs, for the single, thin quartz PREX-II/CREX detectors, they are the same as the results from the 3 and 5.5 GeV beam energy data (these detector's signals have no energy dependence). The following details apply to all the result plots shown in this section: the black lines are the real data, the red lines are the simulated data, including the precise beam multiplicity (from Poisson fits to the data spectra). The blue lines are the simulated 1-electron response of the detector. The 2" PMT high voltages are set to maximum (-2000 V), the quartz radiators are all near 90 deg normal beam incidence, and they are wrapped in black, light tight polyimide Kapton film (except for the bevel cut which is $\sim$3 mm from the PMT window). The 1-electron critical performance parameters, peak PE yield and resolution (RMS/Mean), are also given on the plots.

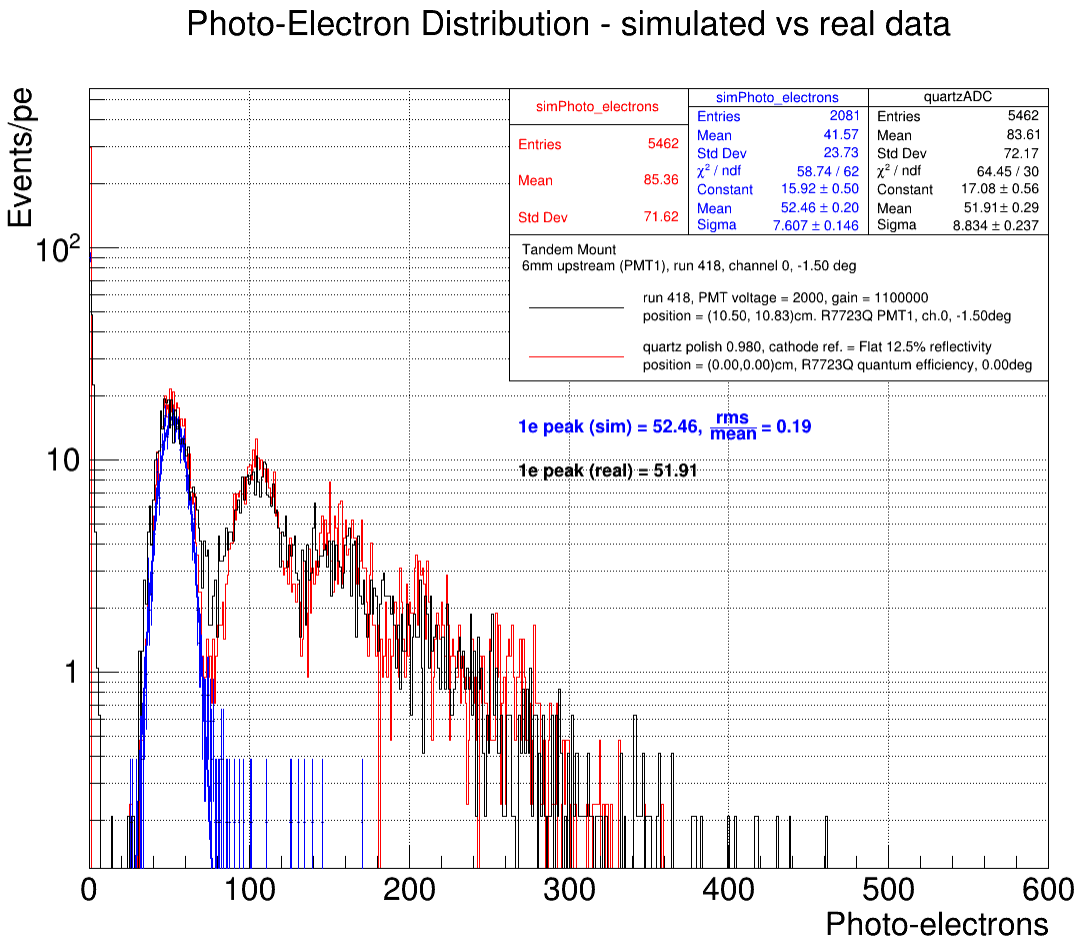

Figure 74: SLAC data (black) and QSIM simulation (red) for PREX-II/CREX tandem detector 6 mm thick Upstream quartz using PMT1. Note the statistical precision of the data is much lower than for MAMI testbeam due to 5 Hz bean rate.

In the case of the 6 mm thick quartz piece, data gives ∼52 peak photoelectrons per event. The SLAC data agrees with QSIM using a gain of 1.1×10^6 for PMT1 at -2000 V, somewhat higher than the measured value of 0.98×10^6 at -2000 V; its resolution for the 1-electron response is 19%. For the 10 mm quartz piece, SLAC data gives ∼100 peak photoelectrons per event. The SLAC data agrees with the simulation at a gain of 0.725×10^6 for PMT2 at -2000 V, a little lower than the measured value of 0.74×10^6 at -2000 V. Again, the downstream quartz shows markedly worse resolution (29%) due to the presence of the upstream quartz causing increased multiple scattering, Bremsstrahlung, and delta-ray production of the beam electron(s).

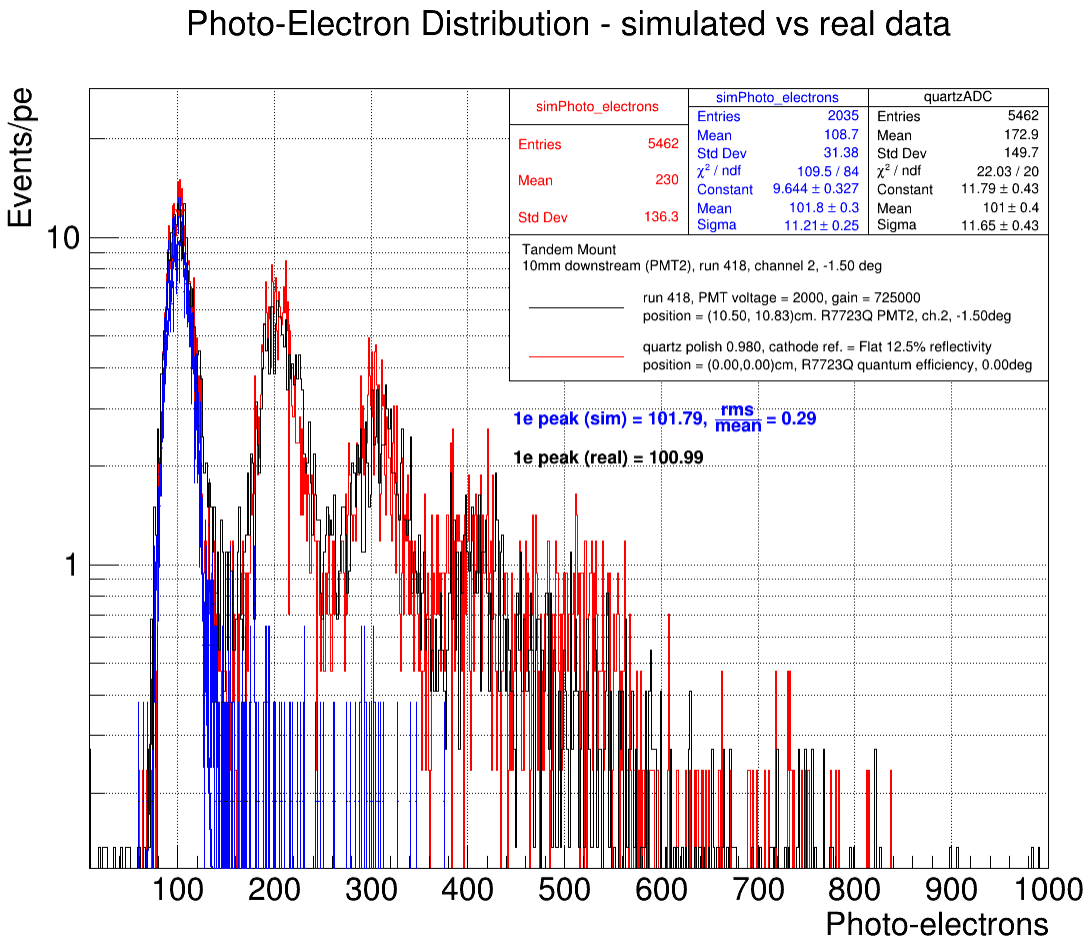

Figure 75: SLAC data and QSIM simulation for PREX-II/CREX tandem detector 10 mm thick Downstream quartz using PMT2 and very near perpendicular incident beam trajectory.

As a check of the above results, given that the PE yields were slightly elevated as compared to MAMI test results, and that the PMT gains had to be tweaked to get QSIM to agree with data, we decided to swap the PMTs between the 6 mm and 10 mm quartz and take data. The results of these tests are given in Figures 76 and 77.

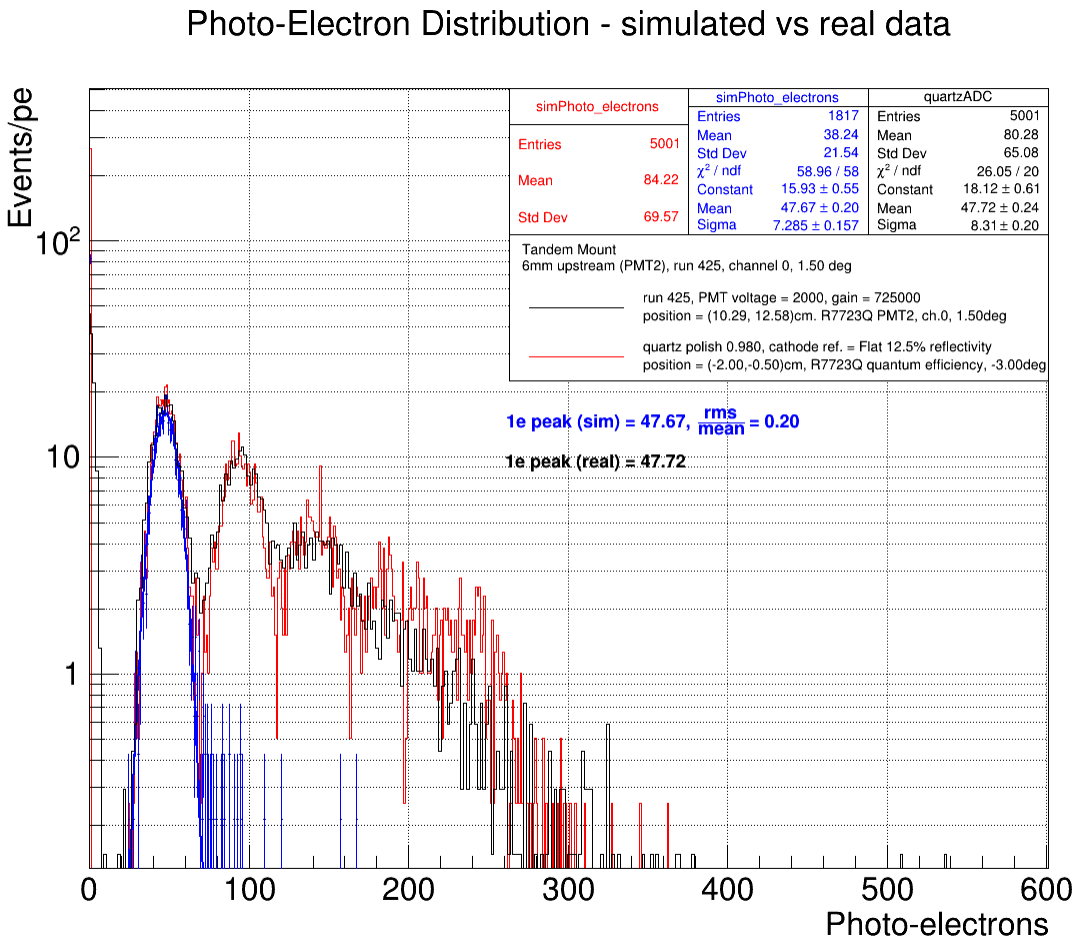

Figure 76: SLAC data and QSIM simulation for PREX-II/CREX tandem detector 6 mm thick Upstream quartz using PMT2 and perpendicular incident beam angle. PMT2 was swapped for PMT1 relative to Figure 74.

These 'swapped' results are in reasonable agreement with the 'un-swapped' results, however there are some puzzling discrepancies. The gain for PMT1 was 'tuned' by +10% (relative to MAMI gain) in order to match simulation and data for the 6 mm quartz. Likewise, the gain for PMT2 was tuned by -2% in order to match simulation and data for the 10 mm quartz. To recap, the peak PE yields were ∼52 and 101 PEs for 6 mm and 10 mm, respectively, and with ∼19% and 29% resolutions. After the swap, and using the same tuned gains, the peak PE yields are ∼47 and ∼90 PEs for 6 mm and 10 mm, respectively, and with ∼20% and 31% resolutions. The difference in the swapped resolutions are small and may be due to statistical fluctuations in the

low statistics data-set. But there are 9.6% and 10.9% discrepancies between the peak PE yields for the 6 mm and 10 mm swapped results, respectively. While the simulated and real data spectra match well for the swapped 6 mm results, the agreement is not as good for the 10 mm swapped results as the single-electron peaks are within 2σ or 10% of each other.

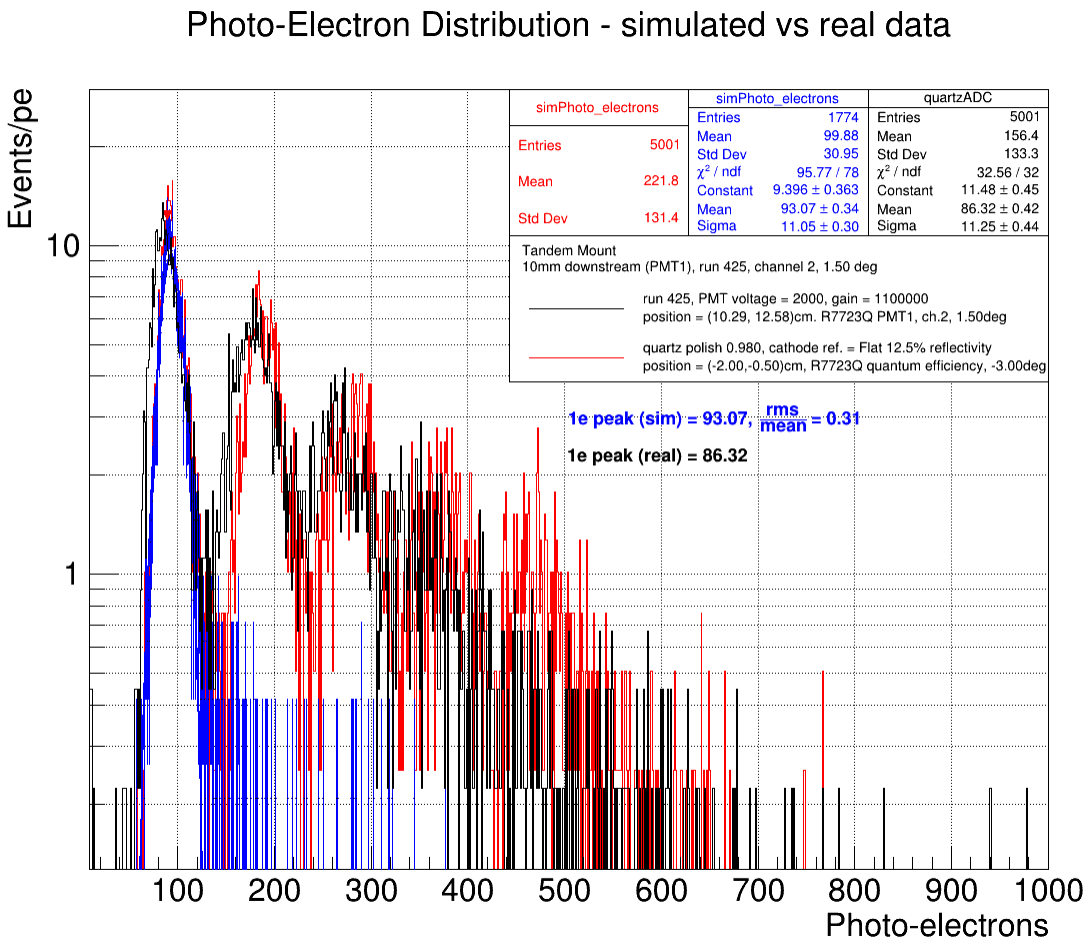

Figure 77: SLAC data and QSIM simulation for PREX-II/CREX tandem detector 10 mm thick Downstream quartz using PMT1 and perpendicular incident beam angle. Here, PMT1 was swapped for PMT2 relative to Figure 75.

There is also a clear difference between the MAMI and SLAC results for these quartz pieces, and that most likely has to do with the Kapton wrapping around the quartz. We naively thought the data should be similar to bare quartz, but it is brighter. To better understand this, a more detailed simulation of the black Kapton

wrapping was performed and compared with SLAC data as well with un-wrapped and aluminized-Mylar wrapped data from MAMI. These comparisons for 6 mm and 10 mm are shown in Figures 78 and 79, respectively, and summarized in Table 6.

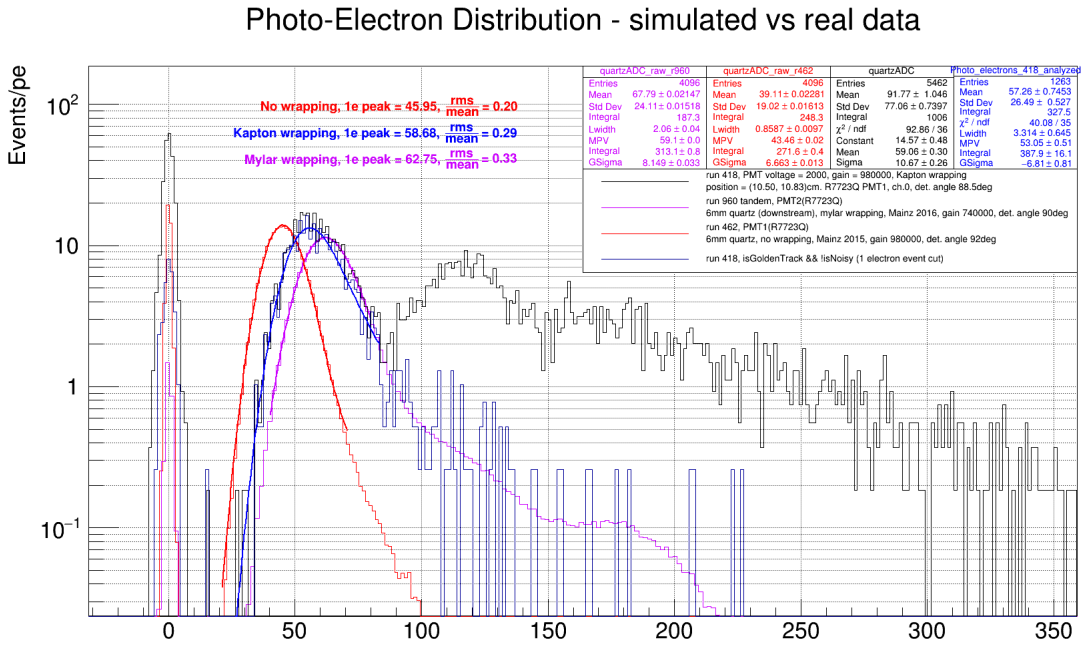

Figure 78: photoelectron distributions from SLAC (8GeV electron beam) and Mainz (885 MeV electron beam) beam tests for a 6 mm quartz piece, unwrapped (red) Kapton wrapped (blue) and reflective Mylar wrapped (violet).

Figure 79 shows data for the 10 mm thick quartz piece. In both instances, SLAC and Mainz, the same quartz and the same PMT at -2000 V was used and the beam is near 90 deg incidence on the quartz.

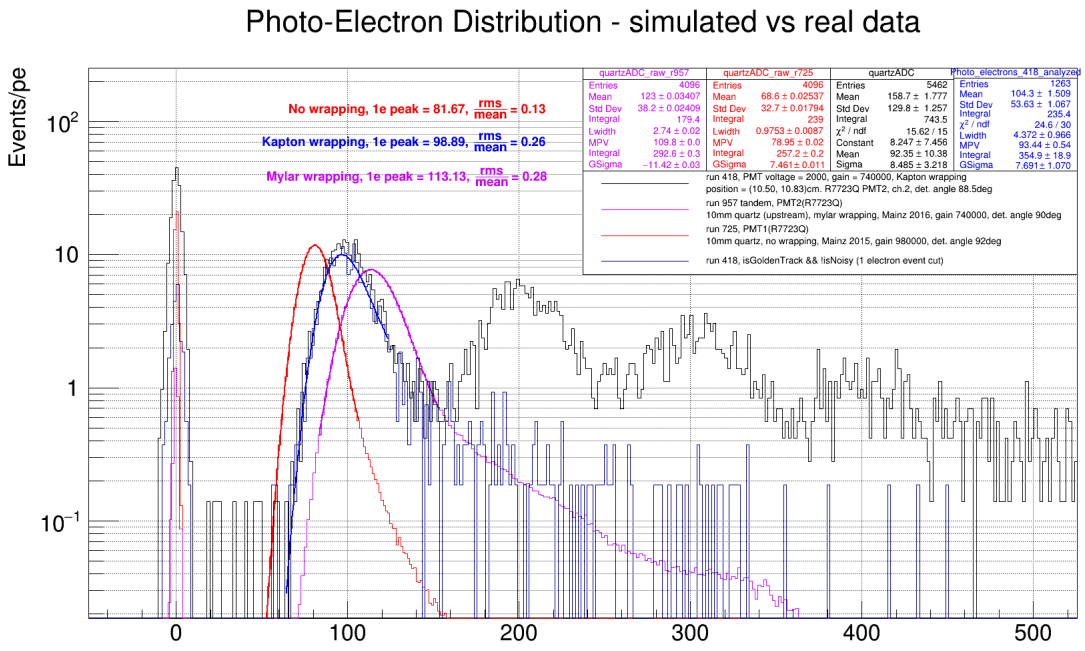

Figure 79: Photoelectron distributions from SLAC (8 GeV electron beam) and Mainz (885 MeV electron beam) beam tests for a 10 mm quartz piece, unwrapped, Kapton, and Mylar wrapped.

quartz thickness[mm]	run	position	PMT	gain [$\times 10^6$]	wrapping	Peak PE	resolution rms/mean
6	462	single	1	0.98	not used	45.95	0.20
6	418	downstream	1	0.98	Kapton	58.68	0.29
6	960	downstream	2	0.74	Mylar	62.75	0.33
10	725	single	1	0.98	not used	81.67	0.13
10	418	upstream	2	0.74	Kapton	98.89	0.26
10	957	upstream	2	0.74	Mylar	113.13	0.28

Table 6: Photoelectron yields from 6 mm and 10 mm quartz pieces, with and without Kapton or aluminized-Mylar wrapping.

The use of wrapping materials increases the photoelectron yield by $\sim 25\%$ in the case of Kapton and $\sim 37\%$ in the case of Mylar at the cost of resolution. For the PREX-II/CREX detector, the use of reflective wrapping is optional, and we will use no wrapping because that gives the best resolution. However in other applications, like the Shower-max stack detector, the quartz pieces need protection from scratches and the use of wrapping may be necessary.

4.4.2 Shower-max benchmarking Prototype Test Results

Now we are going to look at the Shower-max benchmarking prototype data and examine how they compare with simulation. As stated previously, the Shower-max detector is a sampling electromagnetic calorimeter which uses 4 alternating layers of quartz and high-purity tungsten. This quartz-tungsten sandwich is referred to as the "stack". The quartz pieces are Spectrosil 2000, 6 mm thick or 10 mm thick, with a geometry of 40 mm wide by 80 mm long and with a 45 deg bevel cut on one of the 40 mm sides. The benchmarking Shower-max detector is a small scale version of the full-scale design, but with no lightguide to complicate comparisons with simulated results, thus the name "benchmarking". These special detectors instead use a 3 inch PMT mounted directly to the top of the stack, facing the beveled end. Note that while there is no light guide, and the stack transverse dimensions are very different than the full-scale, the stack thicknesses are all identical and so the showering generation and light production are effectively the same for the benchmarking and full-scale stacks.

Two different stacks were tested: so-called 1A and 1B. Benchmarking-1A uses 10 mm thick quartz tiles and benchmarking-1B uses 6 mm thick quartz tiles. Both prototypes use 8 mm thick tungsten plates with the same length and width as the quartz. The total thickness of the stack is approximately 9.5 X_o. A 3D-printed support frame was designed to hold the stack and PMT together. A CAD schematic cross section of the benchmarking-1B prototype, with overlaid visualization for one shower event, is given in Figure 80). A CAD of the SLAC test stand with 1B prototype installed, and with event visualization, is given in Figure 81. The visualizations in these figures clearly show the electromagnetic shower production of gamma-rays (green), electrons, (red), and positrons (blue).

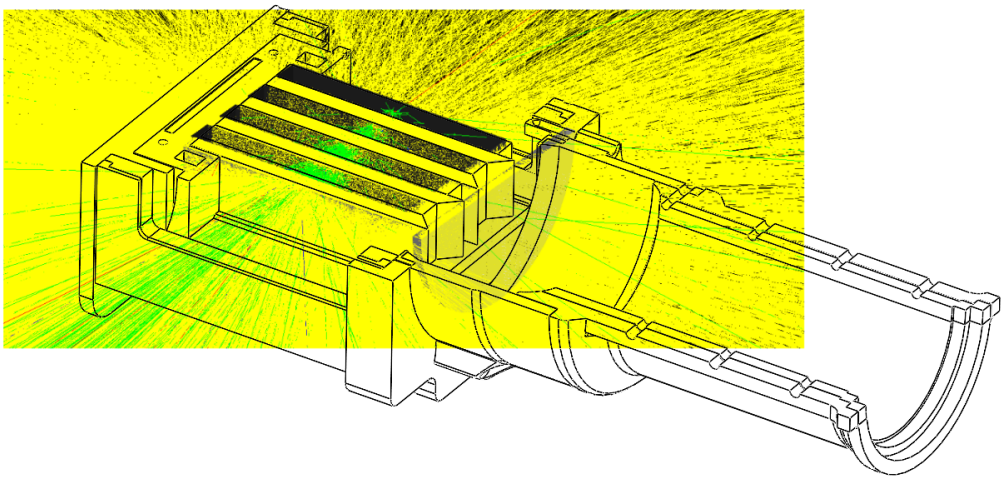

Figure 80: Benchmarking-1B prototype cross-section drawing. One simulated electron hit visualization is superimposed. The interleaved quartz (clear) and tungsten (black) can be seen. The electron enters from right to left, passing through the tungsten first to initiate the electromagnetic shower.

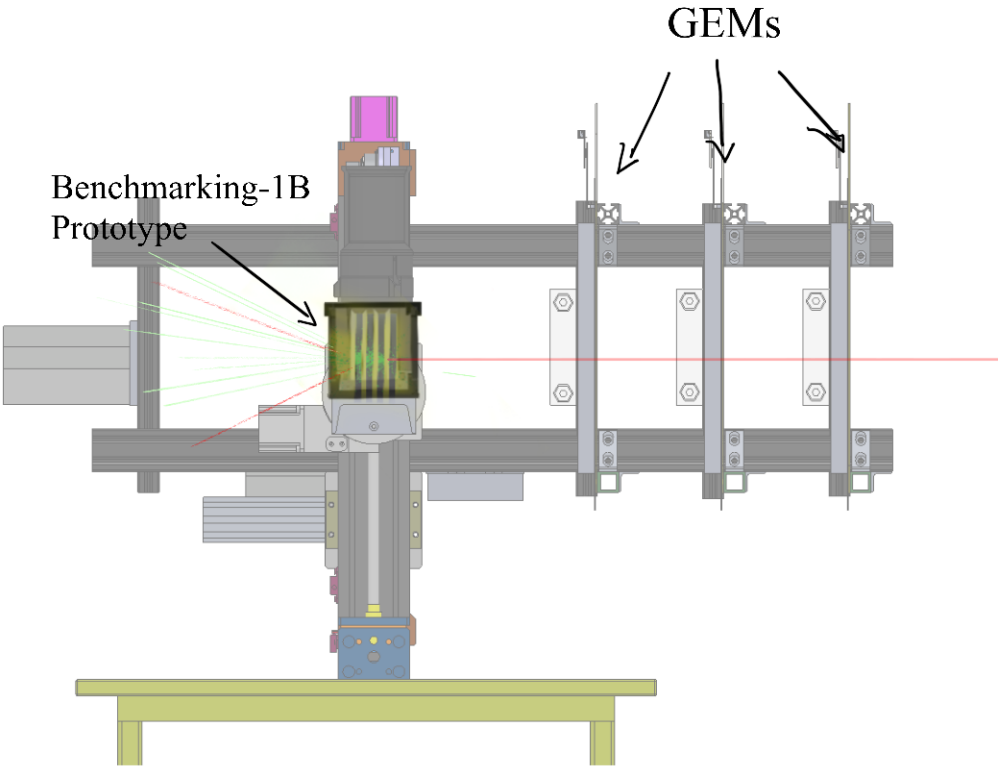

Figure 81: Visualization of one 5.5 GeV electron (red) hit at the SLAC beam test. Benchmarking prototype 1B (8 mm thick tungsten pieces, 6 mm thick quartz pieces. being hit by a 5.5 GeV electrons at the SLAC beam test.)

Figure 82 shows the photoelectron distribution of benchmarking-1A prototype with only a single piece of quartz installed. This configuration was run so that the new quartz polish parameter could be calibrated; a polish parameter of 0.94 matches the data with the simulation using measured PMT gain values. This polish is in contrast to the 0.98 found for the PREX-II/CREX quartz. These are fairly close results, perhaps within the uncertainty in PMT gain. Note that several runs were combined to improve the statistics of this result; PMT5 was used at -1200 V.

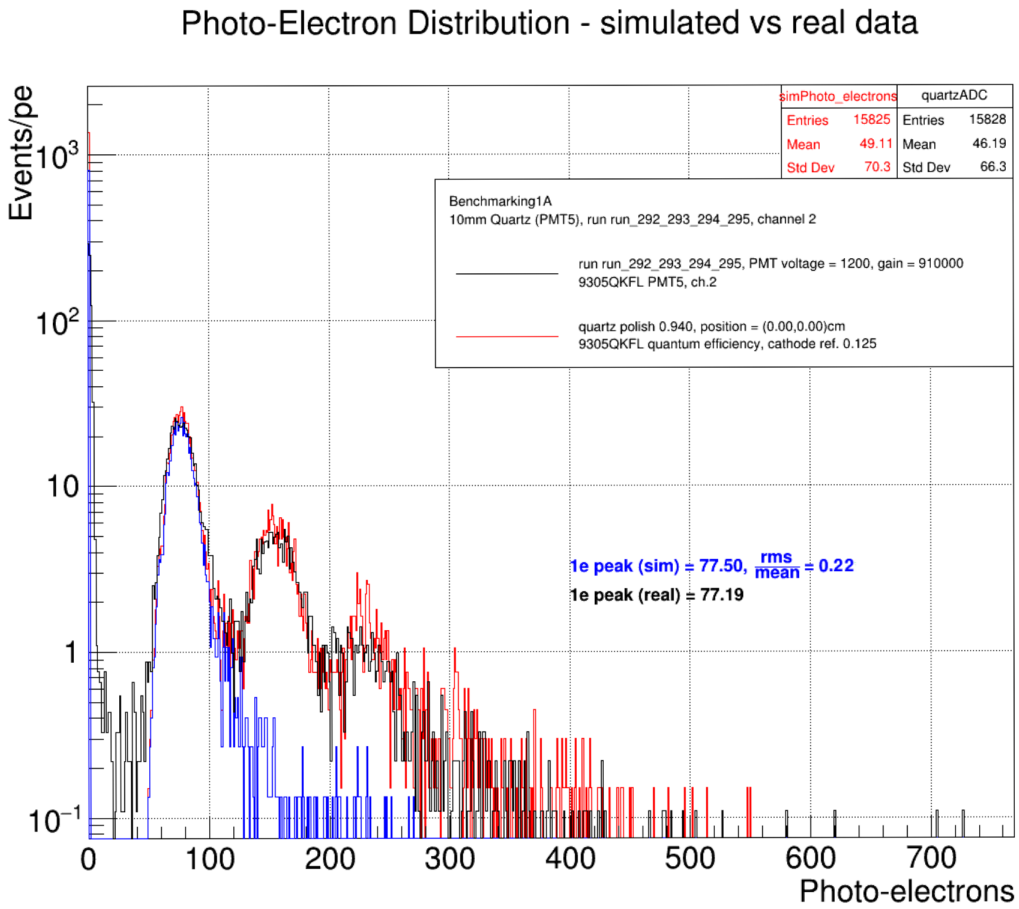

Figure 82: photoelectron distribution benchmarking-1A with only a single 10 mm thick quartz piece inside. The 3" 9305QKFL PMT is used. Notice that a polish parameter of 0.94 is used to match the data with the simulation.

The PE yield for these 10 mm thick quartz pieces are lower than for the PREX-II/CREX detector. The reason for this difference could from QE sensitivity differences between the 2" and 3" PMTs and a slightly worse polish of the quartz bar. There

is also a small geometric difference where the PMT window is not parallel with the bevel cut for the benchmarking as it is for the PREX-II/CREX detectors.

Figure 83 shows the same results but for the benchmarking-1B prototype. A polish parameter of 0.96 matches the data with the simulation. Note the same 3" PMT5 was used for both 1A and 1B prototypes.

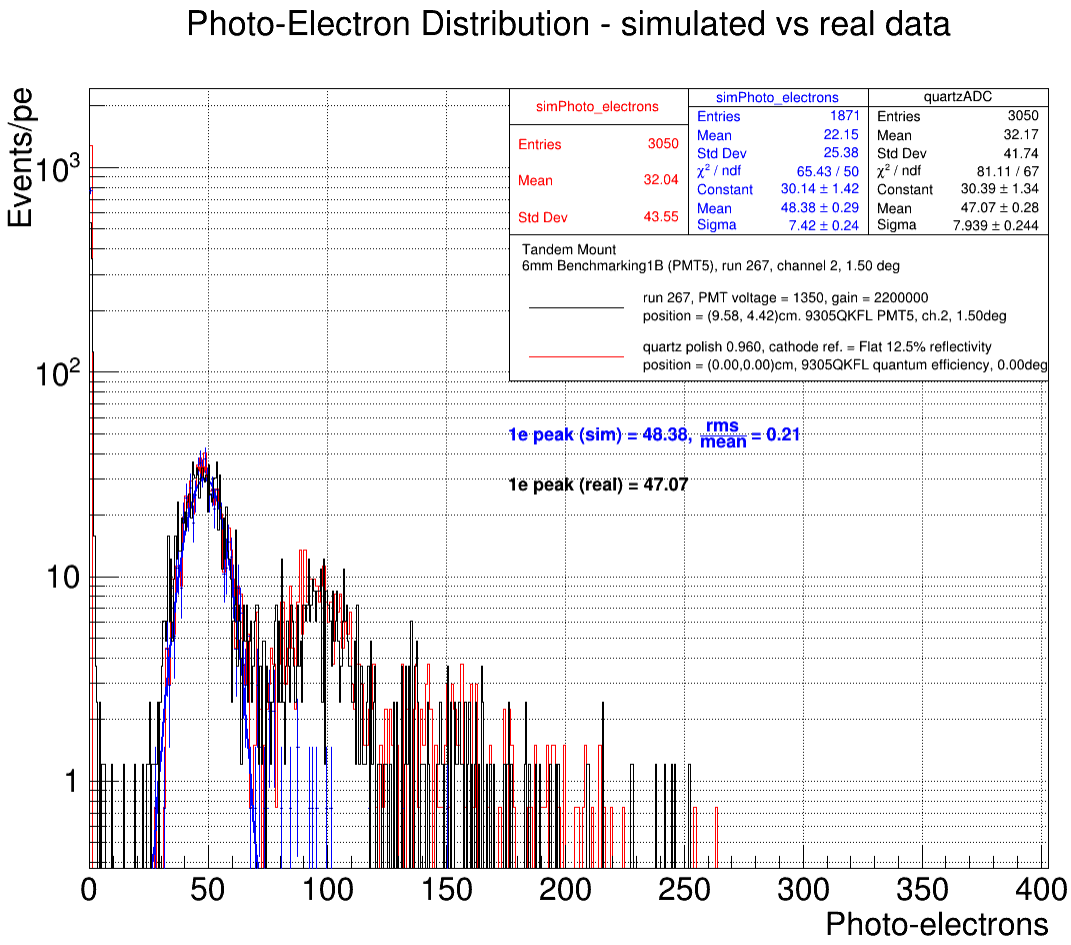

Figure 83: photoelectron distribution benchmarking-1B with only a single 10 mm thick quartz piece inside. The 3 inches diameter 9305QKFL PMT is used. Notice that a polish parameter of 0.96 is used to match the data with the simulation.

Now the following SLAC testbeam results show a progression of what happens to the Shower-max stack light yield as more layers are added, one at a time. Figure 84 shows this progression for the benchmarking-1A. The upper-left plot shows the results for 1 single layer of tungsten followed by quartz; upper-right plot shows the

yield for 2 layers; lower-left for 3 layers, and lower-right for the full, 4-layer stack. The same progression of results are shown for the benchmarking-1B prototype in Figure 85.

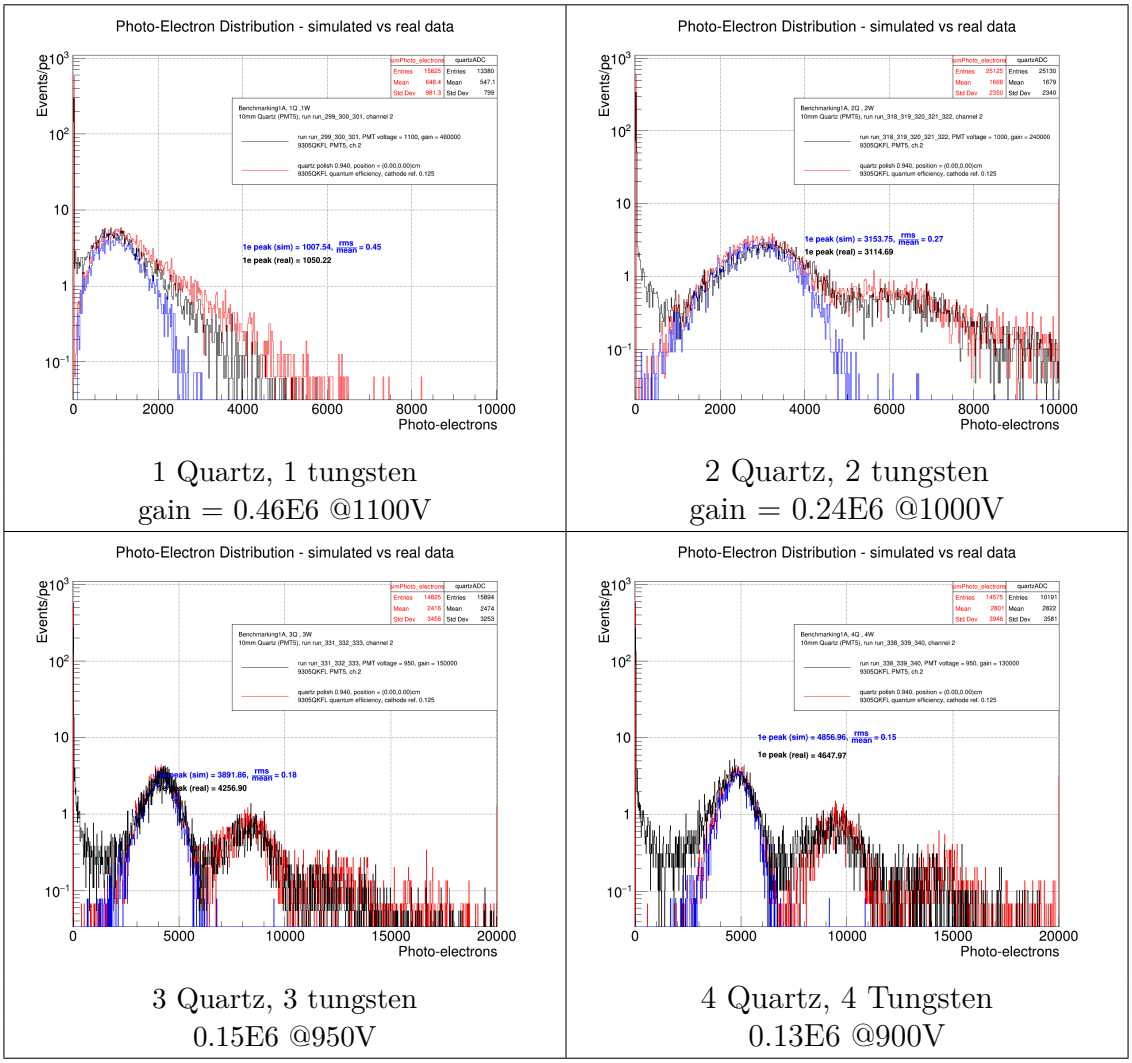

Figure 84: Benchmarking-1A photoelectron distributions (real in black and simulated in red) for a different number of quartz-tungsten pieces in the stack and different PMT voltages[V]. Polish parameter is 0.94

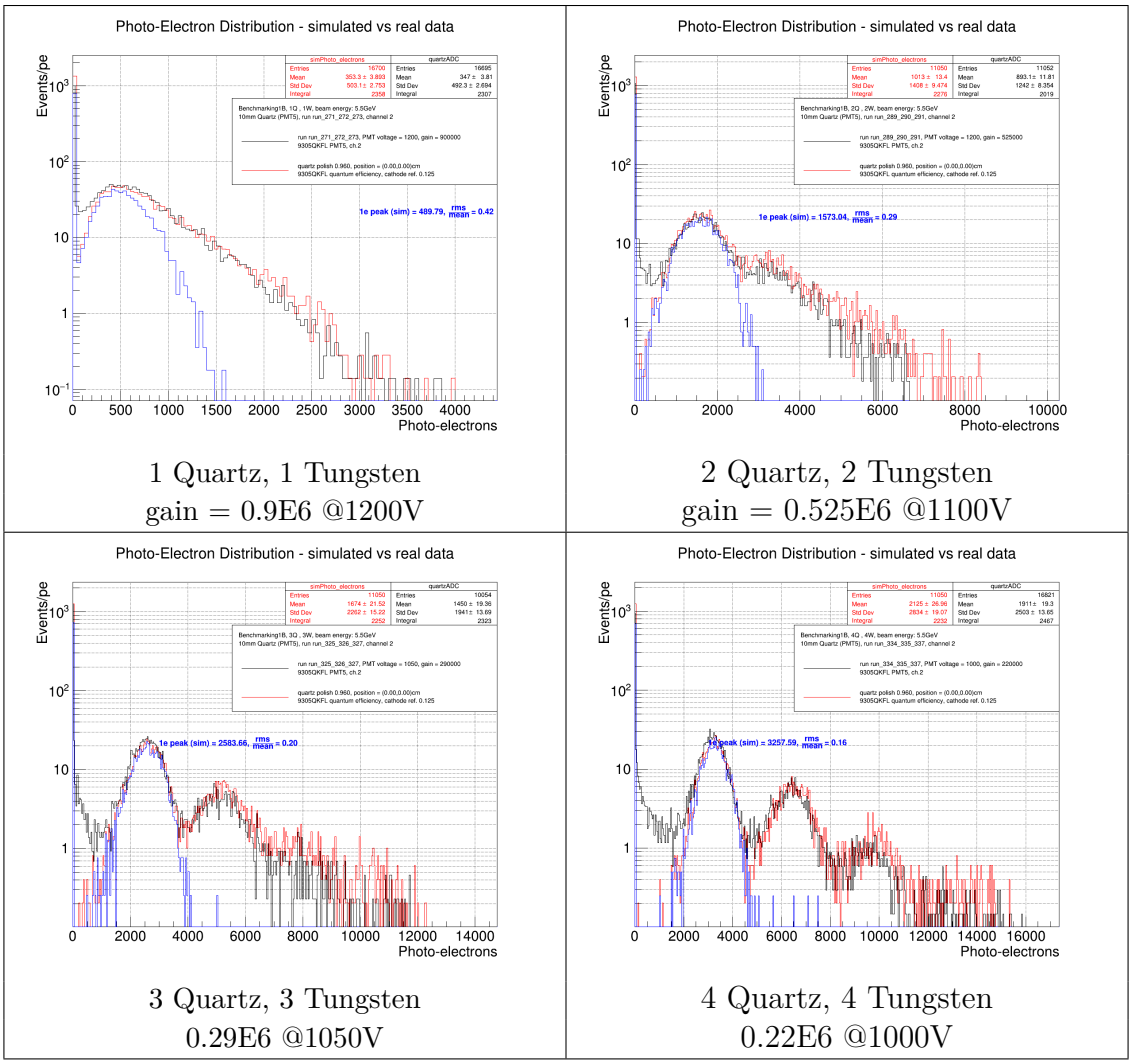

Figure 85: Benchmarking-1B photoelectron distributions (real in black and simulated in red) for a different number of quartz-tungsten pieces in the stack and different PMT voltages[V]. Polish parameter is 0.96

Notice how the detector generates an enormous amount of light (1000's of PEs), but with only one or two stack layers, the resolution is poor (30 - 45%). This is because, for an under-developed shower, there are more relative fluctuations in the number of produced showering particles. As the shower "matures" to it's maximum in size ("Shower-max"), those fluctuations become relatively small (15 - 20% for a 5.5 GeV electron). Simulation and data agree and the benchmarking prototype served its purpose as a first step toward understanding and optimizing the full-scale design.

5 Current Detector System for PREX-II/CREX

5.1 Consideration of Quartz Thickness and PMT Linearity

The detectors and corresponding electronics used in PVeS experiments should show a very linear signal response to the Cerenkov light levels on the photocathode during integration mode. In particular, these highly linear responses should lead to a highly linear asymmetry measurement. Any deviation from linear response behavior will induce a potential non-linearity in the value of the measured asymmetry. The measured A_{PV} should remain constant, independent of the overall photocathode light level or PE current during the measurement. To achieve this operational requirement of the detectors, they must have an appropriate high voltage setting for particular photocathode light levels. The summary finding here is that the photocathode (PE) current should be less than $\sim$15 pA and the PMT anode current should be in the range of 20 - 30 μA. Following these guidelines should ensure a low detector non-linearity contribution to the systematic error.

In order to explain "non-linearity" in the context of PVeS experiments, the technique for quantifying the non-linearity should be described briefly: The PMT is illuminated by two LEDs, one is set to a constant brightness (light level), and the other flashes at a specific helicity reversal or 'flip' frequency (30, 120, or 240 Hz); the integrating DAQ is synchronized with the flashing LED–which mimics the physics asymmetry signal. In this way, the test PMT measures an asymmetry,

$$A_{LED} = \frac{N^+ - N^-}{N^+ + N^-}, \tag{28}$$

where N^+ and N^- are the signal size from the PMT when the flashing LED is ON and OFF, respectively. Now we can approximate the asymmetry by

$$A_{LED} = A_{true}(1 + \beta N_{avg}), \tag{29}$$

where the measured asymmetry, A_{LED}, is equal to the true value, A_{true}, when the average signal brightness, N_{avg}, approaches zero. The above expression represents the standard way to parameterize the PMT non-linearity for PVeS experiments into a single, linear coefficient, β. βA_{true} represents the slope of a plot of A_{LED} as a function of N_{avg}, and the difference between A_{true} (the y-intercept) and $\beta A_{true} N_{avg}$, at the maximum N_{avg}, gives the amount of deviation from linear response behavior.

Various N_{avg} values can be obtained using a set of filters placed in between the LEDs and PMT. In principle, the asymmetry is independent of filter setting except for any non-linear response of the PMT. The non-linearity is also studied at various light levels or photocathode current, PMT high voltage and pre-amplifier setting in order to fully characterize the PMT non-linearity and find the optimal operational setup: light level and HV setting.

As mentioned before, the quartz thickness is the single parameter that determines the statistical error when integrating the signal. If the quartz is too thin, there are too few photoelectrons detected and the photoelectron distribution width would increase. If the quartz is too thick, the electrons create a long Landau (delta-ray) tail, which increases the width. We want to find a thickness that compromises between these two extremes and gives an adequate brightness (light level) that keeps the PMT's non-linearity close to zero. Note that the light level depends on the product of the quartz PE yield and the rate of detected scattered electrons. A thicker quartz tile could yield too much light for optimal linearity if the detection rate is high. Likewise, too low of a high voltage also causes PMT instability and leads to increased non-linearity. A sample of the type of data collected for the PMT non-linearity assessment is shown in Figure 86.

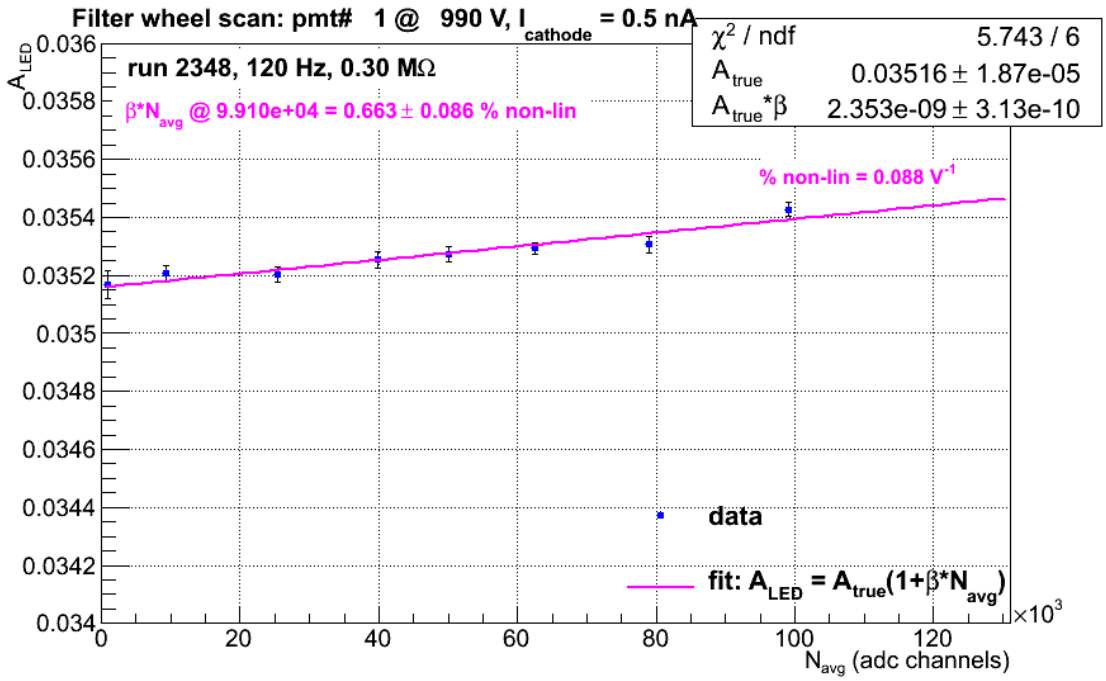

Figure 86: PMT1's non-linearity measurement at 990V and $I_{cathode} = 0.5$ nA. The measurement is done for each of the PMTs that are going to be used during the experiment. Study made by Devi Adhikari.

This sample non-linearity data was collected for PMT1 at 990 V with a 0.5 nA photocathode current (avg light level with no filter) and at 120 Hz flash rate. The y-axis is the measured asymmetry, A_{LED}, and the x-axis is the average signal level (in ADC channels using 18-bit Q_{weak} integrating ADC) for 8 different filter settings. The fit is the linear parametrization of Equation 29 with the fit parameters (y-intercept and slope) given in the plot's stat-box. The result for this particular data sample is that we should expect $\sim 0.66 \pm 0.09\%$ non-linearity (systematic error) in our asymmetry measurement from PMT1 if we used these settings. In order to tune the photocathode light level during the experiment, a study of quartz PE yields and resolution as a function of thickness was performed.

5.2 Quartz Thickness Study for PREX-II/CREX Tandem Mount Detector

Given the level of agreement achieved between simulation and testbeam data using QSIM, it was ready to be used to study the PE yield distributions for different quartz thicknesses. Summary results from this study, for the downstream quartz, are given in Figures 87 and 88. The simulation indicates that the number of peak PEs increases linearly with the quartz thickness and is ∼independent of the upstream quartz thickness. The resolution gets better with increasing downstream thickness and decreasing upstream quartz thickness.

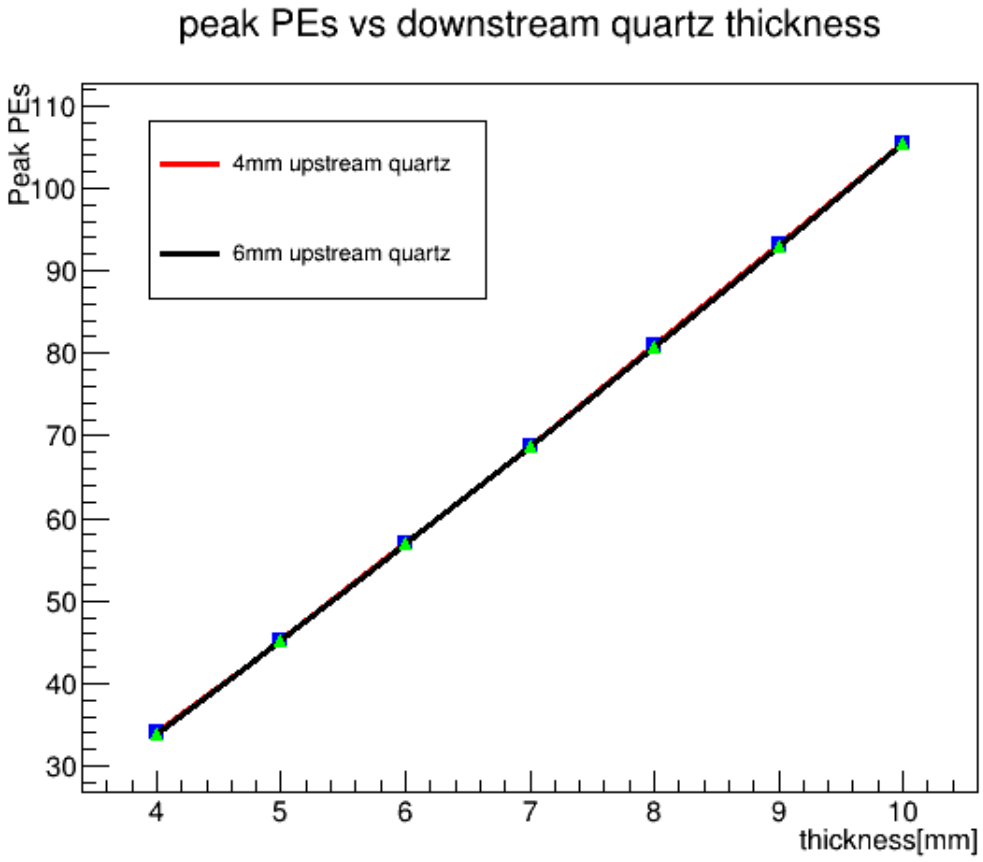

Figure 87: Peak PE yields as a function of different quartz thicknesses for the downstream piece. Note the upstream quartz thickness is set to 4 mm (red line) and 6 mm (black line). Thee two lines are directly on top of each another, indicating very little dependence of thee "peak" yield on the upstream quartz thickness.

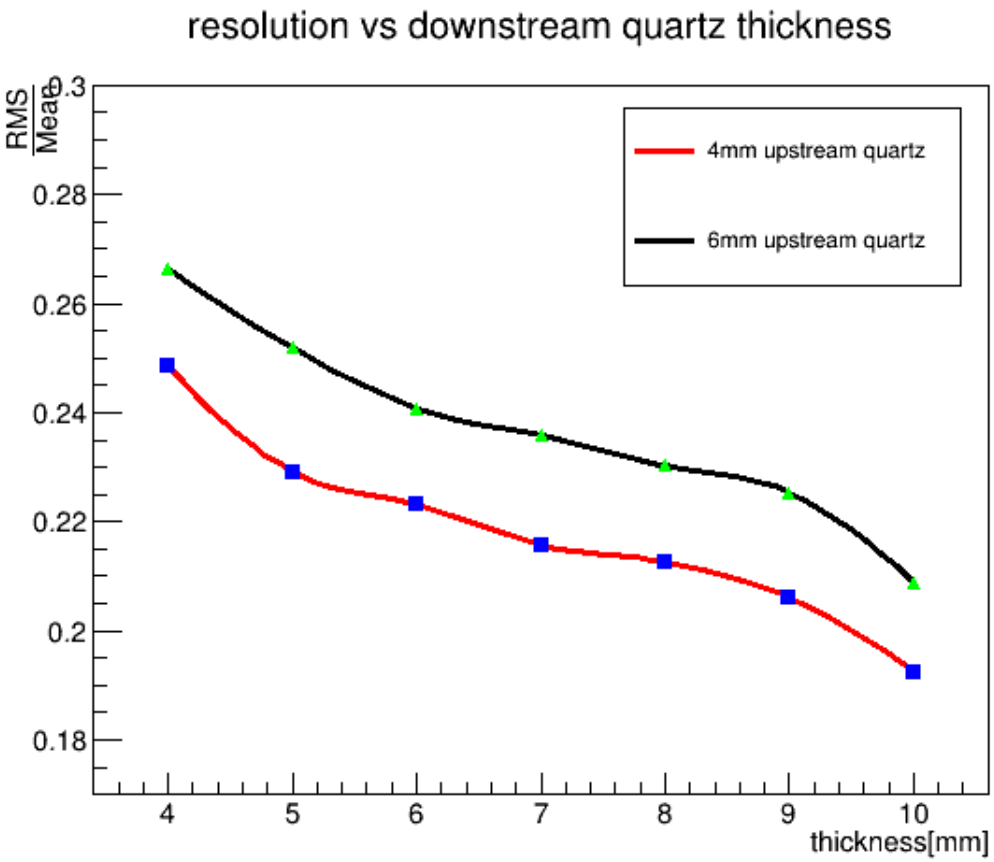

Figure 88: Downstream quartz resolution, $RMS/mean$, as function of the thickness, having a $4mm$ and $6mm$ thick quartz upstream the beam.

During the 2015 and 2016 beam test, 6 mm and 10 mm quartz pieces were used–giving acceptable resolutions at the 20 - 30% level depending on configuration. But, the light output at these thicknesses, according to more recent linearity measurements, is too bright for the ∼2 GHz of expected flux rate. Therefore, thinner 5 mm thick quartz pieces will be used for the PREX-II/CREX tandem detector–for both upstream and downstream positions. Figure 89 shows the predicted PE distributions for this 5 mm quartz configuration. This quartz thickness allows the PMT to operate at the edge, but within the optimal regime in terms of photocathode current for best linearity. With ∼44 peak PE's per electron and 2 GHz of electrons, the photocathode current is ∼14 nA. It has been found that operating the PMT around 600 V for this light level gives a PMT gain that provides an optimal anode current of ∼28 μA (this implies the PMT gain is around 2000 at 600 V which is what we find). The typical

PMT non-linearity systematic error for this setup is below 0.5%±0.3%.

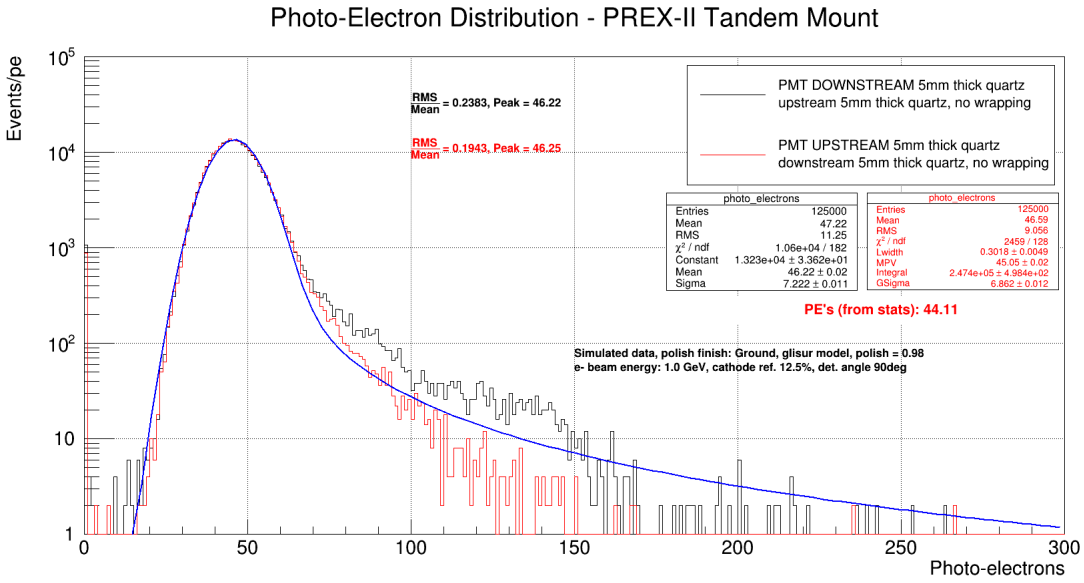

Figure 89: Simulated PE distributions (upstream and downstream) for 5 mm thick quartz for the PREX-II/CREX tandem detector. The Red histogram is for the upstream while the black histogram is for the downstream (note the extra high-light tail and worse resolution, but same exact peak PE's. The blue curve is a Landau-Gaussian (LanGau) convoluted fit to the upstream distributions. While this fit captures the photo-peak and beginning of the tail, it does not properly model the sharp cutoff of the high-light tail.

Figures 90 and 91 show the angle dependence on the peak PE yield and overall detector resolution (RMS/Mean) for the 5 mm thick quartz, both upstream and downstream. Since the orientation of the quartz will be tuned to be normal to the incoming flux, our anticipated detector resolution is at the 20% level, which will induce very minimal, less than 1%, excess noise in the asymmetry measurement.

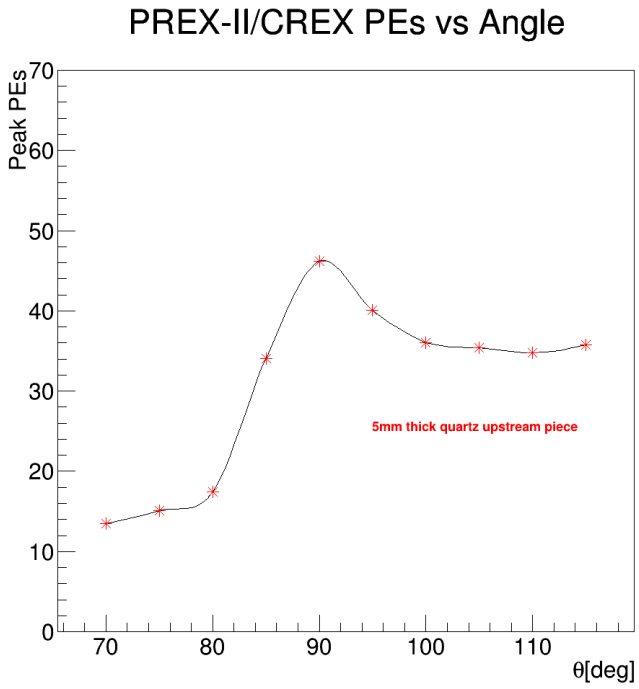

Figure 90: Angle dependency of the peak PE signal of the PREX-II/CREX detector with 5 mm thick quartz pieces (upstream).

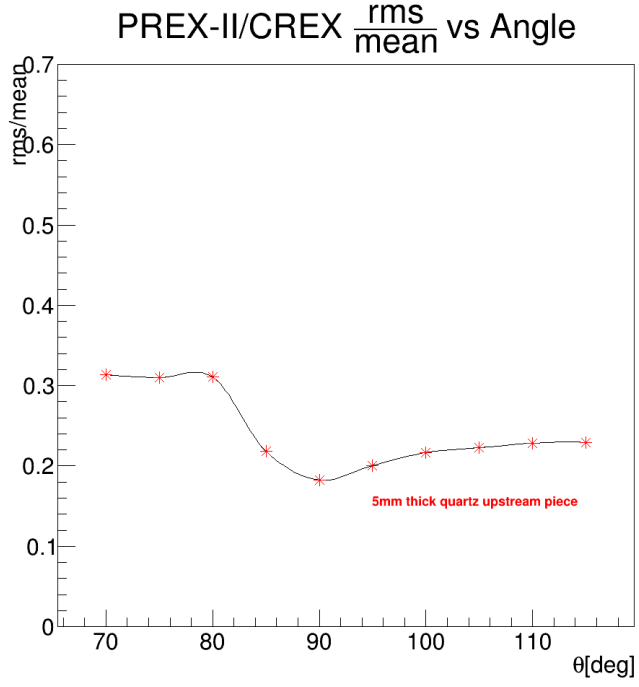

Figure 91: Angle dependence of the resolution, $RMS/mean$, of the PREX-II/CREX detector with 5 mm thick quartz pieces (upstream).

5.3 Final Detector Focal Plane Package

The detector package for both, Left and Right, Hall A High Resolution Spectrometers (LHRS and RHRS) focal planes each consist of a tandem detector assembly, a system of three GEM trackers, and associated electronics and motion system. The motion system for each arm consists of one 5 inch and one 15 inch long linear Velvex slider and a rotary stage (all remotely controlled). The Left and Right focal plane packages have mirror symmetry, as required to efficiently run parity violation experiments. Thus, two sets of all components, a left-handed and right-handed (mirror-symmetric) version, have been designed and prepared. The RHRS tandem detector CAD is shown in Figure 92. Note that the quartz light tight, 3D-printed ABS plastic covers, with black Kapton windows are only shown in the upper left-hand picture in the upstream position. The entire package assembly with GEMs and motion system is shown Figure 93.

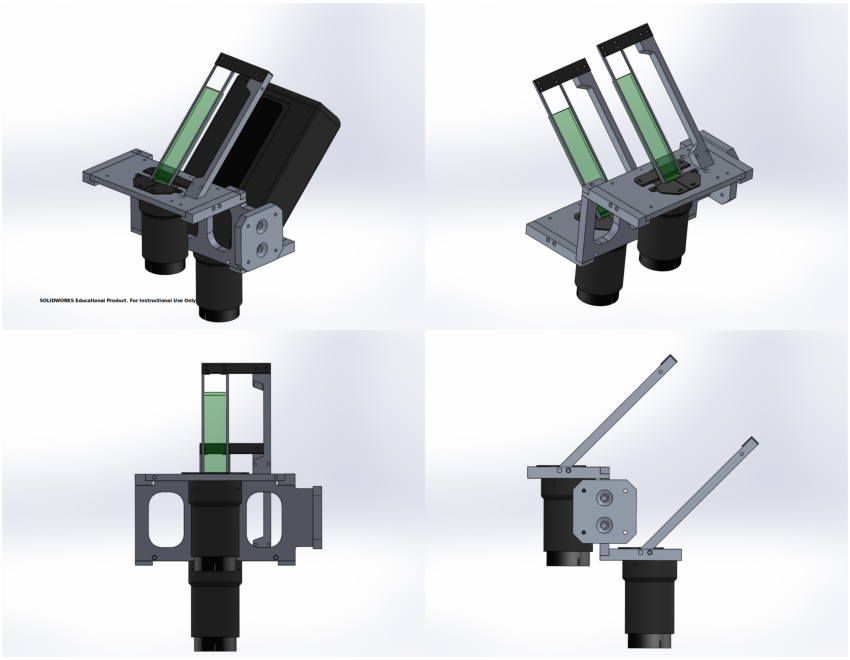

Figure 92: Various CAD views of the thin quartz, integrating tandem detector for PREX-II/CREX. The design uses machined aluminum and 3D printed ABS plastic. The quartz is shown as green for visual clarity.

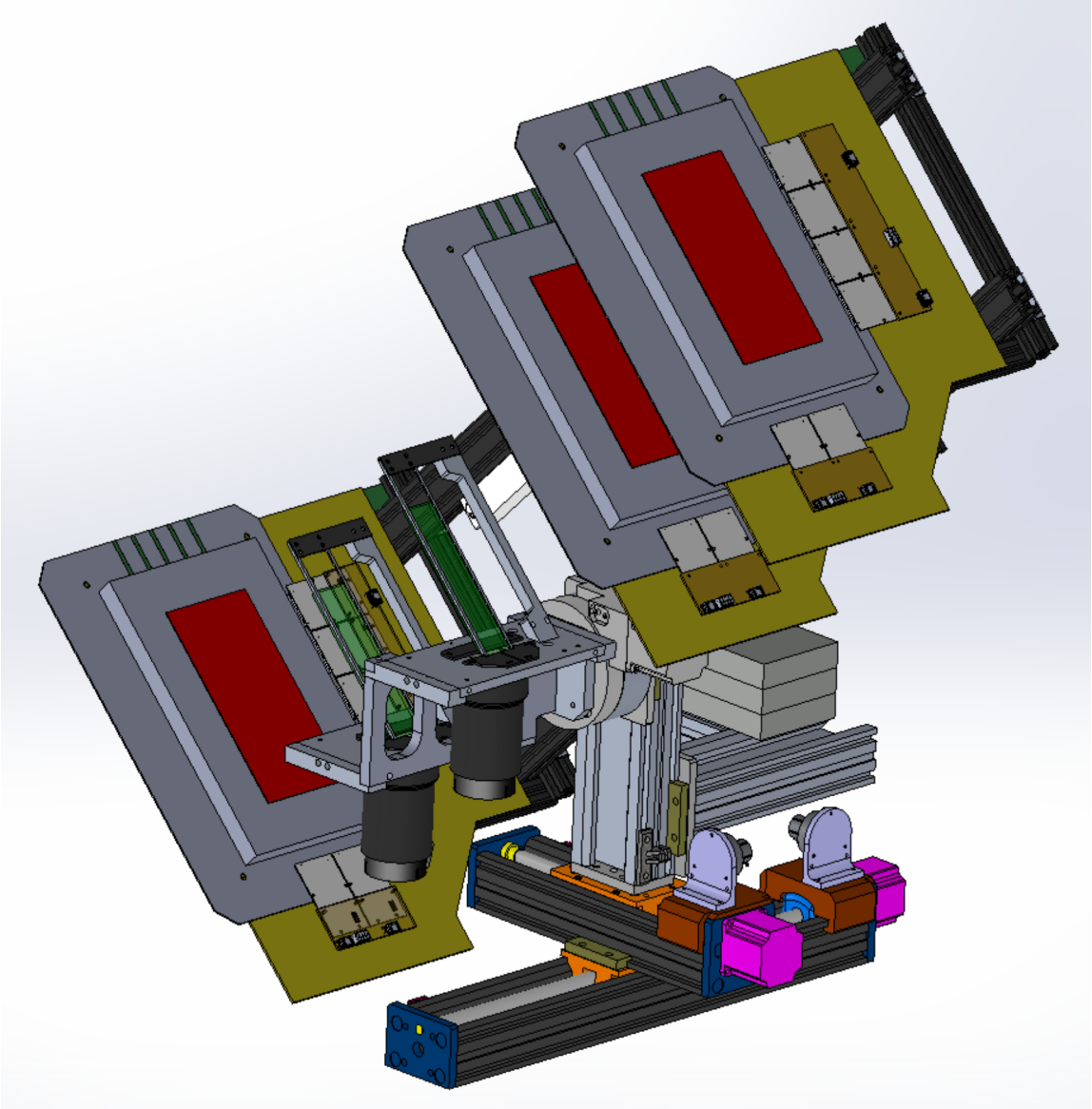

Figure 93: PREX-II/CREX RHRS detector package CAD. Many details are present, including rough outlines of the GEM electronics, the linear position transducers (light purple-colored sitting atop the linear sliders near the motors), and counter weight assembly. All details needed to be included in order to balance the package and ensure weight and torque tolerances of the sliders were not exceeded. The primary framing component is series-10 extruded aluminum.

As mentioned previously, a tandem design, with two independent detectors, was chosen for the sake of redundancy (insurance) and to check the other detector's result. A difference in the asymmetry widths between the upstream and downstream detectors would indicate some problem with the spectrometer, beam and/or target.

Also if for some reason one of the PMTs fails during the experiment, the other will continue taking data until a replacement is arranged.

A detector package is placed within the focal plane of each HRS, which are positioned to accept ±5 degree scattered particles and transport the negatively charged ones, with momentum near the beam energy (elastic), to the focal plane. The focal plane resides within a two story shielded bunker made of concrete and steel (called the detector hut). The purpose of the hut, which is three stories above the scattering plane (beam line), is to shield the sensitive detectors and electronics from Hall radiation and backgrounds during the experiment. The hut has two massive doors that allow access inside. The HRSs typically have a wide array of particle detectors pre-installed in the focal plane, but these are all removed for PREX-II/CREX, except for the Vertical Drift Chamber (VDC) tracking system. The focal plane chassis is also on a roller system (or cart) that allows the entire assembly to be pulled out of the hut for installation and maintenance.

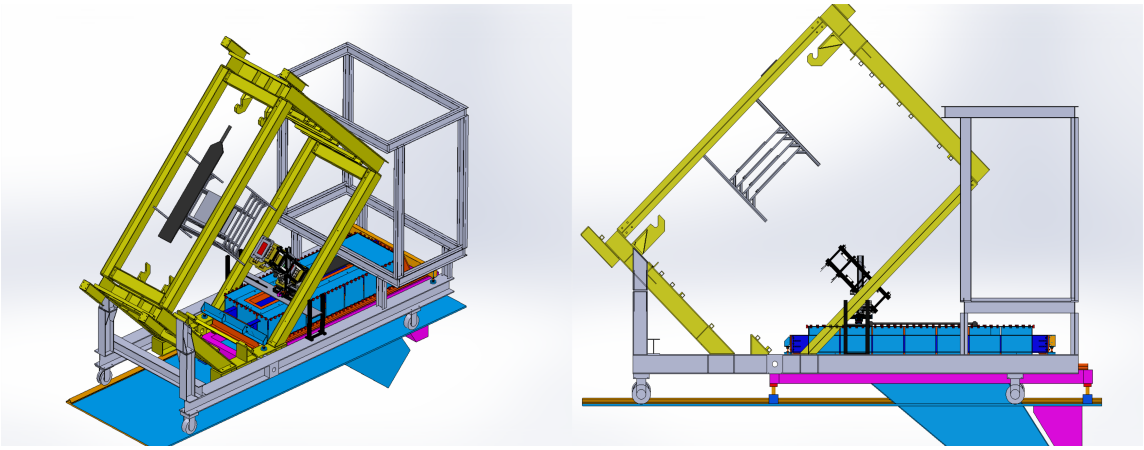

Figure 94: CAD drawing of the I-beam framing system for the HRS spectrometers. The PREX-II/CREX detector package is seen installed just above the blue VDC box near the bottom yellow I-beam. Also shown are various trigger scintillator paddles.

The HRS focal plane chassis consists of an I-beam frame system as shown in the CAD schematic of Figure 94. The grey I-beam frame supports the electronics equipment (Racks, crates, ADCs, HV power supplies, NIM electronics, etc.), and the yellow I-beam frame, tilted at 45 deg, holds detectors such that their sensitive surfaces

are normal to the transported flux passed into the hut from below. A photograph of the focal plane detector cart, pulled out from the hut during the PREX-II detector package installation, is given in Figure 95. Figure 96 gives an overall side-view of the main features of Hall A, including the HRS and relative location of the focal plane package.

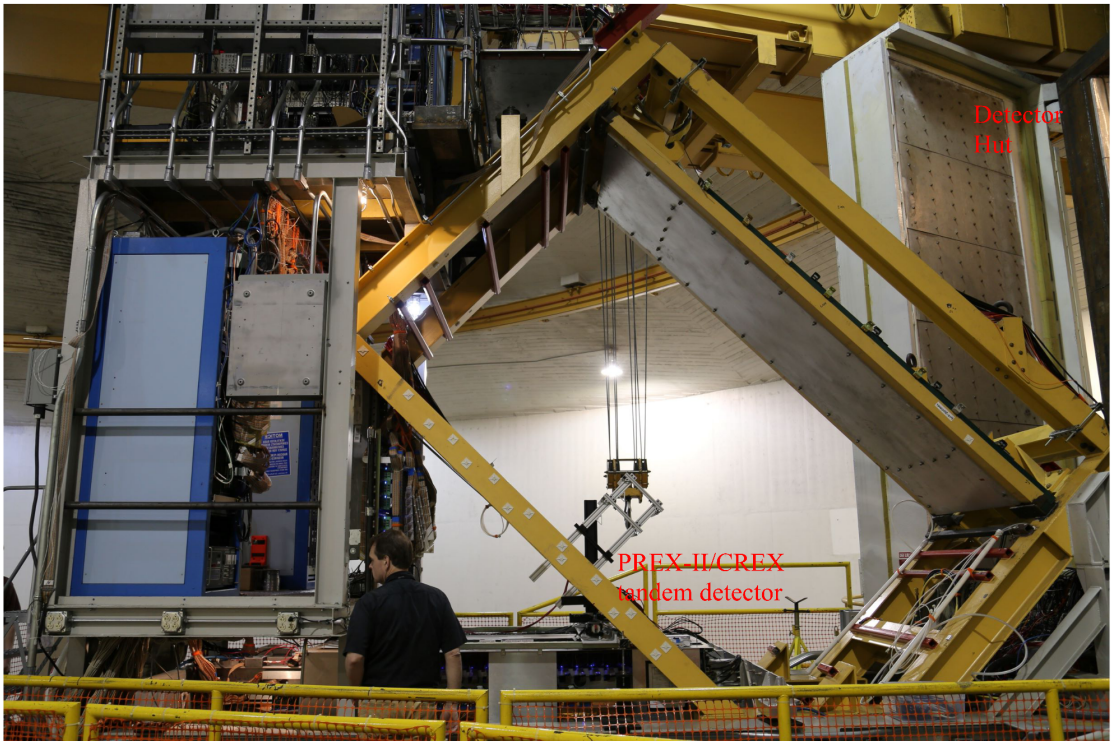

Figure 95: Side view of the RHRS detector cart pulled out from its shielded hut during PREX-II installation. The PREX-II/CREX detector package extruded aluminum framing can be seen installed near the bottom yellow I-beam. A Hall A technician is standing in front for perspective. Also seen are the two stories of electronics racks supporting the detectors.

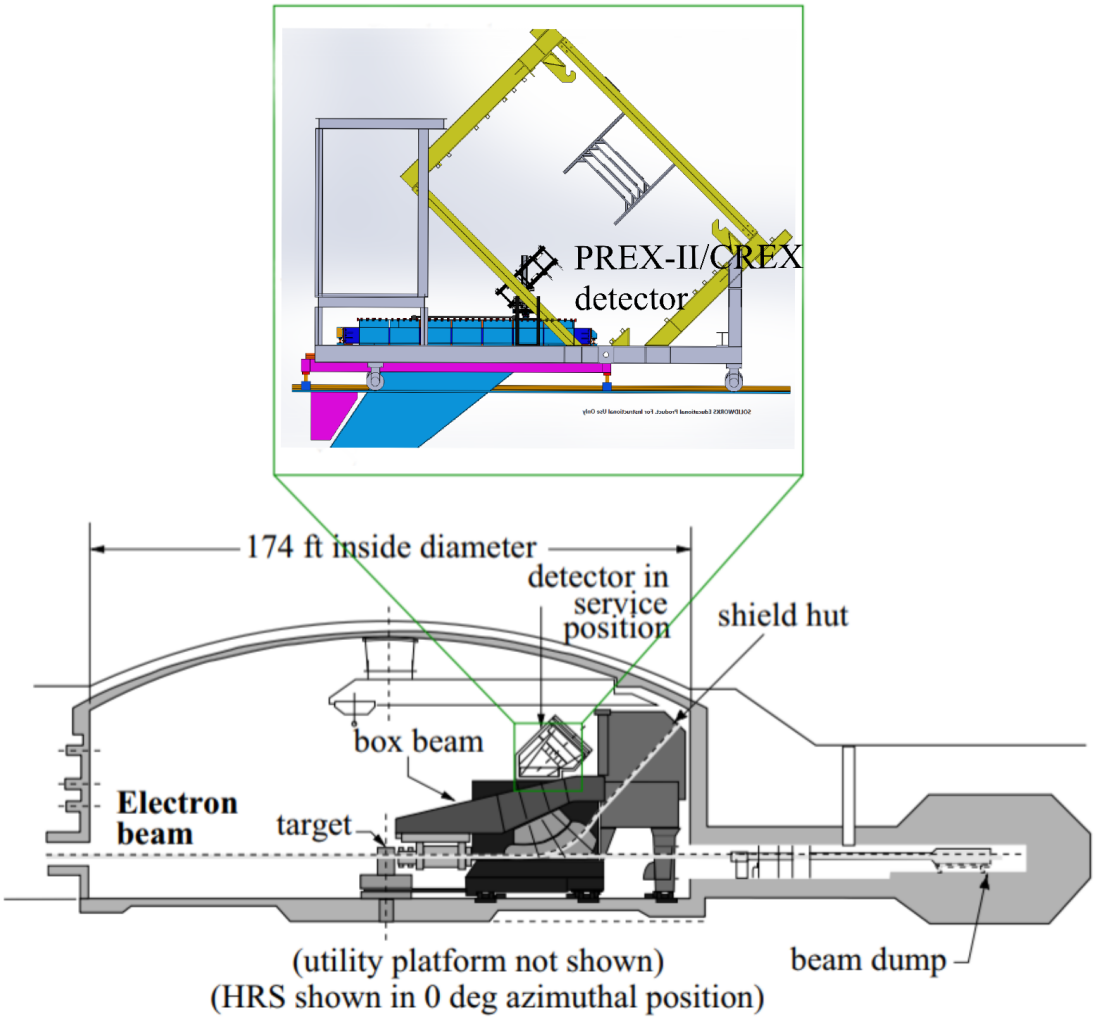

Figure 96: Overall position of the PREX-II/CREX detector inside the Hall A at JLab. Dashed line represents the electron beam and transported flux to shielded hut.

A side view of the LHRS, showing the elastic peak (nominal) flux-ray, together with an event visualization, is given in Figure 96. A photo of the LHRS package installed in the focal plane is given in Figure 98. Recall that the final configuration uses unwrapped 5 mm thick quartz tiles which are 16 cm long and 3.5 cm wide. The elastic plus radiative-tail part of the signal, up to the first inelastic state (which represents a 2.6 MeV loss in energy), is passed through both quartz tiles for each arm by taking advantage of the high resolution capability of the spectrometer. The precision alignment is achieved using the detector package motion system.

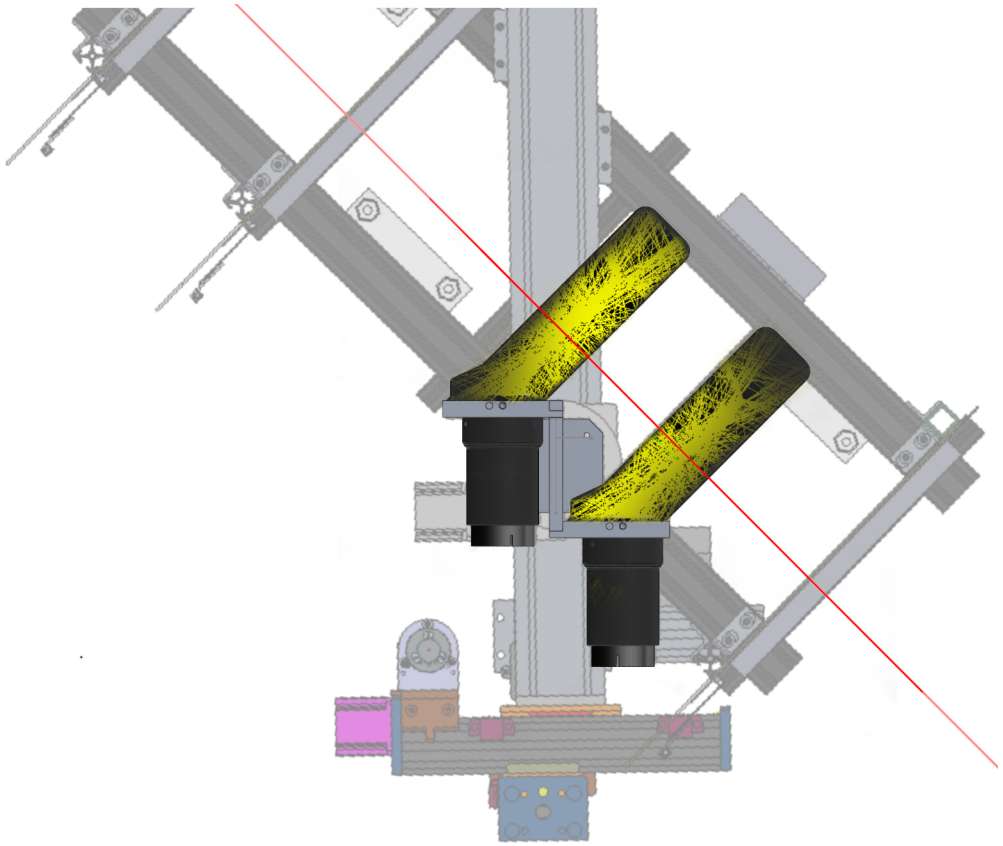

Figure 97: Side-view of the PREX-II/CREX LHRS detector package CAD together with QSIM visualization of a single electron event. The nominal scattered flux peak trajectory is shown as a red line passing from bottom to top through the tandem quartz and GEMs;the generated Cerenkov light is shown as yellow.

The motion system for each arm includes two linear sliders and a rotary stage, giving $\hat{x}, \hat{y}$, and $\hat{\theta}$ degrees of freedom. Only the tandem detector has the $\hat{\theta}$ motion, as the GEM orientation is fixed, however the entire assembly can move in $\hat{x}$ and $\hat{y}$. Their movement is controlled remotely with a GUI interface. The linear stages have position transducers to provide position feedback and the rotary stage is equipped with an encoder.

One final key detail is that the intercepted elastic flux envelope fills the entire width of the quartz, but is only $\sim$8.5 cm long. This implies that the remaining 7.5 cm of quartz length acts only as a total internal reflection based lightguide–to funnel the Cerenkov light to the PMT window.

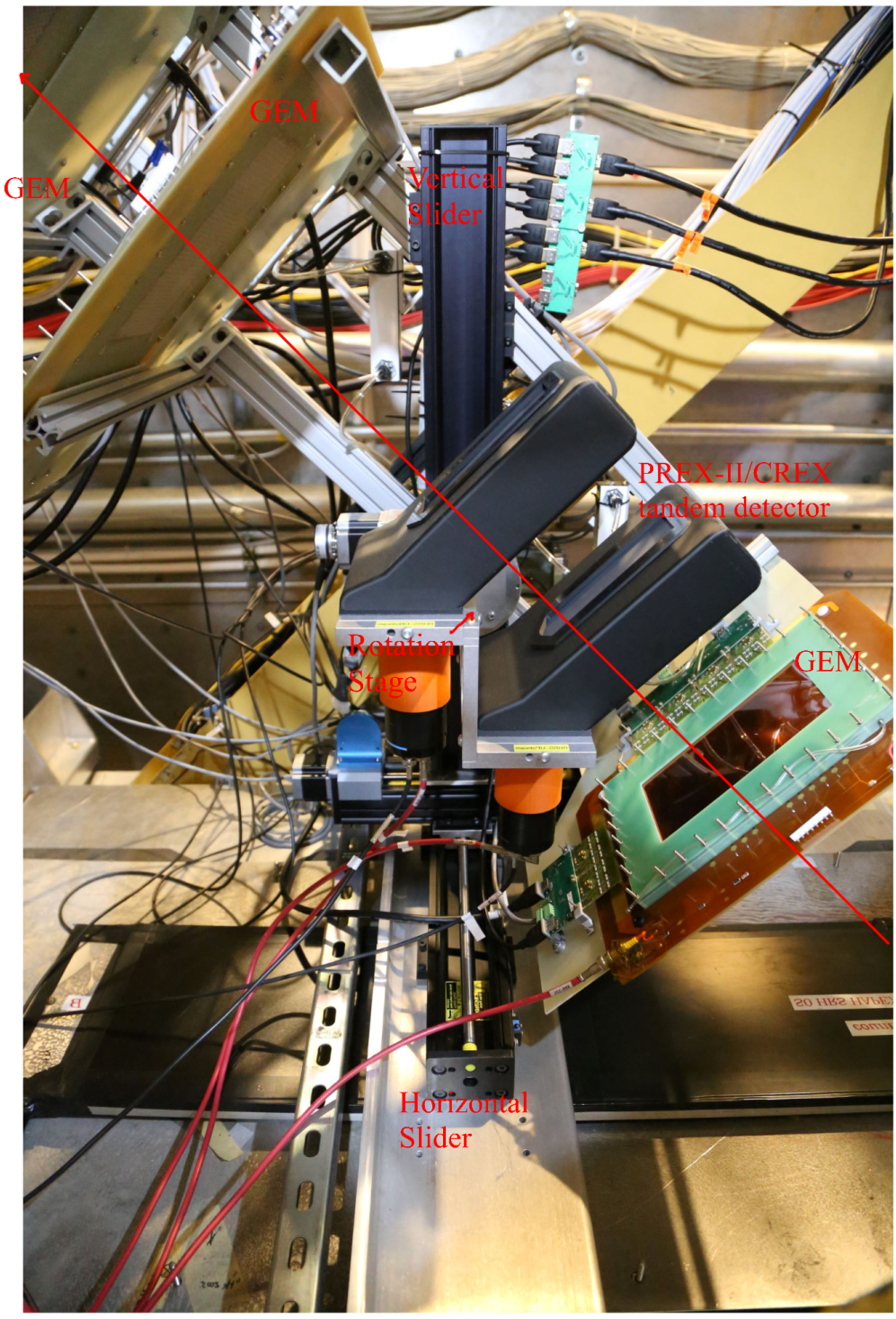

Figure 98: Photograph of the LHRS PREX-II/CREX main detector package installed in the focal plane.

6 Conclusions

An optimized design for the PREX-II and CREX thin quartz Cerenkov detectors has been rigorously developed using successive testbeam and simulation studies. A new, powerful simulation tool, QSIM, developed over the past five years, has reached an impressive state–capable of reproducing real data distributions for any detector scenario. The development of the PREX-II/CREX detector at Idaho State represents a great leap forward, with respect to the previous generation of these detectors, with two times more light output and 40% better resolution. In June 2019, the PREX-II/CREX detector packages were installed and commissioned at Jefferson Lab, and they have now been successfully used to probe the neutron distribution in ^{208}Pb nuclei. In addition to providing rich nuclear structure information, a precise measurement of the neutron radius will pin down the density dependence of the symmetry energy of neutron-rich nuclear matter, which has broad impacts for neutron star structure[38], heavy-ion collisions, and future atomic parity violation experiments[39]. The same focal plane detector package will be used to probe the neutron distribution in ^{48}Ca nuclei starting in December 2019. As highlighted throughout this work, the successful development of the PREX-II/CREX detector package required the joint efforts of faculty and students from Idaho State University and other institutions.

In addition to designing, constructing, testing, and delivering the PREX-II/CREX detector packages, the ISU parity group has also developed several other parity-violating quartz Cerenkov-based detector systems. Most notably are the SAMs and the Shower-max detector. The Small Angle Monitors received a significant overhaul as their lightguide geometry and quartz radiator size were optimized. Another new design feature, including a pre-radiator with the SAMs, was also carefully studied with testbeam and simulation, but not implemented due to excessive radiation load on the experimental hall. The new SAMs have operated successfully in Hall A since they were first installed in late 2015 and commissioned in spring 2016. Their performance parameters, PE yield, and resolution are known from testbeam data matched to simulation, and they will continue to be useful tools in future parity violation experiments

at Hall A in JLab. The benchmarking shower-max prototype for MOLLER had a successful debut at the SLAC End Station Test Beam facility in late 2018. These tests validated the baseline design for the shower-max detector and will pave the way for future development of the final design.

The development of the Geant4 optical Monte Carlo quartz simulation, QSIM, has been an invaluable tool as we push to understand the performance and design optimization of our detectors. QSIM has the flexibility to accommodate multiple detector geometries and incident beam characteristics (from cosmic-ray to pin-point beams). In the pursuit to fully understand real data distributions, we were forced to study and incorporate the optical properties of all design components into the simulation. Besides the quartz radiator (dispersion, attenuation, and polish), the optical properties of the PMT have been crucial to incorporate in order to fully match real data and simulation and to give confidence in PE yields.

To match simulation to real data (precisely), several parameters need to be included in QSIM: light refraction indexes and attenuation in quartz, reflection coefficients of wrapping materials, and specific optical properties of the photocathode (QE and reflectivity) and quartz PMT window. The accurate definition of these parameters is crucial for a realistic simulation of the transit of Cerenkov photons from their creation, inside the quartz tile, to their multiple internal reflections inside the tile, to attenuation and reflections inside the quartz PMT window and their absorption or reflection in the photocathode. We get these parameters from available literature and verify their correct implementation, one by one, by comparing simulation outputs with literature.

It turns out that many of the optical properties needed are quite well defined in the literature (even the typical photocathode reflectivity of 12.5%). After all known optical surface parameters are implemented, the quartz tile polish parameter in QSIM can be tuned to precisely match the data. QSIM's GLISUR model describes the quartz optical polish with a single parameter that needs to be benchmarked by matching real photoelectron distributions and simulated ones. For the 6 mm and 10 mm thick

quartz tiles used in the PREX-II/CREX detector during the beam test at Mainz and SLAC, the simulation matches the data with a polish parameter of 0.98. The quartz tiles used in the Shower-max benchmarking prototypes gave a slightly lower polish but nearly the same for PREX-II/CREX.

The optical (photon) simulation in Geant4 has many peculiarities that set it apart from the simulation of other types of particles (as discussed). The incorrect handling of these peculiarities can lead to unrealistic or inconsistent results. The number of parameters required by the optical simulation can be overwhelming if not for the invaluable testbeam data, gain measurements and previous optical studies and literature in materials and photocathode properties.

The transport and detection of light is the basis for the working principles of many detectors. The optimized collection of light is not trivial and can be very important for detectors used in high precision measurements in order to have a large signal to noise ratio and high resolution. The optical simulation, QSIM, will serve as a designing tool, within the ISU parity group, for future detectors that incorporate photosensitive devices and complex lightguide geometries with quartz Cerenkov radiators.

References

[1] B. Ananthanarayan et al. "Asymmetry in nature—Discrete symmetries in particle physics and their violation". In: *Resonance* 7.3 (Mar. 2002), pp. 10–17. ISSN: 0973-712X. DOI: 10.1007/BF02896303. URL: https://doi.org/10.1007/BF02896303.

[2] T. D. Lee and C. N. Yang. "Question of Parity Conservation in Weak Interactions". In: *Phys. Rev.* 104 (1 Mar. 1956), pp. 254–258. DOI: 10.1103/PhysRev.104.254. URL: https://link.aps.org/doi/10.1103/PhysRev.104.254.

[3] C. S. Wu et al. "Experimental Test of Parity Conservation in Beta Decay". In: *Phys. Rev.* 105 (4 Feb. 1957), pp. 1413–1415. DOI: 10.1103/PhysRev.105.1413. URL: https://link.aps.org/doi/10.1103/PhysRev.105.1413.

[4] Mark Thomson. *Modern particle physics*. New York: Cambridge University Press, 2013. ISBN: 9781107034266. URL: http://www-spires.fnal.gov/spires/find/books/www?cl=QC793.2.T46::2013.

[5] C. Y. Prescott et al. "Parity Nonconservation in Inelastic Electron Scattering". In: *Phys. Lett.* 77B (1978), pp. 347–352. DOI: 10.1016/0370-2693(78)90722-0.

[6] Charles Y. Prescott. "Weak-electromagnetic interference in polarized eD scattering". In: 1992.

[7] A. Franklin. *Selectivity and Discord: Two Problems of Experiment*. University of Pittsburgh Press, 2002. ISBN: 9780822941910. URL: https://books.google.com/books?id=l%5C_v0ioy5M5UC.

[8] K.D. Souder P. & Paschke. "Parity violation in electron scattering". In: *Front. Phys.* (2016).

[9] Jens Erler et al. "Weak Polarized Electron Scattering". In: *Annual Review of Nuclear and Particle Science* 64.1 (2014), pp. 269–298. DOI: 10.1146/annurev-nucl-102313-025520. eprint: https://doi.org/10.1146/annurev-nucl-102313-025520. URL: https://doi.org/10.1146/annurev-nucl-102313-025520.

[10] *PREX-II: PRECISION PARITY-VIOLATING MEASUREMENT OF THE NEUTRON SKIN OF LEAD*. https://hallaweb.jlab.org/parity/prex/prexII.pdf.

[11] Abrahamyan *et al.* "Measurement of the Neutron Radius of ^{208}Pb through Parity Violation in Electron Scattering". In: *Phys. Rev. Lett.* 108 (11 Mar. 2012), p. 112502. DOI: 10.1103/PhysRevLett.108.112502. URL: https://link.aps.org/doi/10.1103/PhysRevLett.108.112502.

[12] A.M. Fox. *Optical Properties of Solids*. Oxford master series in condensed matter physics. Oxford University Press, 2001. ISBN: 9780198506126. URL: https://books.google.com/books?id=-5bVBbAoaGoC.

[13] E.D. Palik and G. Ghosh. *Handbook of Optical Constants of Solids*. Academic Press handbook series v. 2. Elsevier Science, 1991. ISBN: 9780125444224. URL: https://books.google.com/books?id=d4%5C_kRYYS0H8C.

[14] I. H. Malitson. "Interspecimen Comparison of the Refractive Index of Fused Silica*,†". In: *J. Opt. Soc. Am.* 55.10 (Oct. 1965), pp. 1205–1209. DOI: 10.1364/JOSA.55.001205. URL: http://www.osapublishing.org/abstract.cfm?URI=josa-55-10-1205.

[15] Rei Kitamura, Laurent Pilon, and Miroslaw Jonasz. "Optical constants of silica glass from extreme ultraviolet to far infrared at near room temperature". In: *Appl. Opt.* 46.33 (Nov. 2007), pp. 8118–8133. DOI: 10.1364/AO.46.008118. URL: http://ao.osa.org/abstract.cfm?URI=ao-46-33-8118.

[16] Connor Harper. *Reproducibility of optically stimulated luminescence dosimeters in mixed radiation fields.* URL: http://libpublic3.library.isu.edu/login?url=http://search.ebscohost.com/login.aspx?direct=true&db=cat06825a&AN=isu.b2268200&site=eds-live&scope=site.

[17] *Ultraviolet*. https://en.wikipedia.org/wiki/Ultraviolet.

[18] Qingliang Zhao et al. "Deformation analysis of micro/nano indentation and diamond grinding on optical glasses". In: *Chinese Journal of Mechanical Engineering* 25.3 (May 2012), pp. 411–418. ISSN: 1000-9345. DOI: 10.3901/CJME.2012.03.411. URL: https://doi.org/10.3901/CJME.2012.03.411.

[19] *Photocathode*. http://farside.ph.utexas.edu/teaching/em/lectures/node100.html.

[20] Peter R. Hobson. "The photomultiplier handbook, by A. G. Wright". In: *Contemporary Physics* 59.1 (2018), pp. 101–102. DOI: 10.1080/00107514.2017.1403486. eprint: https://doi.org/10.1080/00107514.2017.1403486. URL: https://doi.org/10.1080/00107514.2017.1403486.

[21] H. Sonnenberg. "Negative-electron-affinity photoemitters". In: *IEEE Journal of Solid-State Circuits* 5.5 (Mar. 1970), pp. 272–275. ISSN: 0018-9200. DOI: 10.1109/JSSC.1970.1050126.

[22] Triveni Rao and David H. Dowell. *An Engineering Guide To Photoinjectors*. 2014. arXiv: 1403.7539 [physics.acc-ph].

[23] *Photocathode*. https://en.wikipedia.org/wiki/Photocathode.

[24] Daniella Motta and Stefan Schoenert. "Optical properties of bialkali photocathodes". In: *Nuclear Instruments and Methods in Physics Research Section A: Accelerators, Spectrometers, Detectors and Associated Equipment* 539 (Sept. 2004), pp. 217–235. DOI: 10.1016/j.nima.2004.10.009.

[25] M. E. Moorhead and Nancy Tanner. "Optical properties of an EM1 IQCsSb bialkali photocathode". In: *Nuclear Instruments and Methods in Physics Research A* (1996).

[26] M.D. lay. "Parameterisation of the angular response of the R1408 Hamamatsu eight-inch photomultiplier tube to be used in the Sudbury Neutrino Observatory". In: *Nuclear Instruments and Methods in Physics Research Section A: Accelerators, Spectrometers, Detectors and Associated Equipment* 383.2 (1996), pp. 485–494. ISSN: 0168-9002. DOI: https://doi.org/10.1016/S0168-9002(96)00860-1. URL: http://www.sciencedirect.com/science/article/pii/S0168900296008601.

[27] Hamamatsu Photonics K.K. *Hamamtsu PMT Handbook*. 3rd Edition. Chap. 4.

[28] Brady Lowe. "High-Precision PMT Gain Measurement With Subsequent Quartz Cerenkov Detector Characterization". MA thesis. Idaho State University, 2019.

[29] W. D. Gunter, G. R. Grant, and S. A. Shaw. "Optical Devices to Increase Photocathode Quantum Efficiency". In: *Appl. Opt.* 9.2 (Feb. 1970), pp. 251–257. DOI: 10.1364/AO.9.000251. URL: http://ao.osa.org/abstract.cfm?URI=ao-9-2-251.

[30] S Hallensleben, S W Harmer, and P D Townsend. "Limitations on the enhancement of photomultiplier quantum efficiency through multiple total internal reflection". In: *Journal of Physics D: Applied Physics* 32.5 (Jan. 1999), pp. 623–628. DOI: 10.1088/0022-3727/32/5/019. URL: https://doi.org/10.1088%2F0022-3727%2F32%2F5%2F019.

[31] *GEANT4 Physics Reference Manual*. http://geant4-userdoc.web.cern.ch/geant4-userdoc/UsersGuides/PhysicsReferenceManual/fo/PhysicsReferenceManual.pdf.

[32] Erik Dietz-Laursonn. "Detailed studies of light transport in optical components of particle detectors". Veröffentlicht auf dem Publikationsserver der RWTH

Aachen University; Dissertation, RWTH Aachen University, 2016. Dissertation. Aachen: RWTH Aachen University, 2016. URL: http://publications.rwth-aachen.de/record/667646.

[33] S. Agostinelli et al. "Geant4—a simulation toolkit". In: *Nuclear Instruments and Methods in Physics Research Section A: Accelerators, Spectrometers, Detectors and Associated Equipment* 506.3 (2003), pp. 250–303. ISSN: 0168-9002. DOI: https://doi.org/10.1016/S0168-9002(03)01368-8. URL: http://www.sciencedirect.com/science/article/pii/S0168900203013688.

[34] Erik Dietz-Laursonn. "Peculiarities in the Simulation of Optical Physics with Geant4". In: 2016.

[35] S Lo Meo et al. "A Geant4 simulation code for simulating optical photons in SPECT scintillation detectors". In: *Journal of Instrumentation* 4.07 (2009), P07002. URL: http://stacks.iop.org/1748-0221/4/i=07/a=P07002.

[36] Kevin Rhine. Private Communication. Pocatello, ID, USA,

[37] Kiadtisak Saenboonruang and Nima Liyanage. "Q2 measurement and challenges in PREX". In: *Kasetsart Journal - Natural Science* 49 (Aug. 2015), pp. 277–287.

[38] Jorge Piekarewicz and Farrukh J. Fattoyev. "Neutron-rich matter in heaven and on Earth". In: *Physics Today* 72.7 (2019), pp. 30–37. DOI: 10.1063/PT.3.4247. eprint: https://doi.org/10.1063/PT.3.4247. URL: https://doi.org/10.1063/PT.3.4247.

[39] B.M. Roberts, V.A. Dzuba, and V.V. Flambaum. "Parity and Time-Reversal Violation in Atomic Systems". In: *Annual Review of Nuclear and Particle Science* 65.1 (2015), pp. 63–86. DOI: 10.1146/annurev-nucl-102014-022331. eprint: https://doi.org/10.1146/annurev-nucl-102014-022331. URL: https://doi.org/10.1146/annurev-nucl-102014-022331.

Appendix

Detailed "how-to" description of QSIM

In consideration with future students and researchers a more detailed, how-to discussion of QSIM is appropriated. First of all, Geant4 provides several physics lists which are routinely validated and updated with each release of Geant4. The physics list used depends highly on the use-case, from low energy radio-biological applications to high energy physics experiments. QSIM uses Geant4's `FTFP-BERT` reference physics list with the standard electromagnetic processes. `FTFP` stands for Fritiof model, valid for energies $\geq$ to 10 GeV, which is an order of magnitude greater than the 0.95 GeV PREX-II/CREX experiment energy. `BERT` stands for Bertini Cascade Model for energies $<$ to 10 GeV. `BERT` includes the Standard EM Physics package that describes the electromagnetic processes in Geant4.

In order to run a QSIM simulation, we need a macro file. One can find macro files examples in the build directory `QSIM/build/macros`. There, the user define the run mode:

```
   Set run mode
/qsim/fDetMode 4
/qsim/fQMode 0
/qsim/fStandMode 0
/qsim/fSourceMode 1
```

`fDetMode` selects the detector mode. The detector mode options can be:

$$\texttt{G4int detMode} == \begin{cases} 0 & \text{PREX-I detector geometry} \\ 1 & \text{PREX-II prototype (single quartz) detector geometry} \\ 2 & \text{SAM detector} \\ 3 & \text{ShwerMax detector} \\ 4 & \text{PREX-II/CREX tandem detector} \end{cases}$$

Different detector modes use quartz pieces with different dimensions. `qMode` selects the quartz geometry:

$$\texttt{G4int qMode} == \begin{cases} 0 & \text{PREX-I/PREX-II quartz geometry} \\ 1 & \text{SAM's quartz geometry} \\ 2 & \text{Shower-max's quartz geometry} \end{cases}$$

After choosing a `detMode` and a `qMode`, we can set other parameters, like the quartz polish parameter and detector angle and position:

```
   Set detector properties
/qsim/fQuartzPolish 0.98
/qsim/fDetAngle 0 deg
/qsim/fDetPosX 0 cm
/qsim/fDetPosY 0 cm
```

Then, the user initialize the run, set the primary particle kind, energy range, the name of the output file and number of events:

```
   Initialize run
/run/initialize
/qsim/filename qsim-out.root
```

```
/qsim/seed 50
/qsim/emin 1.0 GeV
/qsim/emax 1.0 GeV
/gun/particle e-
/run/beamOn 1
```

As mentioned before, the geometry, the materials and their optical properties have to be specified in the `qsim-master/src/qsimDetectorConstruction.cc` source file. The geometry varies according to the detector mode selection, this is done by selecting the desired flags which points to an `If` statement where the detector geometry is defined.

With the purpose of illustration let's consider the particular case in which we simulate the PREX-II prototype (a single quartz piece with a PMT) detector geometry (see Figure 99).

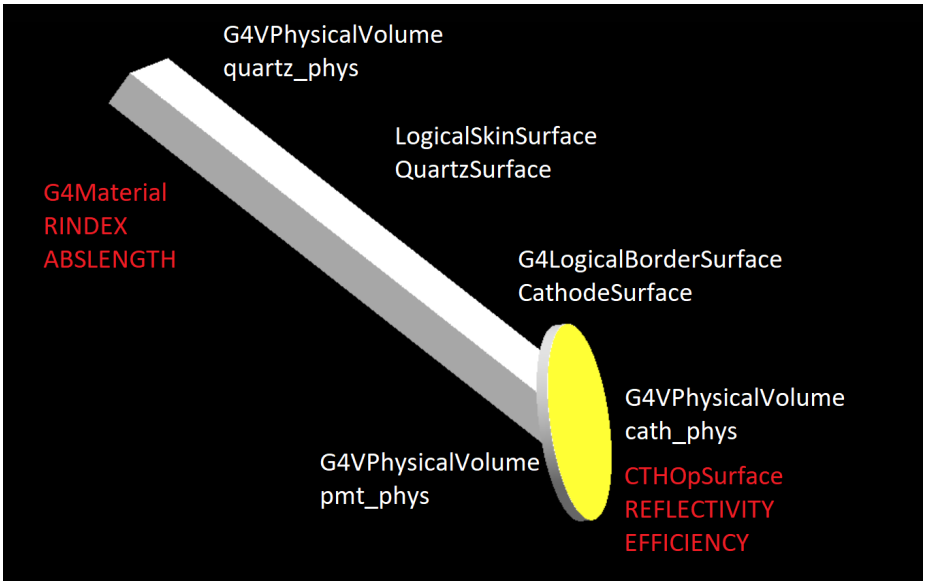

Figure 99: PREX-II, single quartz detector prototype. The G4 physical volumes, `G4VPhysicalVolume`, and the optical surfaces (`G4LogicalSkinSurface, ↪ G4LogicalBorderSurface`) implemented in the simulation are indicated in the figure. Notice that only the surfaces with relevant optical surfaces are included in the simulation.

Let us explain how we can define the geometry and to add the optical properties.

It starts with the quartz material definition, where Quartz is made of two elements, Silicon and Oxygen:

```
G4Element* Si = new G4Element("Silicon", "Si", z=14, a=28*g/mole);
G4Element* O = new G4Element("Oxygen" , "O", z=8 , a=16.00*g/mole)
    ↪ ;

G4Material* Quartz = new G4Material("Quartz", density= 2.203*g/cm3
    ↪ , nelements=2);
Quartz->AddElement(Si, 1);
Quartz->AddElement(O, 2);
```

Once the material is created, we should associate an optical material property table to it:

```
// Quartz material property table

G4MaterialPropertiesTable* myMPT1 = new G4MaterialPropertiesTable
    ↪ ();
myMPT1->AddProperty("RINDEX", PhotonEnergy, RefractiveIndex1,
    ↪ nEntries);
myMPT1->AddProperty("ABSLENGTH", PhotonEnergy, Absorption1,
    ↪ nEntries);
Quartz->SetMaterialPropertiesTable(myMPT1);
```

The material property table for `Quartz`, named here `myMPT1`, has two properties: `RINDEX`, index of refraction, and `ABSLENGTH`, the absorption length of quartz. These properties are given in the form of an array with a number of entries, `nEntries`. All the property arrays have to be the same length of the photon energies array. For example, each entry is the refractive index and the absorption length arrays at the

energy value in the corresponding position in the photon energy array. These energies should be inside the sensitive range of the PMT used.

```
//Array of photon energies for R7723Q
    G4double PhotonEnergy[nEntries] = {1.8233, 1.85051, 1.87855,
        ↪ 1.90745, 1.93725, 1.968, 1.99975, 2.03253, 2.0664, 2.10143,
        ↪  2.13766, 2.17516, 2.214, 2.25426, 2.296, 2.33932, 2.38431,
        ↪  2.43106, 2.47968, 2.53029, 2.583, 2.63796, 2.69531,
        ↪ 2.7552, 2.81782, 2.88335, 2.952, 3.024, 3.09961, 3.17908,
        ↪ 3.26274, 3.35092, 3.44401, 3.54241, 3.64659, 3.7571,
        ↪ 3.87451, 3.99949, 4.13281, 4.27532, 4.42801, 4.59201,
        ↪ 4.76862, 4.95937, 5.16601, 5.39062, 5.63565, 5.90401,
        ↪ 6.19921};
```

For the refractive index and absorption length of quartz, we use a parametrization, where we calculate an index of refraction for each photon energy in the array:

```
//Refractive index for quartz
RefractiveIndex1[i]= 1.438 + (.01197*PhotonEnergy[i]/eV) - (.001955*
    ↪ PhotonEnergy[i]*PhotonEnergy[i]/eV/eV) + (.0004793*PhotonEnergy
    ↪ [i]*PhotonEnergy[i]*PhotonEnergy[i]/eV/eV/eV);
```

```
   //Quartz absorption length
   Absorption1[i] = (exp(4.325)*exp(1.191*PhotonEnergy[i]/eV)*exp
       ↪ (-.213*PhotonEnergy[i]*PhotonEnergy[i]/eV/eV)*exp(-.04086*
       ↪ PhotonEnergy[i]*PhotonEnergy[i]*PhotonEnergy[i]/eV/eV/eV))*m
       ↪ ;
   if (Absorption1[i] > 25*m) {
       Absorption1[i] = 25*m;
       }
```

With the material, `Quartz`, defined, we can proceed and create the quartz piece:

```
G4double q_yLB = quartz_y - (quartz_z);
G4double q_yLB2 = quartz2_y - (quartz2_z);

G4Trap* quartz_box = new G4Trap("Quartz", 2*quartz_x, 2*quartz_z,
    ↪ 2*quartz_y, 2*q_yLB);

G4LogicalVolume* quartz_log
= new G4LogicalVolume(quartz_box,Quartz,"Quartz",0,0,0);
```

After creating the `quartz_log` logical volume, we should define a `G4OpticalSurface`, this surface describes the optical characteristics of the quartz surface. We have used a `G4LogicalSkinSurface` so all the faces of the quartz will have the same optical surface finish.

```
// Surfaces
// quartz
G4OpticalSurface* OpQuartzSurface = new G4OpticalSurface("
    ↪ QuartzSurface");
OpQuartzSurface->SetType(dielectric_dielectric);
OpQuartzSurface->SetFinish(ground);
OpQuartzSurface->SetModel(glisur);
OpQuartzSurface->SetPolish(fQuartzPolish);
G4LogicalSkinSurface* QuartzSurface =
new G4LogicalSkinSurface("QuartzSurface",quartz_log,
    ↪ OpQuartzSurface);
```

The quartz pieces in our detectors is a right trapezoid, its dimensions depends of the `qMode` selected. Now it is possible to place the quartz inside the virtual volume

associated to the detector logical volume det_log:

```
G4VPhysicalVolume* quartz_phys
= new G4PVPlacement(rotQ,G4ThreeVector(0,0,quartz_zPos),quartz_log
    ↪ ,"Quartz", det_log,false,0);
```

Now we should add the photocathode. It consist on the PMT's quartz window (pmt_phys) and the bialkali coating (cath_phys):

```
G4VPhysicalVolume* pmt_phys = new G4PVPlacement(rot_pmt,
    ↪ G4ThreeVector(7.5*cm+3.6*mm,0.*cm,0.0*mm),pmt_log,"PMT",
    ↪ det_log,false,0);
G4VPhysicalVolume* cath_phys = new G4PVPlacement(rot_pmt,
    ↪ G4ThreeVector(7.5*cm+(plngth+clngth)*cos(M_PI/4*rad)+3.6*mm
    ↪ ,0.*cm,-(plngth+clngth)*sin(M_PI/4.*rad)-0.0*mm),cath_log,"
    ↪ CATH",det_log,false,0);
```

The quartz window shares the same optical properties as the quartz piece:

```
// quartz window
G4OpticalSurface* QWOpSurface = new G4OpticalSurface("
    ↪ QuartzWindowOpSurface");


QWOpSurface -> SetType(dielectric_dielectric);
QWOpSurface -> SetFinish(ground);
QWOpSurface -> SetModel(glisur);
QWOpSurface -> SetPolish(0.98);


G4LogicalVolume* pmt_log
= new G4LogicalVolume(pmt,Quartz,"PMT",0,0,0);
```

```
G4LogicalSkinSurface* QuartzWindowSurface = new
G4LogicalSkinSurface("QuartzWindowOpS",pmt_log,QWOpSurface);
```

Notice that we use previously defined material, `Quartz`, and we create an identical optical surface, `QWSurface`, for the window.

The boundary between the PMT quartz window and the cathode, `CathodeSurface` ↪ , have to include adequate cathode optical properties as well:

```
G4OpticalSurface* CTHOpSurface = new G4OpticalSurface("
    ↪ CathodeOpSurface");
CTHOpSurface -> SetType(dielectric_metal);
CTHOpSurface -> SetFinish(polished);
CTHOpSurface -> SetModel(glisur);
G4MaterialPropertiesTable* COpSurfaceProperty = new
    ↪ G4MaterialPropertiesTable();
COpSurfaceProperty -> AddProperty("REFLECTIVITY",PhotonEnergy,
    ↪ Reflectivity2,nEntries);
COpSurfaceProperty -> AddProperty("EFFICIENCY",PhotonEnergy,
    ↪ EfficiencyArray,nEntries);
CTHOpSurface -> SetMaterialPropertiesTable(COpSurfaceProperty);
G4LogicalBorderSurface* CathodeSurface =
new G4LogicalBorderSurface("CathodeSurface",pmt_phys,cath_phys,
    ↪ CTHOpSurface);
```

Notice that the cathode optical surface, `CTHOpSurface`, has a material property table, `COpSurfaceProperty`, attached to it. This material table has two optical properties: the cathode reflectivity, `REFLECTIVITY` and the PMT's quantum efficiency, `EFFICIENCY`.

The cathode reflectivity is set constant for every photon energy:

```
Reflectivity2[i] = 0.125;
```

The quantum efficiency is provided by the manufacturer:

```
//R7723Q quantum efficiency
//G4double EfficiencyArrayPercent[nEntries] = {0, 0.1, 0.2, 0.3,
    ↪ 0.6, 0.9, 1.4, 2, 2.7, 3.4, 4.2, 5, 5.8, 6.7, 7.7, 9.3, 12,
    ↪ 14.6, 15.9, 16.5, 17.4, 18.3, 19.7, 20.9, 21.8, 22.5, 23.1,
    ↪ 23.6, 24, 24.2, 24.4, 24.2, 24.1, 24.3, 24.4, 24.3, 24.1,
    ↪ 23.7, 22.9, 21.7, 20.1, 18.3, 17.2, 16.7, 15.8, 15, 15.1,
    ↪ 15.4, 16.2};
```

So far we have described how to define the volumes, which constitute the detector and how to add the relevant optical properties. Only one important part is missing: make of the photocathode a detector. This is done by making the cathode logical volume, `cath_log`, a `qsimDetector`, named here `cathSD`:

```
G4LogicalVolume* cath_log
= new G4LogicalVolume(cath,CATH,"CATH",0,0,0);
qsimDetector* cathSD = new qsimDetector("cath", 2);
SDman->AddNewDetector(cathSD);
cath_log->SetSensitiveDetector(cathSD);
```

In this way, `cath_log` is set as a sensitive detector with the name `cathSD` of the class `qsimDetector`. In order to make a "hit" (i.e. release a photoelectron), the photon has to be absorbed with a probability given by the `EFFICIENCY` array. `qsimDetector` is a custom class of QSIM. The logical volume set as a `qsimDetector` will tally the photons that go through it and save the information in a `root` file. In this example, the root file (`qsim_out.root`) contains 5462 events inside. Inside the root file save the entire information of this 5462 simulated events in the branches listed bellow:

```
*******************************************************************************
```

```
*Tree :T : Geant4 Quartz Detector Simulation *
*Entries : 5462 : Total = 68819709 bytes File Size = 48276542 *
* : : Tree compression factor = 1.41 *
******************************************************************************
*Br 0 :ev.pid : ev.pid/I *
*Entries : 5462 : Total Size= 36174 bytes File Size = 321 *
*Baskets : 2 : Basket Size= 40960 bytes Compression= 68.50 *
*.............................................................................*
*Br 1 :ev.vx : ev.vx/D *
*Entries : 5462 : Total Size= 71574 bytes File Size = 394 *
*Baskets : 2 : Basket Size= 54272 bytes Compression= 111.25 *
*.............................................................................*
*Br 2 :ev.vy : ev.vy/D *
*Entries : 5462 : Total Size= 71574 bytes File Size = 394 *
*Baskets : 2 : Basket Size= 54272 bytes Compression= 111.25 *
*.............................................................................*
*Br 3 :ev.vz : ev.vz/D *
*Entries : 5462 : Total Size= 71574 bytes File Size = 461 *
*Baskets : 2 : Basket Size= 54272 bytes Compression= 95.08 *
*.............................................................................*
*Br 4 :ev.p : ev.p/D *
*Entries : 5462 : Total Size= 71566 bytes File Size = 460 *
*Baskets : 2 : Basket Size= 54272 bytes Compression= 95.29 *
*.............................................................................*
*Br 5 :ev.px : ev.px/D *
*Entries : 5462 : Total Size= 71574 bytes File Size = 3243 *
*Baskets : 2 : Basket Size= 54272 bytes Compression= 13.52 *
*.............................................................................*
*Br 6 :ev.py : ev.py/D *
*Entries : 5462 : Total Size= 71574 bytes File Size = 3217 *
*Baskets : 2 : Basket Size= 54272 bytes Compression= 13.63 *
*.............................................................................*
*Br 7 :ev.pz : ev.pz/D *
```

```
*Entries : 5462 : Total Size= 71574 bytes File Size = 462 *
*Baskets : 2 : Basket Size= 54272 bytes Compression= 94.88 *
*.....................................................................*
*Br 8 :hit.n : hit.n/I *
*Entries : 5462 : Total Size= 36166 bytes File Size = 8235 *
*Baskets : 2 : Basket Size= 40960 bytes Compression= 2.67 *
*.....................................................................*
*Br 9 :hit.det : hit.det[hit.n]/I *
*Entries : 5462 : Total Size= 1912125 bytes File Size = 28813 *
*Baskets : 39 : Basket Size= 1168896 bytes Compression= 65.21 *
*.....................................................................*
*Br 10 :hit.vid : hit.vid[hit.n]/I *
*Entries : 5462 : Total Size= 1912125 bytes File Size = 27729 *
*Baskets : 39 : Basket Size= 1168896 bytes Compression= 67.76 *
*.....................................................................*
*Br 11 :hit.pid : hit.pid[hit.n]/I *
*Entries : 5462 : Total Size= 1912125 bytes File Size = 27765 *
*Baskets : 39 : Basket Size= 1168896 bytes Compression= 67.67 *
*.....................................................................*
*Br 12 :hit.trid : hit.trid[hit.n]/I *
*Entries : 5462 : Total Size= 1912170 bytes File Size = 880302 *
*Baskets : 39 : Basket Size= 1169408 bytes Compression= 2.13 *
*.....................................................................*
*Br 13 :hit.mtrid : hit.mtrid[hit.n]/I *
*Entries : 5462 : Total Size= 1912215 bytes File Size = 68150 *
*Baskets : 39 : Basket Size= 1169408 bytes Compression= 27.57 *
*.....................................................................*
*Br 14 :hit.gen : hit.gen[hit.n]/I *
*Entries : 5462 : Total Size= 1912125 bytes File Size = 28970 *
*Baskets : 39 : Basket Size= 1168896 bytes Compression= 64.86 *
*.....................................................................*
*Br 15 :hit.x : hit.x[hit.n]/D *
*Entries : 5462 : Total Size= 3769214 bytes File Size = 3374982 *
```

```
*Baskets : 75 : Basket Size= 2322944 bytes Compression= 1.11 *
*.....*
*Br 16 :hit.y : hit.y[hit.n]/D *
*Entries : 5462 : Total Size= 3769214 bytes File Size = 3584879 *
*Baskets : 75 : Basket Size= 2322944 bytes Compression= 1.04 *
*.....*
*Br 17 :hit.z : hit.z[hit.n]/D *
*Entries : 5462 : Total Size= 3769214 bytes File Size = 3316612 *
*Baskets : 75 : Basket Size= 2322944 bytes Compression= 1.13 *
*.....*
*Br 18 :hit.px : hit.px[hit.n]/D *
*Entries : 5462 : Total Size= 3769295 bytes File Size = 3555429 *
*Baskets : 75 : Basket Size= 2322944 bytes Compression= 1.05 *
*.....*
*Br 19 :hit.py : hit.py[hit.n]/D *
*Entries : 5462 : Total Size= 3769295 bytes File Size = 3580711 *
*Baskets : 75 : Basket Size= 2322944 bytes Compression= 1.04 *
*.....*
*Br 20 :hit.pz : hit.pz[hit.n]/D *
*Entries : 5462 : Total Size= 3769295 bytes File Size = 3554639 *
*Baskets : 75 : Basket Size= 2322944 bytes Compression= 1.05 *
*.....*
*Br 21 :hit.vx : hit.vx[hit.n]/D *
*Entries : 5462 : Total Size= 3769295 bytes File Size = 3140393 *
*Baskets : 75 : Basket Size= 2322944 bytes Compression= 1.19 *
*.....*
*Br 22 :hit.vy : hit.vy[hit.n]/D *
*Entries : 5462 : Total Size= 3769295 bytes File Size = 3143920 *
*Baskets : 75 : Basket Size= 2322944 bytes Compression= 1.19 *
*.....*
*Br 23 :hit.vz : hit.vz[hit.n]/D *
*Entries : 5462 : Total Size= 3769295 bytes File Size = 2899340 *
*Baskets : 75 : Basket Size= 2322944 bytes Compression= 1.29 *
```

```
*.....................................................................*
*Br 24 :hit.vdx : hit.vdx[hit.n]/D *
*Entries : 5462 : Total Size= 3769376 bytes File Size = 3428405 *
*Baskets : 75 : Basket Size= 2323456 bytes Compression= 1.09 *
*.....................................................................*
*Br 25 :hit.vdy : hit.vdy[hit.n]/D *
*Entries : 5462 : Total Size= 3769376 bytes File Size = 3467432 *
*Baskets : 75 : Basket Size= 2323456 bytes Compression= 1.08 *
*.....................................................................*
*Br 26 :hit.vdz : hit.vdz[hit.n]/D *
*Entries : 5462 : Total Size= 3769376 bytes File Size = 3205787 *
*Baskets : 75 : Basket Size= 2323456 bytes Compression= 1.17 *
*.....................................................................*
*Br 27 :hit.p : hit.p[hit.n]/D *
*Entries : 5462 : Total Size= 3769214 bytes File Size = 3424376 *
*Baskets : 75 : Basket Size= 2322944 bytes Compression= 1.09 *
*.....................................................................*
*Br 28 :hit.e : hit.e[hit.n]/D *
*Entries : 5462 : Total Size= 3769214 bytes File Size = 3410984 *
*Baskets : 75 : Basket Size= 2322944 bytes Compression= 1.10 *
*.....................................................................*
*Br 29 :hit.m : hit.m[hit.n]/D *
*Entries : 5462 : Total Size= 3769214 bytes File Size = 40481 *
*Baskets : 75 : Basket Size= 2322944 bytes Compression= 92.28 *
*.....................................................................*
*Br 30 :sci.n : sci.n/I *
*Entries : 5462 : Total Size= 36166 bytes File Size = 2305 *
*Baskets : 2 : Basket Size= 40960 bytes Compression= 9.54 *
*.....................................................................*
*Br 31 :sci.det : sci.det[sci.n]/I *
*Entries : 5462 : Total Size= 60089 bytes File Size = 6734 *
*Baskets : 3 : Basket Size= 47616 bytes Compression= 5.78 *
*.....................................................................*
```

```
*Br 32 :sci.id : sci.id[sci.n]/I *
*Entries : 5462 : Total Size= 60080 bytes File Size = 6717 *
*Baskets : 3 : Basket Size= 47616 bytes Compression= 5.80 *
*.....................................................................*
*Br 33 :sci.edep : sci.id[sci.n]/D *
*Entries : 5462 : Total Size= 79463 bytes File Size = 40358 *
*Baskets : 3 : Basket Size= 52736 bytes Compression= 1.38 *
*.....................................................................*
```

As mentioned, the output tree is organized into several branches. Here is a brief description of each one:

```
ev.* - generated particle info, one entry per particle
hit.* - detector hits
sci.* - scintillator detector sums


event data - single variables
ev.pid  Geant4 particle type
ev.v[xyz] creation vertex, lab frame [m]
ev.p  Particle initial momentum [GeV]
ev.p[xyz] Particle initial momentum components, lab frame [GeV]
ev.th  Particle initial polar angle [rad]
ev.ph  Particle initial azimuthal angle [rad]


hit data
hit.n  Number of hits for the event, the number, being modulated by the PMT's
    ↪ EFFICIENCY, is the number of electrons emitted from cathode for event n
hit.det  Detector number (2 is the PMT)
hit.vid  Volume ID number (not yet implemented)
hit.pid  Geant4 particle type
hit.trid Geant4 track ID number (1 = first particle created)
hit.mtrid Geant4 mother track ID number (0 = particle from gun)
hit.gen  Generator (not yet implemented)
```

```
hit.[xyz] Hit coordinate, lab frame [m]
hit.p  Momentum magnitude of particle [GeV]
hit.p[xyz] Momentum components of particle, lab frame [GeV]
hit.v[xyz] Creation vertex of particles
hit.e  Energy of particle [GeV]
hit.m  Mass of particle [GeV]

scint data
sci.n  Number of hits for the event
sci.det  Detector number (1 top only, 2 bottom only, 10 for both)
sci.vid  Volume ID number (not yet implemented)
sci.edep Energy deposited [GeV]
```

For further illustration, let us print the arrays corresponding to one of the event (`EVENT 17`). In this event, a 8 GeV electron (ev.pid = 11, ev.p = 8) hits the quartz creating Cerenkov photons (hit.pid = 0). 138 (hit.n = 138) of these photons arrived to the cathode to be absorbed, effectively releasing an equal number, 138, of photoelectrons (the actual release of photoelectrons is not simulated, but the number of photon hits distribution on the photocathode modulated by the QE is effectively the photoelectron distribution). I have printed only 20 entries from the total number (138) in order to save pages. In this detector configuration, no scintillators are used, so the sci.* arrays are all empty.

```
   ======> EVENT:17
 ev.pid = 11
 ev.vx = 0
 ev.vy = 0
 ev.vz = -4
 ev.p = 8
 ev.px = 0
 ev.py = 0
 ev.pz = 8
 hit.n = 138
 hit.det = 2,
```

```
                2, 2, 2, 2, 2, 2, 2, 2, 2, 2,
                2, 2, 2, 2, 2, 2, 2, 2, 2
hit.vid = 0,
                0, 0, 0, 0, 0, 0, 0, 0, 0, 0,
                0, 0, 0, 0, 0, 0, 0, 0, 0
hit.pid = 0,
                0, 0, 0, 0, 0, 0, 0, 0, 0, 0,
                0, 0, 0, 0, 0, 0, 0, 0, 0
hit.trid = 622,
                616, 612, 604, 604, 597, 587, 585, 565, 549, 546,
                543, 524, 472, 470, 453, 441, 427, 425, 415
hit.mtrid = 2,
                2, 2, 2, 2, 2, 2, 2, 2, 2, 2,
                2, 2, 2, 2, 2, 2, 2, 2, 2
hit.gen = 636255984,
                636255984, 636255984, 636255984, 636255984, 636255984, 636255984,
                    ↪ 636255984, 636255984, 636255984, 636255984,
                636255984, 636255984, 636255984, 636255984, 636255984, 636255984,
                    ↪ 636255984, 636255984, 636255984
hit.x = 0.07814,
                0.0740276, 0.0747395, 0.0771727, 0.0740486, 0.0739824,
                0.0755796, 0.0729008, 0.076288, 0.0778163, 0.0773328,
                0.0735681, 0.079648, 0.0735079, 0.0762218, 0.0777803,
                0.0795907, 0.0769669, 0.0709444, 0.0722476
hit.y = 0.0144082,
                0.0109109, -0.0134964, -0.00590374, -0.01582, 0.0198674,
                -0.0164041, -0.00439331, -0.0143648, -0.00135864, 0.0103319,
                -0.0045145, 0.0059838, 0.00856907, 0.00421428, 0.00735944,
                0.0144255, 0.00813306, -0.0161378, -0.0161232
hit.z = -0.162181,
                -0.162051, -0.165582, -0.163149, -0.16203, -0.166339,
                -0.160499, -0.163178, -0.159791, -0.162505, -0.158746,
                -0.162511, -0.160673, -0.162571, -0.159857, -0.158298,
```

```
                -0.160731, -0.159112, -0.165134, -0.163831
hit.px = -3.2182e-09,
                2.89396e-09, -2.70929e-09, -2.41078e-09, 2.56172e-09, -2.53432e
                    ↪ -09,
                2.45233e-09, 3.80927e-09, 2.13878e-09, -1.29883e-09, 2.68753e-09,
                2.4697e-09, -2.4681e-09, 2.11377e-09, 1.94705e-09, 2.32616e-09,
                -3.35256e-09, 3.0131e-09, 1.21736e-09, 1.03026e-09
hit.py = 5.51139e-10,
                -1.48935e-09, -3.58324e-10, -1.19938e-09, -1.27904e-09, 1.40868e
                    ↪ -09,
                -1.44705e-09, 1.64146e-09, 5.64968e-10, -1.30946e-09, 1.64846e-09,
                2.09382e-09, 1.06104e-09, -7.37074e-10, -3.94808e-10, 1.31682e-09,
                -6.616e-10, -1.02811e-09, -1.83511e-09, -1.58699e-09
hit.pz = 3.11468e-09,
                -2.09426e-09, 2.83618e-09, 2.0178e-09, -1.76735e-09, 2.23105e-09,
                -2.69857e-09, -2.76083e-09, -1.65133e-09, 1.62304e-09, -3.22212e
                    ↪ -09,
                -2.49717e-09, 2.6491e-09, -2.31465e-09, -2.05256e-09, -2.48596e
                    ↪ -09,
                3.38787e-09, -2.52708e-09, -2.24807e-09, -1.85922e-09
hit.vx = -0.000963828,
                -0.000962786, -0.000964189, -0.000963953, -0.000963953,
                    ↪ -0.000964049,
                -0.000963531, -0.000963407, -0.000962975, -0.00096268,
                    ↪ -0.000962951,
                -0.000964446, -0.000964152, -0.000964177, -0.000962507,
                    ↪ -0.000963751,
                -0.000963551, -0.000962753, -0.000963154, -0.000963207
hit.vy = -0.000955044,
                -0.000954342, -0.000955286, -0.000955128, -0.000955128,
                    ↪ -0.000955192,
                -0.000954844, -0.00095476, -0.000954469, -0.000954271,
                    ↪ -0.000954453,
```

```
                -0.000955459, -0.000955262, -0.000955279, -0.000954154,
                    ↪ -0.000954992,
                -0.000954857, -0.00095432, -0.00095459, -0.000954625
hit.vz = -0.158508,
                -0.16144, -0.157495, -0.158157, -0.158157, -0.157888,
                -0.159345, -0.159693, -0.160909, -0.16174, -0.160978,
                -0.156772, -0.157597, -0.157527, -0.162227, -0.158725,
                -0.159288, -0.161535, -0.160405, -0.160258
hit.vdx = 0.735688,
                -0.681265, 0.722663, 0.64961, 0.64961, 0.604341,
                -0.650659, -0.684412, 0.703333, 0.482828, 0.638947,
                -0.487262, 0.650542, 0.682202, -0.684136, 0.654085,
                0.716388, 0.698672, 0.383217, 0.361611
hit.vdy = 0.108256,
                0.285162, -0.153141, 0.34289, 0.34289, -0.421336,
                0.350219, -0.304143, -0.199733, -0.547203, -0.380582,
                0.557139, -0.347453, 0.269901, -0.260715, -0.338803,
                0.210147, 0.24275, 0.625117, 0.634732
hit.vdz = 0.668614,
                0.674212, 0.674022, 0.678553, 0.678553, 0.676201,
                0.673787, 0.662629, 0.682224, 0.6837, 0.668509,
                0.672437, 0.675331, 0.679525, 0.681165, 0.676303,
                0.665301, 0.673001, 0.67998, 0.682901
hit.p = 4.51241e-09,
                3.87028e-09, 3.9386e-09, 3.3648e-09, 3.3648e-09, 3.65852e-09,
                3.92303e-09, 4.98268e-09, 2.76051e-09, 2.45681e-09, 4.50803e-09,
                4.08893e-09, 3.77294e-09, 3.22008e-09, 2.85655e-09, 3.65035e-09,
                4.81197e-09, 4.06471e-09, 3.14697e-09, 2.65268e-09
hit.e = 4.51241e-09,
                3.87028e-09, 3.9386e-09, 3.3648e-09, 3.3648e-09, 3.65852e-09,
                3.92303e-09, 4.98268e-09, 2.76051e-09, 2.45681e-09, 4.50803e-09,
                4.08893e-09, 3.77294e-09, 3.22008e-09, 2.85655e-09, 3.65035e-09,
                4.81197e-09, 4.06471e-09, 3.14697e-09, 2.65268e-09
```

```
hit.m = 0,
                0, 0, 0, 0, 0,
                0, 0, 0, 0, 0,
                0, 0, 0, 0, 0,
                0, 0, 0, 0
sci.n = 1
sci.det = 15
sci.id = 0
sci.id = 0.000632741
```